UNIVERSITÀ
DEGLI STUDI
FIRENZE

Scuola di
Scienze Matematiche
Fisiche e Naturali

Corso di Laurea Magistrale in
Scienze Fisiche ed Astrofisiche

Shapiro Steps in a fermionic superfluid Josephson junction

Shapiro Steps in una giunzione Josepshon superfluida fermionica

Candidato: Giulio Nesti
Relatrice: Dr. Giulia Del Pace

Anno Accademico: 2023/2024

To Domenico and Graziano, no longer between us

Contents

Introduction

In the context of new emerging quantum technologies, Josephson junctions represent a powerful experimental tool which allows to investigate macroscopic quantum phenomena associated with condensed states [1], occurring together with spontaneous symmetry breaking [2]. These devices are made up by two superconducting metals, weakly coupled by a thin insulating barrier that allows for quantum tunneling [3]. In solid state physics, superconducting Josephson junctions are widely investigated by injecting an external current; the unique transport properties of the device due to tunneling of Cooper pairs are deeply connected with the system's macroscopic wave function Ψ, which behaves as the order parameter of the superconductive phase transition [4]. Dissipationless (i.e. non-resistive) currents are observed to flow inside these systems, being merely sustained by the relative phase difference $\phi = \phi_1 - \phi_2$ between the order parameters associated with the two superconductors [5]. Another noteworthy platform employed for the creation of modern quantum technologies is represented by quantum gases, which can be experimentally realized through laser cooling and trapping processes. They enable quantum simulations of complex many-body systems [6] as well as the realization of ultra-precise atomic sensors [7]. Quantum gases are characterized by key properties that make them particularly appealing for exploring quantum physics: controllable interactions, strong decoupling from the environment, long lifetimes and a large variety of experimental probes. Regarding the first property, the application of external magnetic fields B has been extensively employed in order to exploit Feshbach resonances, where interparticle interactions can be tuned as desired by changing the value of the s-wave scattering length a, a parameter which characterizes the interaction's strength both in bosonic and fermionic systems [8, 9]. Nonetheless, ultracold Fermi gases present a unique phenomenology, not observed in Bose gases. In fact, these systems run through three different interaction regimes while sweeping the value of external magnetic fields [10]: the weakly-repulsive regime where atoms bound together in bosonic molecules (BEC gas), the weakly-attracting regime made-up of Cooper pairs (BCS gas) and the strongly-interacting fermionic regime (UFG), where interactions are the strongest allowed by nature and the system presents universal properties, regardless of the particle's nature. This phenomenon is known as the BEC-BCS crossover, and has been widely investigated both in theory and experiments [11, 12, 13, 14, 15]. Moreover, the presence of modern technologies such as spatial light modulator devices (SLMD) allows to entrap quantum gases within controllable geometries, where the parameters and shape of the trapping potential can be tuned as desired [16, 17]. In particular, it is possible to realize an analogue of the superconducting Josephson junction for a system of ultracold atoms: the so-called atomic Josephson junction, where the superfluid is separated into two distinct reservoirs by an optical barrier, thin enough so that particles can tunnel through it [18]. Many physical phenomena typical of the superconducting Josephson junction have been reproduced in the superfluid variant: the Josephson DC effect, where the application of a direct current generates a non-resistive current which flows inside the junction until the critical current I_c is overcome [19, 20], or the AC Josephson effect, where particles coherently oscillate in time from one side to the other of the device together with the relative phase ϕ [12, 21, 22, 23, 24]. The correspondence between superconducting and superfluid Josephson junctions is not exactly perfect: in fact, the atomic version also presents unique phenomena, not observed in the solid-state version. One noteworthy example is represented by the *macroscopic quantum self-trapping* (MQST), manifestation of the bosonic nature of the condensate, where Josephson oscillations centered around a non-zero value of the particle imbalance ΔZ are measured [25, 26]. On the other hand, in superconducting devices the application of an alternating current or radio-frequency allows to observe a peculiar structure in the ΔV-I characteristic of the junction: due to a synchronization between the applied frequency and the AC Josephson current, this curve presents regions having constant voltage drop ΔV for increasing current (plateaus), connected by almost discontinuous voltage jumps [27]. The step-like structure which forms is known in physics literature as **Shapiro steps**: these jumps are predicted to occur at voltages proportional to the injected current's frequency ν, through an integer n, according to $\Delta V_S = n\nu h/2e$ [28]. Shapiro steps provide an exact conversion from frequency to voltage: because the frequency can be measured with very high precision, this effect is used as the basis of the Josephson voltage standard [29, 30]. Their occurrence has been recently predicted for periodically driven superfluid Josephson junctions when displacing a thin optical barrier through a modulated trajectory, in order to induce an AC driving [31]. The goal of this thesis is the study of Shapiro steps in atomic Josephson junctions, where the superfluid reservoirs are constituted by ultracold ^{6}Li fermionic atoms in the weakly-repulsive regime of the BEC-BCS crossover. In such an experimental system the application of an external alternating current $I(t)$, which permits to probe these structures, represents a difficult task: the employment of a digital micro-mirror device (DMD) allows for the realization of such atomic currents, together with the optical potential and the thin insulating barrier constituting our superfluid junction. This thesis work is organised as follows:

1. In Chap. 1 we will provide an introduction to the physics of ultracold Fermi gases, focusing on their statistical properties. We start by dealing with the ideal Fermi gas, together with the case of confinement due to an external trapping potential $V_T(\vec{r})$; interparticle interactions are subsequently introduced, in order to discuss the BEC-BCS crossover resonance. We will also make a brief analysis of the phenomenon of superfluidity, introducing *Landau's criterion* and the concept of *quantized vortices*. This chapter is concluded with a discussion on the *Josephson effect*, both in the superconducting and superfluid case, in order to present the various analogies between them. In particular, we introduce the main circuital models employed for the study of real Josephson junc-

tions (RSJ and RCSJ), where the relative phase dynamics is described by the *tilted washboard potential* analogy: the presence of Shapiro steps in the $\Delta\mu - I$ characteristic of the device can be easily understood in this context.

2. The purpose of Chap. 2 is to introduce the experimental setup, together with the preliminary calibration procedure necessary for characterizing the thin Josephson barrier's properties. Initially, we will review the exact procedure followed in order to operatively realize the ultracold ^{6}Li Fermi gas, together with the corresponding experimental apparatus employed: the *absorption imaging* system is also presented in this part. We also discuss the working principle of the *digital-micro mirror device* (DMD), which allows to realize the atomic Josephson junction within the desired trapping geometry. In particular, in this thesis work we have opted for a hybrid confinement, where a rigid rectangular box traps the atomic cloud along the x-y plane, while along the vertical direction z an harmonic confinement is employed. We calculate the remarkable physical quantities (Fermi energy E_F, chemical potential μ, speed of sound c_s) describing a Fermi gas trapped within this geometry. Finally, we conclude the chapter by presenting the calibration procedure for the optical barrier's height: an estimate of its value V_0 allows to determine whether or not the junction is in the Josephson regime ($V_0/\mu > 1$), where transport phenomena occur due to tunneling events.

3. In Chap. 3 we report the measurements characterizing our elongated Josephson junction, consisting in a $125 \times 17.5\,\mu\text{m}^2$ box in the x-y plane realized through a repulsive optical dipole trap. We start with an analysis of the propagation of the sound modes inside the device, operatively excited by compressing one side of the junction: these perturbations are predicted to move within the junction at the speed of sound c_s. We will also present how the DMD allows to generate a direct atomic current within our junction, by displacing the optical barrier at a constant speed v_0. Afterwards, we discuss the coherent oscillations in time between the relative phase ϕ and the number of particles between the two superfluid reservoirs: their observation confirms that we are undoubtedly working with a device where the Josephson effect occurs. Finally, we will present and comment the measurements of the Josephson DC and AC effects, carried out by varying the horizontal length of the system and the intensity of the trapping laser. In this analysis we also extract the behaviour of some remarkable quantities, namely the critical current I_c and the Josephson oscillation frequency ν_j, as a function of the former parameters.

4. Finally, Chap. 4 is dedicated to reporting the measurements related to the Shapiro steps, carried out inside our atomic Josephson junction. A preliminary section presents how it is possible to generate a tunable alternating current $I(t)$ inside our microscopic device: in fact, this perturbation is necessary in order to observe the Shapiro steps phenomena. We will also study the behaviour of the chemical potential difference $\Delta\mu$ during the displacement of the thin optical barrier in time, carried out

via a rectilinear trajectory modulated by a periodic function. The measurements of the Shapiro steps are then reported, where the behaviour of the steps is analyzed as a function of the driving frequency ν: we expect, by analogy with the superconducting case, that this phenomenon occurs when the chemical potential jumps by $\Delta\mu_S = nh\nu$. We will also measure the number of quantum vortices observed at the end of the barrier's movement, as a function of its velocity v_0, in order to relate vortex nucleation with the emergence of Shapiro steps inside our superfluid junction. Finally, this thesis is concluded with the brief presentation of a measurement performed in the strongly-interacting *Unitary* regime, to demonstrate that the phenomenology of the Shapiro steps does not depend on the particular interaction regime considered: in particular, we show again that the step's height depends only on the modulation frequency ν.

Chapter 1

Ultracold Fermi gases and Josephson effect

This chapter is devoted to the introduction of basic concepts regarding the statistical properties of low-temperature Fermi gases and their collisional behaviour, together with a treatment of superfluidity in fermionic systems and Josephson effect in ultracold gases. These theoretical tools will provide a useful asset in order to understand the dynamics of the physical system considered in this thesis, consisting of a ^{6}Li ultracold gas trapped within a repulsive optical potential. In Secs. 1.1 and 1.2 we will recall the key features of a non-interacting (collisionless) Fermi gas, respectively in the free-particle case and for a spatially confined gas, the latter obtained via the application of an external trapping potential $V_T(\vec{r})$ onto the atomic cloud. A description of the interacting Fermi gas at low temperature will be given in Sec. 1.3, together with the introduction of *magnetic Feshbach resonances*, an invaluable tool which permits us to manipulate the interparticle interactions in the cloud. In ultracold Fermi gases, the interaction tunability allows us to explore the so-called BEC-BCS crossover, in which single atoms couple together to form a pair, its physical properties depending on the nature of the collisions. This is discussed in Sec. 1.4. An introduction of superfluidity phenomena will be provided in Sec. 1.5, where *Landau's criterion* for superfluidity and the emergence of quantized vortices in rotating superfluids will be analyzed. Finally, Sec. 1.6 will be devoted in presenting the Josephson effect, both in superconductors and atomic condensates, together with its main circuital models (RSJ and RCSJ): we conclude this chapter by discussing the emergence of **Shapiro steps** in the $\Delta V - I$ characteristic, which occurs when an alternating current $I(t)$, modulated at a certain frequency ν, is injected within a Josephson junction.

1.1 The ideal Fermi gas

The best context in which to discuss the quantum statistical properties of the *non-interacting* Fermi gas is the grand canonical ensemble, where calculations turn out to be straightforward. We recall that the probability to realise a configuration with N particles in a state of momentum $\hbar k$, with associated energy E_k, is [32]:

$$P_N(E_k) = e^{-\beta(E_k - \mu N)} \tag{1.1}$$

where β is $1/k_BT$, μ is the chemical potential of the reservoir with which the system is in thermal equilibrium, and T is its temperature. For a free particle, the relation between the energy and the wave vector k is simply given by:

$$E_k = \frac{\hbar^2 k^2}{2m} \tag{1.2}$$

Since we are working in the grand canonical ensemble, the total number of particles is not fixed, and we can write the partition function of the gas as:

$$Z = \sum_N^{\infty} \sum_{\{n_k\}} e^{-\beta \sum_k (E_k - \mu) n_k} \tag{1.3}$$

where we used that $N = \sum_k n_k$. The sum over $\{n_k\}$ corresponds to the sum over every configuration for which the relation $\sum_k n_k = N$ is satisfied, with fixed N. In order to extract the average occupation number of the state associated with the energy E_k from Eq. (1.3), we invoke the most striking feature about fermions: the *Pauli exclusion principle.* Since we can only accommodate at most one particle for each quantum state, the calculation of the partition function Z is greatly simplified. The average occupation number $\langle n_k \rangle^F$ of a fermionic state with wave vector k is found out to be [13]:

$$\langle n_k \rangle^F = \frac{1}{e^{\beta(E_k - \mu)} + 1} \tag{1.4}$$

In order to investigate the behaviour at zero temperature, we take the limit for $T \to 0$ of Eq. (1.4). The occupation number then takes the simple form:

$$\begin{cases} \langle n_k \rangle^F = 0 & \text{for } E_k > \mu \\ \langle n_k \rangle^F = 1 & \text{for } E_k < \mu \end{cases} \tag{1.5}$$

Therefore, the energy levels of the ideal Fermi gas at zero temperature are fully occupied up to an energy of μ. This defines a typical energy scale known as the *Fermi energy* E_F, which is the highest energy available for a particle of the gas. For non-interacting particles, we simply have:

$$E_F = \mu \tag{1.6}$$

and the *Fermi energy* is exactly equal to the chemical potential of the system. The distribution function corresponding to the occupation number reported in Eq. (1.4) is shown for different temperatures in Fig. (1.1): by increasing the system's temperature above zero higher energy levels start to be thermally occupied, and the $T \neq 0$ distributions show a smoother trend around μ with respect to the $T = 0$ case, where the energy distribution is represented by the step function reported in Eq. (1.5). If we finally take into account the spin quantum number S then each energy level will be occupied a number of times equal to the multiplicity of the spin, $g_s = (2S + 1)$. The total number of atoms con be written in terms of the average occupation number of Eq. (1.4) as follows:

$$N = g_s \sum_k \langle n_k \rangle^F \tag{1.7}$$

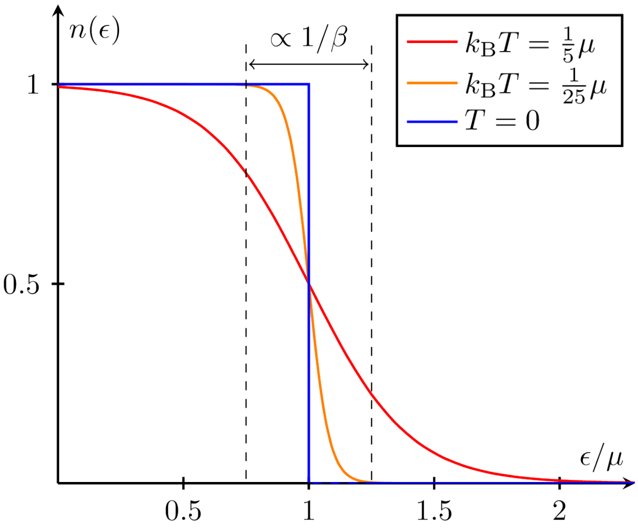

Figure 1.1: *Plot of the Fermi distribution for different temperatures. The smooth region for $T \neq 0$ near the Fermi energy has a typical width of order of $k_B T$. The $T = 0$ curve has the behavior predicted by Eq. (1.5); a step function, centered on $E_k = \mu$.*

If we now impose *periodic boundary conditions* on the single particle wave function, the sum in Eq. (1.7) approaches the integral in the k-space when $V \to \infty$, where V is the volume containing the system [33]:

$$N = \frac{g_s V}{(2\pi)^3} \int_{\mathbb{R}^3} \frac{d^3k}{e^{\beta(E(k)-\mu)} + 1} = \frac{g_s V}{(2\pi\hbar)^3} \int_{\mathbb{R}^3} \frac{d^3p}{e^{\beta(E(p)-\mu)} + 1} \tag{1.8}$$

where we wrote the integral of Eq. (1.8) in momentum space using the relation $p = \hbar k$. For an ideal Fermi gas of free particles, in the absence of a trapping potential, the occupation number reported in Eq. (1.4) does not depend on the particle position, but only on its momentum.

1.2 Non-interacting Fermi gas in a trapping potential

The presence of an external trapping potential inevitably affects the statistical properties of an ideal Fermi gas. In what follows we will extend the results of the previous section by considering a generic *trapping potential* $V_T(\vec{r})$, which depends only on the particle position. If the thermal energy $k_B T$ is much larger than the spacing between the quantum mechanical energy levels E, solutions of the eigenvalue equation:

$$\left(\frac{p^2}{2m} + V_T(\vec{r})\right)|E\rangle = E|E\rangle \tag{1.9}$$

then the occupation of a phase space cell $\{\vec{r}, \vec{p}\}$ is given by the following expression [13]:

$$f(\vec{r}, \vec{p}) = \frac{1}{e^{\beta(\frac{p^2}{2m} + V_T(\vec{r}) - \mu)} + 1} \tag{1.10}$$

The density distribution of the gas can be written in terms of the function $f(\vec{r},\vec{p})$ of Eq. (1.10) as follows:

$$n(\vec{r}) = \int_{\mathbb{R}^3} \frac{d^3p}{(2\pi\hbar)^3} f(\vec{r},\vec{p}) = -\frac{1}{\lambda_{dB}} Li_{3/2}\Big(-e^{\beta(\mu - V_T(\vec{r}))}\Big) \tag{1.11}$$

where $Li_z(n)$ is the polylogarithm of order n in the variable z, defined as:

$$Li_z(n) = \frac{1}{\pi^2} \int \frac{d^{2n}r}{e^{r^2}/z - 1} \tag{1.12}$$

while λ_{dB} is the *de Broglie* thermal wavelenght:

$$\lambda_{dB} = \sqrt{\frac{h^2}{2\pi m k_B T}} \tag{1.13}$$

The total number of particles N is finally given by the following integral:

$$N = \int_{\mathbb{R}^3} d^3r\, n(\vec{r}) \tag{1.14}$$

The *de Broglie* thermal wavelength λ_{dB}, introduced in Eq. (1.13), represents an important length scale in quantum physics as it allows to establish the importance of quantum effects in a gas. In fact, the regime of *quantum degeneracy* sets in when $\lambda_{dB} \approx d$, where d is the mean interparticle spacing: for non-interacting Fermi gases this phenomena happens for $T \approx T_F$, where $T_F = E_F/k_B$ is the *Fermi temperature.* If the cloud's temperature is smaller than T_F the wave functions of nearby particles overlap, and collective effects due to the statistics become dominant. The gas has to be described in terms of quantum statistics, the *Fermi-Dirac* or the *Bose-Einstein*, depending on the nature of the system. On the other hand, for temperatures much higher than T_F, we have $\lambda_{dB} << d$ and the gas must be treated as a classical one, being described by the *Maxwell-Boltzmann* distribution. The temperature at which this phenomena sets in is also known as the *degeneracy temperature* T_{deg}, and can be calculated from Eq. (1.13) as follows:

$$T_{deg} = \frac{n^{2/3}h^2}{2\pi m k_B T} \tag{1.15}$$

where $n = N/V$ is the mean density of the gas, which fixes the value of the interparticle distance $d = n^{-1/3}$. Typical values of the degeneracy temperature in ultracold atoms experiments are around $1\,\mu K$. In this range of temperatures, for fermions, the occupation of available phase space cells smoothly approaches unity without any sudden transition [13]:

$$\begin{cases} \lim\limits_{T\to 0} f(\vec{r},\vec{p}) = 0 & \text{for } \frac{p^2}{2m} + V_T(\vec{r}) > \mu \\ \lim\limits_{T\to 0} f(\vec{r},\vec{p}) = 1 & \text{for } \frac{p^2}{2m} + V_T(\vec{r}) < \mu \end{cases} \tag{1.16}$$

The density profile then assumes the following expression:

$$n(\vec{r}) = \frac{g_s}{(2\pi\hbar)^3} \int_{|\vec{p}|<\sqrt{2m(\mu - V_T(\vec{r}))}} d^3p = \frac{g_s(2m(\mu - V_T(\vec{r}))^{2/3})}{6\pi^2\hbar^3} \tag{1.17}$$

where we kept into account the spin degeneracy factor g_s. If the trapping potential is a slowly varying function of the position, we can individuate inside the trap a set of volumes small enough for $V_T(\vec{r})$ to be constant inside of them, where all the thermodynamic quantities are well-defined. Under such assumption, the inhomogeneous system is approximated as the sum of locally homogeneous systems. This is known as the *local density approximation.* For the non interacting trapped Fermi gas we can then define the following *local Fermi energy* $\epsilon_F(\vec{r})$, in order to keep into account the spatial dependence of the trapping potential $V_T(\vec{r})$:

$$\epsilon_F(\vec{r}) = \mu - V_T(\vec{r}) = E_F - V_T(\vec{r}) \tag{1.18}$$

where E_F is the trap averaged *Fermi energy.* We want to stress out that, even in the presence of an external potential, Eq. (1.6) is still valid in the *non-interacting* case. The presence of interactions between the particles of the gas may change the relation between the chemical potential μ and the trap averaged *Fermi energy* E_F. By substituting Eq. (1.18) inside the expression for the spatial density reported in Eq. (1.17), we find the following relation for the *local Fermi energy*:

$$\epsilon_F(\vec{r}) = \frac{\hbar^2}{2m}\left(\frac{6\pi^2 n(\vec{r})}{g_s}\right)^{2/3} \tag{1.19}$$

In a particular position $\vec{r}$ of the trap, the highest available momentum for a particle of the gas is the *local Fermi momentum* $k_F(\vec{r})$, which is related to the *local Fermi energy* by the relation:

$$p_F(\vec{r}) = \hbar k_F(\vec{r}) = \sqrt{2m\epsilon_F(\vec{r})} \tag{1.20}$$

We can compare the local Fermi energy $\epsilon_F(\vec{r})$ with the thermal energy $k_B T$ at finite $T < T_F$, in order to study the cloud shape and its temperature inside the trap. For the outer regions in the trap, where $k_B T >> \epsilon_F(\vec{r})$, the gas shows a classical density distribution:

$$n(\vec{r}) \propto e^{-\beta V(\vec{r})} \tag{1.21}$$

while in the inner part of the cloud where $k_B T << \epsilon_F(\vec{r})$ the density is of the zero-temperature form:

$$n(r) \propto (E_F - V_T(\vec{r}))^{2/3} \tag{1.22}$$

The polylogarithm function defined in Eq. (1.12) smoothly interpolates between the classical regime and the quantum one. We conclude that, for thermal clouds with temperature above T_F, a measurement of the cloud's size allows to probe directly the value of its temperature, while for cold Fermi clouds one needs to extract the temperature from the shape of the distribution's wings, since the density profile reported in Eq. (1.22) does not depend on temperature [13]. The general discussion provided in this paragraph is valid for any external trapping potential $V_T(\vec{r})$ acting on the atomic cloud. In Sec. 2.3 we will show how to calculate the *Fermi energy* E_F and the chemical potential μ of the cloud for the particular trapping geometry employed in our measurements, after discussing how the realization of an hybrid potential (different confinements along the vertical direction z and along the x-y plane) is carried out in the experiment (Secs. 2.1 and 2.2).

1.3 Interacting Fermi gases at low temperatures

Interparticle interactions in ultracold atom systems are responsible for a wide variety of interesting phenomena. On the one hand, interactions are necessary in order to achieve the superfluid state, as they are responsible for the presence of collective modes in the excitation spectrum that allows for superfluidity [32]. On the other hand, some experimental techniques actually need the presence of interactions: the process of *evaporative cooling* (App. A.2) exploits collisions between atoms in order to thermalize the system at very low temperatures. In this section we will discuss about interparticle interactions in the general framework of *quantum scattering theory*, along with an introduction on *Feshbach resonances*: the latter phenomena represents a powerful tool in ultracold atom experiments, as it allows to finely tune interactions within many-body systems.

1.3.1 Low-energy scattering theory

Since we are dealing only with neutral systems, the dominating interaction is the attractive *Van der Waals* force between atomic dipoles. These forces are usually described in terms of a *Lennard-Jones* (L-J) potential, which also keeps into account the repulsive *Coulomb* interaction between the electronic clouds:

$$V(r) = -\frac{C_6}{r^6} + \frac{C_{12}}{r^{12}} \tag{1.23}$$

where C_6 and C_{12} represent opportune coefficients, while r is the distance between the atoms. The spatial profile of this potential is shown below in Fig. 1.2.

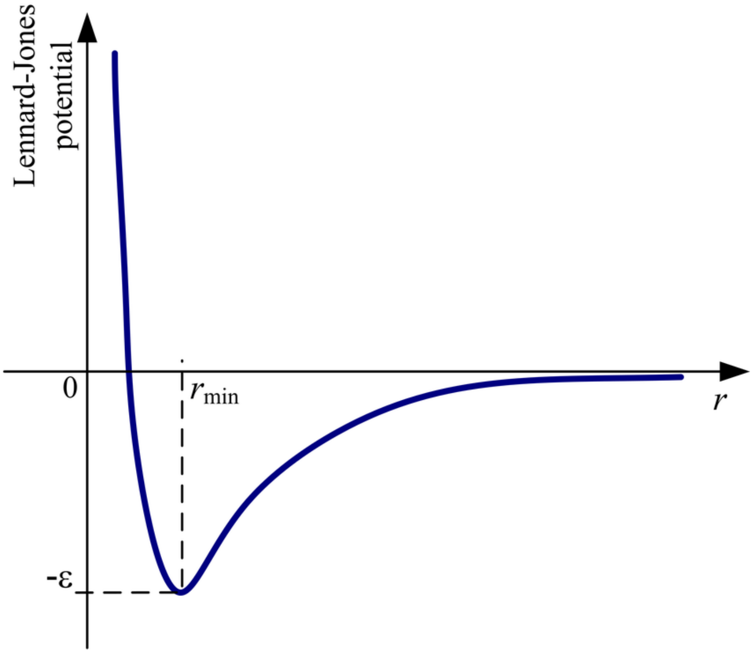

Figure 1.2: *Lennard-Jones potential as a function of the atoms distance* r*. The equilibrium position (minima of potential) is given by* r_{min}*, while* $-\varepsilon$ *is the potential depth. Figure taken from [34].*

The *interaction range* associated with the L-J potential reported in Eq. (1.23) constitutes a typical length scale, and will be denoted as r_0. The gas is said to be dilute when:

$$r_0 << d \tag{1.24}$$

a condition well fulfilled by ultracold quantum gases obtained by means of evaporative cooling techniques. In the notable case, for the present thesis, of a ^6Li ultracold gas, we obtain $r_0/d \approx 2.5 \cdot 10^{-3}$, such that the condition reported in Eq. (1.24) is satisfied. The diluteness condition allows one to consider only configurations involving two-body collisions, safely neglecting interactions between three or more particles [32]. We can therefore study scattering phenomena by considering two identical atoms, interacting only through the two-body interaction potential of Eq. (1.23). Using center-of-mass and relative variables, the total Hamiltonian can be written as a sum of two commutating terms:

$$H = \frac{P_{CM}^2}{2M} + \frac{p^2}{2m'} + V(r) = H_{CM} + H_r \tag{1.25}$$

where $M = 2\,m$ is the total mass, $m' = m/2$ is the reduced mass, while P_{CM} is the center-of-mass momentum and p is the relative momentum. Since the center-of-mass Hamiltonian $H_{CM} = P_{CM}^2/2M$ only describes the propagation of a free particle, the collision dynamics is entirely contained in the relative motion, described by $H_r = p^2/2m + V(r)$. The problem of collision between two particles is then reduced to a problem of scattering of a single particle of mass m' with an interaction potential $V(r)$. The two-body wave function, solution of the Schrödinger equation for the Hamiltonian reported in Eq. (1.25), can be thus factorized as:

$$\Psi(\vec{R}_{CM}, \vec{r}) = \psi(\vec{r})\, e^{i\vec{P}_{CM}\cdot\vec{R}_{CM}/\hbar} \tag{1.26}$$

where $\vec{R}_{CM}$ is the center-of-mass coordinate. If we impose a well defined incident positive energy $E = \hbar^2 k^2/2\,m'$, the Schrödinger equation takes the following form:

$$\left(\frac{\hbar^2\nabla^2}{2m'} + \frac{\hbar^2 k^2}{2m'}\right)\psi(\vec{r}) = V(\vec{r})\,\psi(\vec{r}) \tag{1.27}$$

Eq (1.27) can be solved formally by introducing the outgoing *Green's function*, which satisfy the relation:

$$(\nabla^2 + k^2)\, G^\dagger(\vec{r} - \vec{r}\,') = \delta(\vec{r} - \vec{r}\,') \tag{1.28}$$

By substitution of Eq. (1.28) into Eq. (1.27) we arrive at the *Lippmann-Schwinger* integral equation:

$$\psi(\vec{r}) = \phi_0(\vec{r}) + \frac{2m'}{\hbar^2}\int d^3\vec{r}\,' G^\dagger(\vec{r} - \vec{r}\,')\, V(\vec{r}\,')\,\psi(\vec{r}\,') \tag{1.29}$$

where $\phi_0(\vec{r})$ is the solution of Eq. (1.27), obtained in the absence of an interaction potential. The asymptotic solution of Eq. (1.29), very far from the collision region, can be written as [35]:

$$\psi(\vec{r}) \propto e^{i\vec{k}\cdot\vec{r}} + f(\theta, \mathbf{k})\,\frac{e^{i\vec{k}\cdot\vec{r}}}{r} \tag{1.30}$$

In Eq. (1.30) the plane wave represents the wave function of the incoming particle, while the spherical wave represents the scattered wave function due to the presence of the interaction potential $V(r)$. This second term is multiplied by the *scattering amplitude* $f(\theta, \mathbf{k})$, which represents the probability for the particle to be scattered at an angle θ with respect to the incoming direction. Since we are dealing only with elastic collisions, where energy conservation holds, the wave vector $\mathbf{k}$ of the incoming particle does not change in magnitude but only in direction. The *scattering amplitude* is related to the *differential cross section* by the following:

$$\frac{d\sigma}{d\Omega} = |f(\theta, \mathbf{k})|^2 \tag{1.31}$$

where Ω is the solid angle. We can expand both the incoming and the scattered wave functions on the spherical harmonics basis:

$$\psi(\vec{r}) = \sum_{l=0}^{\infty} \sum_{m=-l}^{l} Y_l^m(\theta, \phi) \frac{u_{k,l,m}(r)}{r} \overset{m=0}{=} \sum_{l=0}^{\infty} Y_l^0(\theta) \frac{u_{k,l,0}(r)}{r} \tag{1.32}$$

where in the second passage we have taken into account the spherical symmetry of the *Lennard-Jones* potential (see Eq. (1.23)), by imposing $m = 0$. If we employ the expansion reported in Eq. (1.32) on the system's wave function, we obtain the following radial Schrödinger equation:

$$\left(\frac{d^2}{dr^2} + k^2 - \frac{l(l+1)}{r^2} - \frac{2m'}{\hbar^2} V(r) \right) u_{k,l,0}(r) = 0 \tag{1.33}$$

where an extra term, the centrifugal barrier $\hbar^2 l(l+1)/2m'r^2$, is added to the interaction potential. We can calculate the scattering amplitude $f(\theta, \mathbf{k})$ from the scattered wave function reported in Eq. (1.30) by substituting Eq. (1.32), obtaining the following expression:

$$f(\theta, \mathbf{k}) = \frac{1}{k} \sum_l (2l+1) P_l(\theta) e^{i\delta_l(k)} \sin\left(\delta_l(k)\right) \tag{1.34}$$

where $P_l(\theta) = \sqrt{\frac{4\pi}{2l+1}} Y_l^0(\theta)$, while $\delta_l(k)$ is the phase shift imprinted on the scattered wave function by the collision. In order to write down the total cross section σ from Eq. (1.31), we must keep into account the indistinguishability of the particles, which is mandatory if we want to describe a real Fermi gas. We recall that, for fermions, the *Pauli exclusion principle* must hold, and therefore the total wave function describing a system of two identical fermionic particles must be anti-symmetric under the exchange of a complete set of quantum numbers. If we ignore the spin degree of freedom, this condition reads:

$$\psi(\vec{r_1}, \vec{r_2}) = -\psi(\vec{r_2}, \vec{r_1}) \tag{1.35}$$

This property implies that two different collisions between identical particles, resulting in final scattering angles of θ and $\theta + \pi$ respectively, are indistinguishable events, as shown in Fig. 1.3.

The scattered wave function thus assumes the following anti-symmetrized form:

$$\psi(\vec{r}) \propto \frac{1}{\sqrt{2}} \left[\left(e^{i\vec{k}\cdot\vec{r}} + f(\theta, \vec{k}) \frac{e^{i\vec{k}\cdot\vec{r}}}{r} \right) - \left(e^{i\vec{k}\cdot\vec{r}} + f(\theta + \pi, \vec{k}) \frac{e^{i\vec{k}\cdot\vec{r}}}{r} \right) \right] \tag{1.36}$$

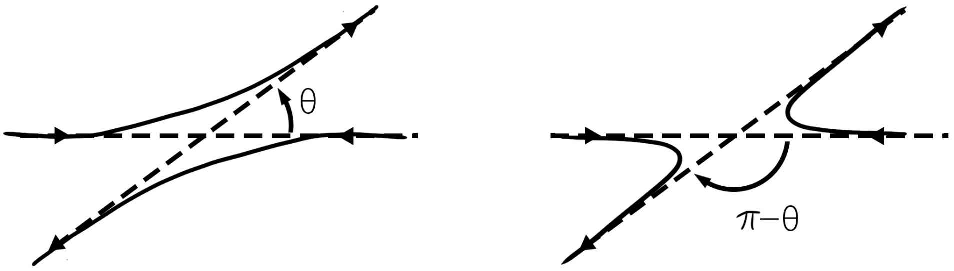

Figure 1.3: *Two scattering processes, yielding the same final state after the collision of identical particles.*

The differential cross-section is anti-symmetrized as well:

$$\frac{d\sigma}{d\Omega} = \frac{1}{2}\left| f(\theta, \mathbf{k}) - f(\theta + \pi, \mathbf{k}) \right|^2 \tag{1.37}$$

We can obtain the total cross-section for the scattering of identical fermions by integrating Eq. (1.37) with respect to the solid angle Ω:

$$\sigma_F = \frac{8\pi}{k^2} \sum_{l\ odd} (2l+1)\ \sin\left(\delta_l(k)\right)^2 \tag{1.38}$$

so that the anti-symmetry property of the total wave function causes the presence of only odd l contributions to the total scattering cross-section. This implies that, at low temperature, interactions between identical fermions are suppressed. In fact, the centrifugal term in Eq. (1.33) inhibits collisions for $l > 0$ of the low energy incoming particles, so that only the *s-wave* scattering ($l = 0$) is permitted. As a consequence, cold identical fermions do not interact with each other as the s-wave scattering is suppressed by statistics, while higher angular momentum collisions are prevented by the low-energy scale of the system. To evaporatively cool fermionic samples, two different hyperfine states have to be employed so that collisions between fermions in opposite spin state can cause thermalization of the sample. Therefore, from now on, we will consider scattering processes to happen between fermions in different spin state, the interactions of which are not suppressed by statistic. We can write the asymptotic solution of Eq. (1.33) as follows:

$$u_{k,0,0}(r) \approx \sin\left(kr - \delta_0(k)\right) \tag{1.39}$$

In the low-energy limit, the scattering amplitude $f(\theta, \mathbf{k})$ reported in Eq. (1.34) tends to a constant value, independent of both the particle energy E and the scattering angle θ [32]:

$$f(\theta)_{E\to 0} = -a \tag{1.40}$$

where we introduced the s-wave *scattering length* a, defined as:

$$a = -\lim_{k\to 0} \frac{\tan\left(\delta_0(k)\right)}{k} \tag{1.41}$$

As we discussed before, in the fermionic case, the low-energy scattering cross section σ_F tends to zero for identical particles. On the other hand, if we consider a Bose gas at low temperatures, with the same calculations we find the following result:

$$\sigma_B = 8\pi a^2 \tag{1.42}$$

which again is independent of energy. The low energy scattering process is therefore fully described by a single parameter: the s-wave scattering length a, even for fermionic systems. In cold atom systems, the scattering length is typically orders of magnitude larger than the *Lennard-Jones* potential range r_0, allowing for the approximation of interatomic interactions with a contact potential:

$$V_p(r) = \frac{4\pi\hbar\, a}{m}\delta(r) \tag{1.43}$$

where $\delta(r)$ is the Dirac delta function. The interaction potential reported in Eq. (1.43) describes attractive interactions for $a < 0$, while repulsive interactions correspond to $a > 0$.

1.3.2 Magnetic Feshbach resonances

In the absence of external fields, the value of the s-wave scattering length is fixed for a certain atomic species, and it only depends on the details of the interatomic potential shown in Eq. (1.23). Let us consider a generic scattering event between two particles, A and B:

$$A + B \to A' + B' \tag{1.44}$$

with final products A' and B'. The combination of the atomic species and the quantum numbers of the particles before and after the collision event is referred to as a scattering *channel*. A particular channel is said to be *open* if it is energetically accessible, while is referred to as *closed* when prohibited by means of energy conservation. If we have two particles in the open channel which mutually interacts via a potential $V_{bg}(r)$, their total energy E is:

$$E = T + V_{bg}(r) + \Delta(\mathbf{P}) \tag{1.45}$$

where T is the total kinetic energy in the relative frame, $\Delta(\mathbf{P})$ is the contribution to E due to couplings with an external field $\mathbf{P}$, and r is the relative coordinate. Consider now a second channel associated with the potential $V_c(r)$, closed for large values of r, which admits a certain bound state with energy E_d. When the energy in the open channel of Eq. (1.45) is resonant with the energy of the bound state, as shown in Fig. 1.4, a *Feshbach resonance* occurs, namely for:

$$E_d \approx T + V_{bg}(r) + \Delta(\mathbf{P}_0) \tag{1.46}$$

where P_0 is the field value which satisfy Eq. (1.46). In ultracold atom systems, the interaction potential between two particles depends on the spin configuration. For alkali atoms we can identify the open channel, populated before the scattering event, with the singlet state, while the triplet state corresponds to the closed channel. These states will, in general, have a different magnetic momentum υ, such that the presence of an external magnetic field $\mathbf{B}$ causes a relative energy shift of $\Delta\upsilon\,\mathbf{B}$ with respect to the zero-field case. If Eq. (1.46) is satisfied for a certain value of the magnetic field B_0 the s-wave scattering

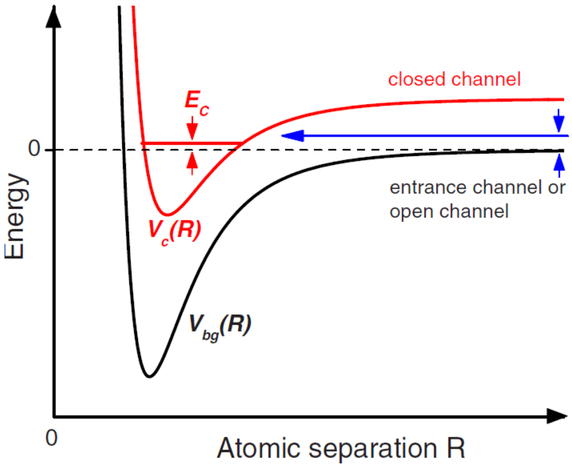

Figure 1.4: *Feshbach resonance between open (black) and closed (red) channels, for a low-energy collision process.*

length a diverges, giving rise to a *Feshbach resonance*. Close to a resonance, the scattering length depends on the magnetic field $\mathbf{B}$ as:

$$a(B) = a_{bg}\left(1 - \frac{\Delta B}{B - B_0}\right) \tag{1.47}$$

where a_{bg} is the scattering length at zero field (*background* scattering length), while ΔB is the resonance width and B_0 is the resonance center. The behavior described by Eq. (1.47) is plotted in Fig. 1.5; the application of an external magnetic field thus reflects on the value of the s-wave scattering length a, which can diverge (*strongly interacting* gas), change sign, or even go to zero (*non-interacting* gas).

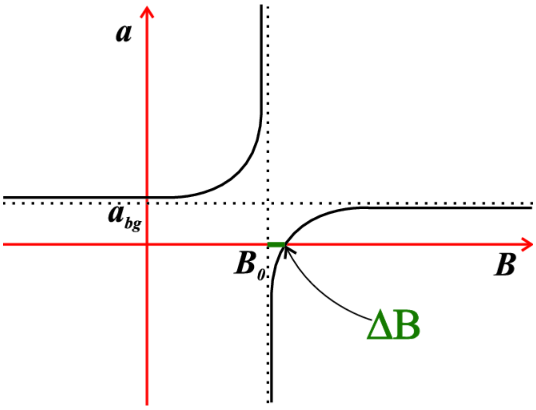

Figure 1.5: *Scattering length a as a function of the applied magnetic field B. A divergence is expected at the resonance center B_0, where the Feshbach resonance occurs.*

We want to stress out that, in spite of the divergence of the parameter a, no physical quantity associated with the scattering event actually diverges. For example, the total scattering cross section for identical fermions in different spin states becomes:

$$\sigma \approx \frac{8\pi a^2}{1 + k^2 a^2} \xrightarrow{a\to\infty} \frac{8\pi}{k^2} \tag{1.48}$$

and the interparticle interactions are the strongest possible.

1.4 BEC-BCS Crossover and Unitary Fermi gas

As discussed in the previous section, *Feshbach resonances* represent a powerful tool for modulating and controlling interactions in ultracold atoms experiments. Their most spectacular application in quantum Fermi gases is that they allow for the exploration of the so called BEC-BCS crossover, where the tunability of the scattering length a plays a fundamental role; another key parameter which characterizes the nature of interactions in these systems is the *Fermi wave vector* k_F, defined in Eq. (1.20). Under a certain critical temperature T^* a coupling between atoms in different spin states emerges, with different behavior across the resonance. The result is the creation of an atom pair, which size and nature depend on the parameter $1/(k_F\, a)$.

1.4.1 BEC Regime

Interactions are *weak* and *repulsive* when the Fermi wave vector k_F and the s-wave scattering length a satisfy the following condition:

$$1/(k_f\, a) >> 1 \tag{1.49}$$

In this regime, when the temperature is lower than the coupling critical temperature T^*, atom pairs in the gas form tightly-bound molecules, the binding energy of which depends on the scattering length as follows:

$$E_b = -\frac{\hbar^2}{ma^2} \tag{1.50}$$

For temperatures below a second critical temperature, $T_c < T^*$, the molecular gas undergoes Bose-Einstein condensation (BEC). The many-body wave function of the condensate, which describes the ground-state of the system, is the solution of the *Gross-Pitaevskij* mean field equation [13]:

$$\left(-\frac{\hbar^2\nabla^2}{2m} + V_T(\vec{r}) + g|\psi(\vec{r},t)|^2\right)\psi(\vec{r},t) = i\hbar\frac{d\psi(\vec{r},t)}{dt} \tag{1.51}$$

where $V_T(\vec{r})$ represents the trapping potential, while g is a parameter characterizing intermolecular interactions:

$$g = \frac{4\pi\hbar^2 a_M}{M} \tag{1.52}$$

where $M = 2\,m$ is the mass of a pair, while $a_M \approx 0.6\,a$ is the scattering length of the molecular gas. Eq. (1.51) is valid only for a weakly interacting gas, for which $n_M a_M^3 << 1$. At equilibrium the ground-state wave function takes the following form:

$$\psi(\vec{r},t) = \psi(\vec{r})e^{-i\mu_M t/\hbar} \tag{1.53}$$

where $\psi(\vec{r})$ is the stationary (i.e. time independent) solution of Eq. (1.51), while μ_M is the molecular gas chemical potential, which can be identified with the energy of the ground state. The stationary solution $\psi(\vec{r})$ is related to the total number of atoms N by the following normalization condition:

$$N = \int_{\mathbb{R}^3} |\psi(\vec{r})|^2 d^3 r \tag{1.54}$$

such that we can write the cloud density as $n(\vec{r}) = |\psi(\vec{r})|^2$. We can distinguish between two noteworthy regimes:

1. *Ideal gas limit*, where $gn << -\hbar^2\nabla^2/2m + V_T(\vec{r})$ and the density distribution $n(\vec{r})$ is the same as the non-interacting case.

2. *Thomas-Fermi limit*, in which $gn >> -\hbar^2\nabla^2/2m + V_T(\vec{r})$. From the Gross-Pitaevskij Eq. (1.51) and its stationary solution (Eq. (1.53)) we can calculate the density profile $n(\vec{r})$ of the cloud, neglecting the kinetic term:

$$n(\vec{r}) = \frac{M(\mu - V_T(\vec{r}))}{4\pi\hbar^2 a_M} \tag{1.55}$$

From Eq. (1.55) we see that, if the trapping potential is of the an harmonic oscillator type, ($V_T(\vec{r}) \sim 0.5\, m\, \omega^2 r^2$), then the cloud density profile is predicted to be parabolic. An important quantity which can be defined in the context of Bose-Einstein condensates, starting from considerations regarding its quasi-particle spectra [32], is represented by the *healing length* ξ:

$$\xi = \frac{\hbar}{\sqrt{2M\mu}} \tag{1.56}$$

The reciprocal of the healing length ξ quantifies the value of the wave vector k for which the dispersion law of quasi-particles transitions from a linear phononic branch $E(k) \propto k$ to a parabolic law $E(k) \propto k^2$. The healing length represents the minimum distance over which the order parameter of the BEC, i.e. its macroscopic wave function Ψ_0 (see Eq. (1.74)), can adjust to changes in the external potential $V_T(\vec{r})$: in other words, it estimates the spatial extension of the condensate's wave function.

1.4.2 BCS Regime

Interatomic interactions are *weak* and *attractive* if the following condition holds:

$$1/(k_f\, a) << -1 \tag{1.57}$$

In this regime, under the critical temperature T_c atoms bound together to form *Cooper pairs*; at the same temperature, the system also undergoes a phase transition to the *superfluid* state, becoming a BCS gas. Similarly to the non-interacting case, discussed in Secs. 1.1 and 1.2, the chemical potential μ of a BCS superfluid is approximately equal to its Fermi energy E_F [13]:

$$\mu \approx E_F \tag{1.58}$$

This is a consequence of the fact that only a small fraction of particles around the Fermi sphere with momentum $k \sim k_F = \sqrt{2mE_F}/\hbar$ is actually involved in the pairing. When the *Cooper instability* sets in and Cooper pairs proliferate in the system an energy gap Δ appears in the excitation spectrum of the *Fermi sea*, which decreases exponentially with the interaction strength [13]:

$$\Delta = \frac{8}{e^2} E_F e^{\pi/2k_F a} \tag{1.59}$$

and represents a phenomenological estimate of the pair's binding energy. The critical temperature T_c also depends in a similar way on the scattering length [36]:

$$\frac{T_c}{T_F} = 0.28\, e^{\pi/2k_F a} \tag{1.60}$$

We stress out that, since the lowest accessible temperatures are of order of $T/T_F \sim 0.1$, it is experimentally impossible to prepare a weakly interacting BCS superfluid which satisfies the condition presented in Eq. (1.57).

1.4.3 Unitary Fermi gas

When the *Feshbach resonance* occurs we have:

$$(1/k_F a) \longrightarrow 0 \tag{1.61}$$

and interparticle interactions become the strongest allowed for the system. The resulting ultracold gas is called *unitary Fermi gas* (UFG). The pairs which form under the critical temperature T^* have a size comparable with the interatomic distance $d \approx n^{-1/3} \sim k_F$, similarly to *Cooper Pairs* in high T superconductors. Since the scattering length diverges, the only relevant length scale is the interatomic distance d itself, while the only relevant energy scale is the *Fermi energy* E_F:

$$E_F = \frac{\hbar^2 k_F^2}{2m} \tag{1.62}$$

Therefore, the UFG properties do not depend on the nature of its constituents, and the unitary atomic gas shares a universal behavior with those composed by neutrons in neutron stars, or quark-gluon plasma [37]. As a result, the UFG is a scale-invariant system described by a universal equation of state depending only on the dimensionless parameter $q = \beta\mu = \mu/k_B T$ [38]. The chemical potential μ for an homogeneous (i.e. non-trapped) gas is therefore found to be proportional to the *Fermi energy* E_F defined in the non-interacting case, through a universal parameter:

$$\mu = \xi\, E_F \tag{1.63}$$

where ξ is the Bertsch parameter, which in general depends on the system temperature and spin polarization. For a spin-balanced gas at zero-temperature it has been measured to be $\xi \approx 0.37$ [39]. If the atomic cloud is spatially confined inside a trap, Eq. (1.63) can be modified to a power law of ξ, such that $\mu = \xi^n\, E_F$, where the index n depends, in general, on the particular trapping potential $V_T(\vec{r})$ employed. In Sec. 2.3 we will show how to calculate the index n for the peculiar trap geometry adopted in the experiment. The equation of state describing the unitary Fermi gas can be written as follows:

$$n = \frac{1}{\lambda_{dB}^3} f_n(q) \tag{1.64}$$

where λ_{dB} is the *de Broglie* thermal wavelength, while $f_n(q)$ is a piecewise-defined function of the parameter q [13]:

$$\begin{cases} f_n(q) = \sum_{b=0}^{4} s\, b_s e^{sq} & \text{for } q < -1.5 \\ f_n(q) = -Li_{3/2}(-e^q)F(q) & \text{for } -1.5 < q < 3.9 \\ f_n(q) = \frac{4}{3\sqrt{\pi}}\left[(\frac{q}{\xi})^{3/2} - \frac{\pi^4}{480}(\frac{3}{q})^{5/2}\right] & \text{for } q > 3.9 \end{cases} \tag{1.65}$$

where b_s are expansion coefficients extracted from virial theorem, known up to the 4-th order, $Li_{3/2}$ is the polylogarithm of order 3/2 and $F(q)$ is a universal function of q. The behavior of the ultracold Fermi gas along the BEC-BCS crossover, explored as a function of the parameter $(k_F a)^{-1}$, is reported in Fig. 1.6.

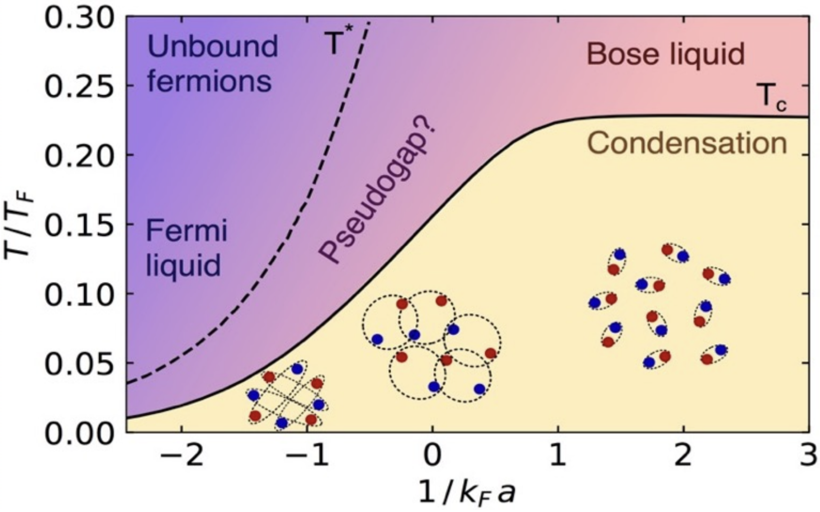

Figure 1.6: *Phase diagram for the BEC-BCS crossover of an homogeneous fermionic gas, where the critical temperatures T^* and T_c for pairing and condensation respectively are reported, as a function of $(k_F a)^{-1}$. The intermediate region of $T_c < T < T^*$, where pairs are already formed but not yet condensed, is called pseudogap. When the temperature is lowered below T_c, atom pairs undergo to condensation, giving rise to different fermionic superfluids. Image taken from [40].*

1.4.4 Polytropic approximation

Across the whole BEC-BCS crossover, the chemical potential μ can be written, under the local density approximation discussed in Sec. 1.2, as a polytropic law of the density profile $n(\vec{r})$ plus the trapping potential term $V_T(\vec{r})$:

$$\mu(\vec{r}) = V_T(\vec{r}) + g_\gamma n(\vec{r})^\gamma \tag{1.66}$$

where γ and g_γ are opportunely chosen coefficients, depending on the particular interactions considered. We can derive the density profile from Eq. (1.66),

Table 1.1: *Expressions of the coefficients γ and g_γ for the different interaction regimes of the BEC-BCS crossover.*

Regime	γ	g_γ
BEC	1	$4\pi\hbar^2 a_M/M$
BCS	2/3	$\hbar^2(6\pi^2)^{2/3}/2m$
UFG	2/3	$\xi\hbar^2(6\pi^2)^{2/3}/2m$

obtaining:

$$n(\vec{r}) = max\left(0, \frac{\mu - V_T(\vec{r})}{g_\gamma}\right)^{1/\gamma} \tag{1.67}$$

Eq. (1.67) allows to cast the density profile $n(\vec{r})$ in a compact form, valid through the entirety of the BEC-BCS crossover, regardless of the nature of interparticle interaction [13]. The desired case can be reproduced by inserting the opportune value of the coefficients γ and g_γ inside Eq. (1.67): their expressions are reported in Tab. 1.1, for the various regimes of the resonance.

1.5 Superfluidity in Fermi gases

Superfluidity is one of the most striking properties exhibited by ultracold Fermi gases, similiar to superconductivity in charged Fermi systems. Superfluids have shear viscosity equal to zero and can flow through narrow capillaries or slits without dissipating energy, this property being directly connected with their excitation spectrum. In the present section, we will introduce the main theoretical result concerning superfluids, the *Landau's criterion* for superfluidity, and discuss about the behavior of the critical velocity v_c along the BEC-BCS crossover. We conclude with an introduction of the main mechanisms of dissipation in a Fermi superfluid: sound waves, pair breaking, and vortex nucleation.

1.5.1 Landau's criterion for superfluidity

Let us consider a uniform fluid at zero temperature, which flows along a capillary at constant velocity v. We also suppose that dissipative processes can only take place through the creation of elementary excitations. In the reference system of the capillary, before the emission of the excitation, the total energy can be written as:

$$E = E_0 + \frac{1}{2}Mv^2 \tag{1.68}$$

where E_0 is the ground-state energy of the superfluid, while M is the mass of the whole fluid. If an elementary excitation with momentum p and energy $\epsilon(\vec{p})$ is emitted the energy becomes, assuming momentum conservation:

$$E \approx E_0 + \epsilon(\vec{p}) - \vec{p}\cdot\vec{v} + \frac{1}{2}Mv^2 \tag{1.69}$$

Eq. (1.69) shows that the appearance of the excitation causes a change in the total energy of $\Delta E = \epsilon(\vec{p}) - \vec{p}\cdot\vec{v}$. The spontaneous creation of an excitation is permitted only if the process is energetically favourable, i.e. if the total energy decreases ($\Delta E < 0$). In this case, the flow of the fluid is unstable and its kinetic energy will be converted into heat. If we impose this process to be unfavourable ($\Delta E > 0$) *Landau's criterion* for superfluidity follows:

$$v < v_c = \min_p \left(\frac{\epsilon(\vec{p})}{p} \right) \tag{1.70}$$

which ensures that the fluid can flow without any friction inside the capillary if the relative velocity between them is smaller than the critical velocity v_c. The *superfluid fraction* f can be introduced to characterize the portion of the system which shows a superfluid behavior:

$$f = \frac{n_s}{n} \tag{1.71}$$

where n is the gas density while n_s is the superfluid density. We want to stress out that this is an independent quantity from the *condensed fraction*, which describes the number of atoms that undergo the phenomena of macroscopic occupation of the system's ground state. Ultracold gases can show superfluidity even without being condensed, like for example a two-dimensional Bose gas; viceversa, a fully condensed system is not necessarily superfluid. From *Landau's criterion*, reported in Eq. (1.70), we see that an ideal non-interacting gas cannot achieve superfluidity because an eventual excitation would correspond to a spectra of the free-particle form, $\epsilon(\vec{p}) = p^2/2m$, which yields $v_c = 0$. The interacting Fermi gas is instead fully superfluid at $T = 0$, regardless of the interaction regime. For crossover Fermi superfluids, as in Bose gases, low-frequency excitations correspond to a phononic branch of sound waves, which energy can be calculated from hydrodinamic theory [32]. For higher energies pair-breaking mechanisms set in, creating fermionic excitations. Along the BEC-BCS crossover the interplay between these two contributions gives rise to different behaviors, depending on the interaction. The excitation spectrum of an ultracold Fermi gases, connected with superfluidity, has been deeply investigated in recent experiments [41]. In the BCS gas the transition between the phononic branch and the continuum of single-particle excitations already occurs at low energies, while in the BEC regime the scenario is different, with the phonon branch extending up to higher frequencies. For a UFG the system shows an intermediate behavior, where the phonon branch survives up to energies comparable with the Fermi energy. The minimum energy needed to break a fermionic pair can be calculated by doubling the energy required to add or remove a single fermion to the condensate. In the BCS limit this energy coincides with the *energy gap* Δ, which is exponentially suppressed with $(k_F a)^{-1}$. Thus, pair breaking excitations are the lowest energy excitations in the BCS side of the crossover, where the critical velocity can be calculated from Eq. (1.70) by substituting $\epsilon(\vec{p}) \approx \Delta$, and by considering wave vectors of order of the *Fermi wave vector* k_F:

$$v_c^{BCS} = \frac{\Delta}{\hbar k_F} \tag{1.72}$$

where we used that $\vec{p} = \hbar \vec{k}$. In the BEC regime the energy needed to remove a single particle from the system is $\sqrt{\Delta^2 + \mu^2}$. This corresponds to a pair-breaking energy which is much higher with respect to the BCS case, and other kinds of excitations dominate at low energy, like sound modes. In the BEC limit the critical velocity coincides with the sound velocity c_s, which in Bogoliubov theory is predicted to be [32]:

$$v_c^{BEC} = c_s = \sqrt{\frac{g n_B}{m_B}} = \sqrt{\frac{4\pi a \hbar^2 n_B}{m_B^2}} \tag{1.73}$$

From the weakly interacting BEC side of the resonance the speed of sound c_s increases with increasing interactions, up to a maximum value $v_c = v_F/\sqrt{3}$. In the BCS regime, where the main dissipation mechanism is represented by pair-breaking phenomena, the velocity of the sound modes is approximately constant, $c_s \approx v_F/\sqrt{3}$ (*Bogoliubov-Anderson* modes) [36], while the critical velocity increases when approaching unitarity as in the BEC case. The two trends smoothly connect to each other near the strongly-interacting unitary regime, where the superfluid is in the most stable configuration and the critical velocity reaches its maximum value, as shown in Fig. 1.7.

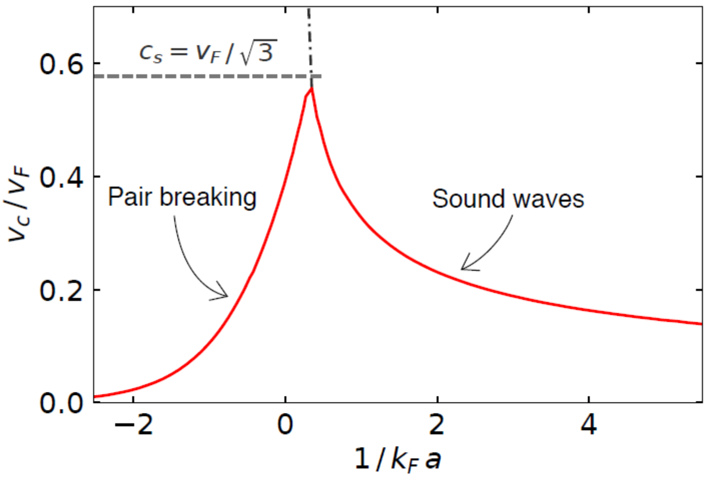

Figure 1.7: *Critical velocity of fermionic superfluids in the BEC-BCS crossover, in units of the Fermi velocity $v_F = \sqrt{2E_F/m}$. Note that the peak value of the critical velocity across the crossover is slightly towards the BEC side. Figure adapted from [13].*

In real systems the measured v_c is always lower than the expected theoretical value due to the presence of additional dissipation mechanisms; a notable one is the creation of a vortex-antivortex pair, which nucleate within the superfluid and cause local density perturbations.

1.5.2 Vortex excitations in superfluids

The long range order which sets in during the condensation phenomena of the fluid causes its motion to be irrotational, dramatically affecting its rotation dynamics with respect to a collisional hydrodynamic gas, for which rotational components in the velocity are allowed. Let us consider a weakly-interacting Bose gas, its ground state wave function being described by the solution of Eq. (1.51) (*Gross-Pitaevskij*). Such a solution can be written in the form:

$$\Psi_0(\vec{r}) = |\Psi_0|\, e^{iS(\vec{r})} \tag{1.74}$$

where $|\Psi_0| = \sqrt{n_0}$ is the order parameter, n_0 is the density of the condensate, and $S(\vec{r})$ is a global phase, reflecting the spontaneous breaking of gauge symmetry which occurs during the condensation phenomena. The velocity of the condensate can be written as the gradient of the phase $S(\vec{r})$, as shown in [32]:

$$v = \frac{\hbar}{2m} \vec{\nabla} S(\vec{r}) \tag{1.75}$$

such that the irrotationality condition holds:

$$\vec{\nabla} \times \vec{v} = 0 \tag{1.76}$$

When set into rotation a superfluid does not rotate like a rigid body, but the externally imparted angular momentum causes the emission of vortex excitations, which circulation is quantized. Let us calculate the circulation of the velocity reported in Eq. (1.75), over a closed contour:

$$\Gamma = \oint \vec{v} \cdot d\vec{l} = \frac{\hbar}{m} \oint \vec{\nabla} S(\vec{r}) d\vec{l} = \frac{\hbar}{m} \Delta S(\vec{r}) = w \cdot \frac{h}{m} \tag{1.77}$$

where $\Delta S(\vec{r})$ is the phase variation along the vortex line. Since the macroscopic wave function shown in Eq. (1.74) has to be single valued the phase must change by $2\pi w$, where w is an integer number, known as *winding number*; this leads to a quantized circulation. Eq. (1.77) shows that the irrotationality criterion associated with the occurrence of superfluidity is satisfied everywhere, except on the line of the vortex [32]. A quantized vortex is therefore associated with the appearence of a singularity in the superfluid, where the order parameter $\sqrt{n}$ vanishes. At large distances from the vortex line the density of the gas must approach its unperturbed uniform value n. The core of the vortex line, where the density is perturbed in a significant way, has a radius size comparable with the healing lenght ξ introduced in Eq. 1.56, which for fermionic superfluids of ^{6}Li is of the order of $\xi \sim 1\,\mu$m. In our system, vortex excitations are best observed in the BEC regime: as we move towards the BCS side of the crossover, where the vortex's size is roughly given by $1/k_F$, the creation of vortices stops affecting in a significant way the density of the superfluid as they can be very small, making very difficult to detect them with *in-situ* measurements.

1.6 The Josephson effect

The Josephson effect in superconductors occurs due to tunneling events of *Cooper pairs*, passing through a thin insulating barrier which separates two superconducting metals, and was first predicted in 1962 by Brian D. Josephson [3]. The associated microscopic device, known as Josephson junction, was realised one year later by P.W Anderson and J.M Rowell [5]. Nowadays, Josephson junctions have important applications in modern quantum technologies, where their peculiar transport properties are widely employed: notable examples are represented by superconducting quantum interference devices (SQUIDs) [42], superconducting qubits [43], and RSFQ digital electronics [44]. In ultracold atoms experiments the superfluid analogous of a superconducting junction, the atomic Josephson junction, can be realized by bisecting the condensate with a thin optical barrier, this procedure being usually carried out through focused laser beams. In the present section we will discuss the Josephson effect in both cases, superconducting metals and ultracold atoms, highlighting similiarities and differences. We conclude this chapter with a description of the phenomenologicals RSJJ and RCSJJ models, both employed to characterize the device in the framework of electronic circuits: in particular, we will explain how **Shapiro steps** appear in the $I - \Delta V$ characteristic of the junction, in the physical context of the *tilted washboard potential.*

1.6.1 Josephson effect in superconductors

Superconductors, as superfluids, can be associated with a macroscopic wave function in order to describe the condensed state of weakly bound *Cooper pairs* which start to appear in a metal at very low temperatures:

$$\Psi(\vec{r}) = |\Psi| \, e^{i\phi(\vec{r})} \tag{1.78}$$

where the amplitude $|\Psi|$ results proportional to the square root of the superconducting electrons density, while $\phi(\vec{r})$ represents a global phase. This wave function plays the role of an order parameter for the superconductor-normal metal phase transition. Superconducting Josephson junctions are electronic devices made up of two superconducting metals, separated by an insulating barrier, which has to be thin enough in order to allow the order parameters of the superconductors to overlap in the barrier region, as shown in Figure 1.8.

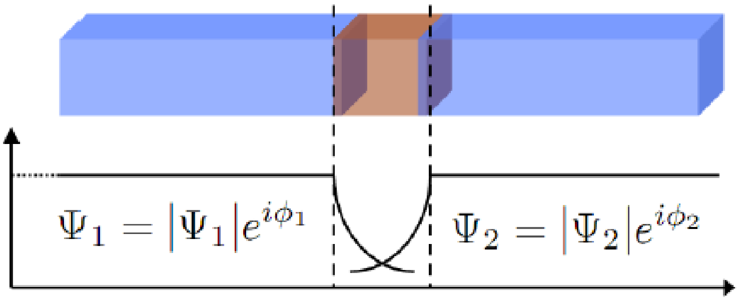

Figure 1.8: *Schematic diagram of a solid-state Josephson junction, where two superconducting electrodes are separated by a thin layer of insulator.* Ψ_1 *and* Ψ_2 *represent the macroscopic wave functions associated with each superconductor.*

The coupling between the two superconductors is able to drive a dissipationless super-current I_s, merely sustained by their relative phase difference $\phi = \phi_1 - \phi_2$, which flows without resistance inside the junction (i.e. without developing a finite ΔV). In order to derive an expression for I_s, let us consider the wave functions ψ_i, solutions of the *Schrödinger* equation for the uncoupled superconductors:

$$i\hbar \frac{d\psi_i}{dt} = E_i \psi_i \tag{1.79}$$

where $i = 1, 2$ is the index labelling each superconductor. The total wave function for the superconducting electrons within the junction can be written as a superposition of the wave functions ψ_i:

$$\Psi(\vec{r},t) = \sum_{i=1}^{2} C_i(t)\psi_i \tag{1.80}$$

We can substitute Eq. (1.80) inside the time-independent *Schrödinger* equation for the whole junction, which takes the form:

$$i\hbar\frac{d\Psi(\vec{r}),t}{dt} = H\Psi(\vec{r},t) \tag{1.81}$$

where the Hamiltonian H contains non-diagonal terms in order to take into account tunneling processes between the two superconductors. We can calculate the supercurrent flowing inside the junction by solving Eq. (1.81), in the limit of weak coupling between the two metals [45]:

$$I_s = I_c \sin(\phi) \tag{1.82}$$

where $\phi = \phi_1 - \phi_2$ is the relative phase difference between the order parameters associated with each superconductor, while I_c is the critical current of the device.

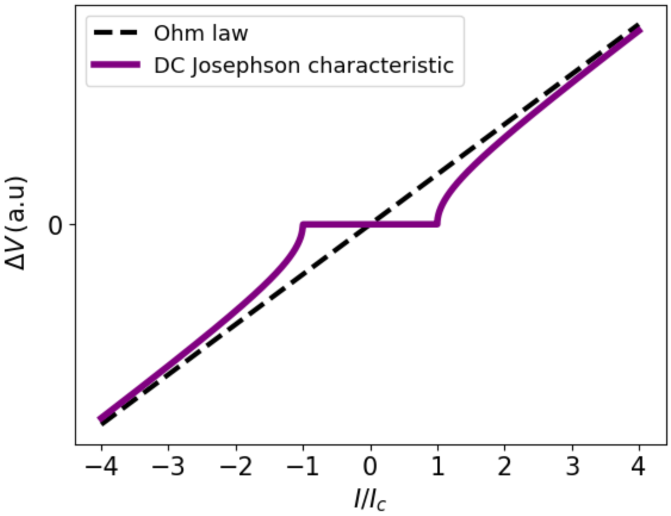

Figure 1.9: *$I - \Delta V$ characteristic describing a superconducting Josephson junction (purple line), in the absence of an external potential difference ΔV (DC regime), plotted together with Ohm's law $\Delta V = IR$ (black dashed line). We notice that the ohmic behavior is retrieved when we inject a current higher than the critical current I_C, and a finite ΔV starts to develop. The Josephson junction characteristic is obtained by plotting the stationary solution of the RSJ model, reported in Eq. (1.94), such that we chose the same G (or equivalently R) for both plots.*

The latter quantity represents the maximum value of the current which can be injected inside the system and flow without dissipation; we notice that Eq. (1.82) predicts a supercurrent I_s that follows a sinusoidal law of the phase difference ϕ. From Eq. (1.81) we can also calculate the time evolution of the phase difference:

$$\dot{\phi} = \frac{q\,\Delta V}{\hbar} \tag{1.83}$$

where $q = 2e$ is the charge of a *Cooper pair*, while ΔV is the applied potential difference across the junction. Eqs. (1.82) and (1.83) are known as the Josephson-Anderson equations, and identify two distinct transport regimes.

1. The *DC Josephson effect* where $\Delta V = 0$, and a constant dissipationless supercurrent $I_s < I_c$ can flow inside the junction without developing any additional potential difference. If the injected current overcomes the critical current I_c the junction starts to manifest a resistive behavior and a finite potential difference ΔV develops, as shown in Fig. 1.9.

2. The *AC Josephson effect*, in which $\Delta V \neq 0$, where an alternate current having a frequency of $2e/\hbar$ flows inside the junction, while the relative phase linearly increases with time.

We want to clarify that, while the phase evolution reported in Eq. (1.83) is derived from Eq. (1.81) without approximations, Eq. (1.82) for the supercurrent was found by imposing a weak coupling constraint, and in general the current-phase relation can be different from the predicted sinusoidal law [46]. The dependancy of the supercurrent from the superconducting gap Δ and the temperature T is given by the *Ambegaokar-Baratoff* relation [47]:

$$I_c R_n = \frac{\pi\Delta}{2e} \tanh\left(\frac{\Delta}{2k_B T}\right) \tag{1.84}$$

where R_n is the resistance of the non superconducting metal that constitutes the barrier. When $T = 0$, Eq. (1.84) reduces to $I_c R_n = \pi\Delta(0)/2e$, meaning that the zero temperature critical current is directly proportional to the superconductors order parameter. Therefore, Josephson effect provides a powerful probe of the order parameter of superconductors, as long as a measurement of the critical current can be performed.

1.6.2 Josephson effect in superfluids

As shown in Sec. 1.5 the superfluid state is associated with a macroscopic wave function, as shown in Eq. (1.74), which is of the same form of the superconducting order parameter reported in Eq. (1.78). This implies that a system made up of two superfluid reservoirs separated by a thin insulating barrier, where the respective wave functions overlap, should undergo the Josephson dynamics expected in superconductors. Regardless of the nature of the system, be it bosonic or fermionic, the problem can be described in terms of the two-state model. Let us consider a weakly interacting Bose-gas, bisected into two distinct reservoirs, where we solve Eq. (1.51) in order to find indipendently the corresponding wave functions $\Psi_{1,2}$, both being associated with an atom number $N_{1,2}$ and a global phase $\phi_{1,2}$. In the intermediate Josephson regime, where $N^2 >> E_J/E_C \sim 1$, the effective Hamiltonian describing the system can be written as [32]:

$$H_J = E_C \frac{k^2}{2} - E_J\, cos(\phi) \tag{1.85}$$

where E_C is the charging energy of the junction, E_J the Josephson tunneling energy, ϕ is the phase difference $\phi_1 - \phi_2$ and k is the popolation imbalance $k = (N_1 - N_2)/2$. We can write down the equations of motion from the Hamiltonian reported in Eq. (1.85), where the canonical conjugate variables are ϕ and $\hbar k$:

$$\begin{cases} \dot{\phi} = \dfrac{\partial \phi}{\partial t} = \dfrac{\partial H_J}{\partial(\hbar k)} = k\dfrac{E_C}{\hbar} \\ \\ \hbar\dot{k} = \dfrac{\partial(\hbar k)}{\partial t} = -\dfrac{\partial H_J}{\partial \phi} = -E_J\, sin(\phi) \end{cases} \tag{1.86}$$

When $\phi << 1$, the solution of the coupled Hamilton Eqs. (1.86) is given by periodic oscillations of both ϕ and k, one out of phase of $\pi/2$ with respect to the other, and occurring at the following plasma frequency ω_J:

$$\omega_J = \frac{1}{\hbar}\sqrt{E_C E_J} \tag{1.87}$$

With opportune algebraic manipulations, Eqs. (1.86) can be written in the same form of Eqs. (1.82) and (1.83); in fact, if we divide the second equation by $\hbar$, we obtain a similar expression to Eq. (1.86) [32]:

$$I = I_c \sin(\phi) \tag{1.88}$$

where $I = -\dot{k}$ is the particle current, which represents the flow of non-charged atoms across the insulating barrier, while the junction's critical current I_c can be written in terms of the Josephson tunneling energy E_J, such that $I_c = E_J/\hbar$. The charging energy E_C can be expressed in terms of the chemical potentials $\mu_{1,2}$, each associated with one distinct reservoir, as [32]:

$$E_C = \frac{\partial \mu_1}{\partial N_1} + \frac{\partial \mu_2}{\partial N_2} = -\frac{2\Delta\mu}{\Delta N} = -\frac{\Delta\mu}{k} \tag{1.89}$$

where $\Delta\mu = \mu_1 - \mu_2$ is the chemical potential difference. The first Eq. (1.86) then becomes:

$$\hbar\dot{\phi} = -\Delta\mu \tag{1.90}$$

analogous to Eq. (1.83), where, for neutral atoms, the chemical potential difference plays the role of the voltage drop in superconducting junctions. Eqs. (1.88) and (1.90), representing the superfluid analogous of the *Josephson-Anderson* equations introduced for superconductors, have been formally derived by resolving the *Gross-Pitaevskij* equation for a weakly-interacting bosonic gas, but they also hold for superfluids across the whole BEC-BCS crossover. The main difference between Bose gases and crossover Fermi gases is that, in the latter case, under the critical temperature the condensate is made up of atom pairs regardless of the position in the crossover. This means that the particle current for fermionic superfluids in the BEC-BCS crossover is a pair current I_B, such that $I_B = I/2$, where I is the current associated with the tunneling of single atoms, while the pair chemical potential is $\mu_B = 2\mu$. We want to stress out that, despite their remarkable similarities, superfluid Josephson junctions are interested by unique physical phenomena with respect to superconducting junctions. One such phenomena is constituted by *macroscopic quantum self-trapping* (MQST): two Bose–Einstein condensates, weakly linked by a thin optical barrier, end up with a higher average number of bosons on one side of the junction than the other even in the presence of tunneling phenomena, which tend to re-equilibrate the density imbalance.

1.6.3 Circuital models

Real superconducting Josephson junctions can be described in the context of electronic circuits, where dissipation phenomena, finite-size effect and charge accumulation can be taken into account by introducing opportune circuit elements. This method can be also extended to atomic Josephson junctions, as done for example in Refs. [19] and [48], where resistive dynamics occurring during the tunneling process is characterized through a conductance G. In the following we will briefly introduce the main circuital models used for describing real junctions, namely the RSJ and the RCSJ models: in this framework, the physical system behaves in a similar way to a damped harmonic oscillator, its dynamics being described by the *tilted washboard potential* $U(\phi)$. In the particular case of a Josephson junction, this potential determines the dynamics of the relative phase ϕ, depending on the value of the injected current.

RSJ Model

In order to incorporate dissipative dynamics into the system we consider the *resistively shunted Josephson junction* (RSJ) model, where a Josephson junction is put in parallel with a resistance R, as shown in Fig 1.10: in this setup, the latter element acts as a shunt.

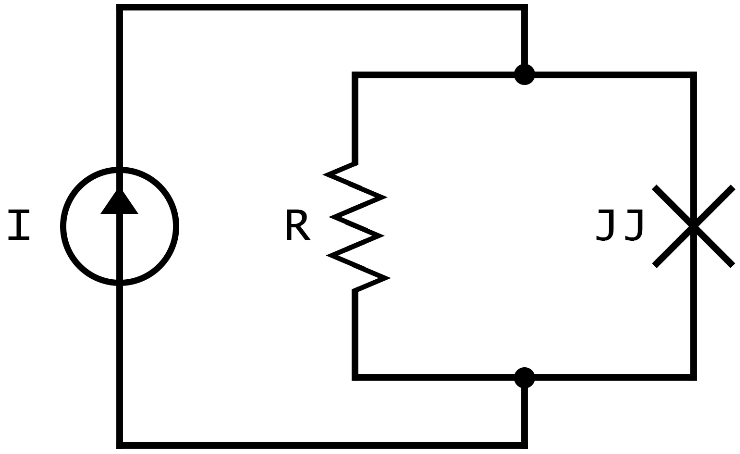

Figure 1.10: *The resistively shunted Josephson junction (RSJ) model circuit.*

The total current I provided by the external source is split in the two branches of the circuit, according to Kirchhoffs's law of currents:

$$I = \frac{\Delta V}{R} + I_c \sin(\phi) \tag{1.91}$$

where ΔV is the potential difference between the sides of the junction (or, equivalently, of the resistance), while the second term represents the current-phase relation typical of Josephson junctions, reported in Eq. (1.82). For atomic Josephson junctions, where the chemical potential difference $\Delta\mu$ replaces the potential drop ΔV, we can write Eq. (1.91) in the following form:

$$I = -G\,\Delta\mu + I_c\,\sin\left(\phi\right) \tag{1.92}$$

where $G = R^{-1}$ is the junction's conductance. By substituting Eq. (1.90) into Eq. (1.92) we obtain the following first-order differential equation for the relative phase $\phi(t)$, describing the RSJ model:

$$I = G\,\hbar\frac{\partial\phi}{\partial t} + I_c\,\sin\left(\phi\right) \tag{1.93}$$

In the following we will assume that the externally provided current I is constant, and not modulated in time (i.e. a direct current); above the critical current, where $I > I_c$, the $\Delta\mu - I$ characteristic of the junction is calculated by integrating Eq. (1.92) and taking the time average of Eq. (1.90):

$$\langle\Delta\mu\rangle = G^{-1}\sqrt{I^2 - I_c^2} \tag{1.94}$$

where $\langle\Delta\mu\rangle$ is the time-averaged chemical potential difference, which builds up due to the application of the atomic current I.

RCSJ Model

Another property of real Josephson junctions is the possibility for the charged particles to accumulate at the interface layers of the device, behaving in a similar way to a capacitance placed inside an electronic circuit. This phenomena causes the presence of an additional contribution to the total current I flowing inside the system: in the framework of circuital models, the process is described by adding a capacitance C in parallel to the RSJ circuit discussed before, as shown in Fig. 1.11.

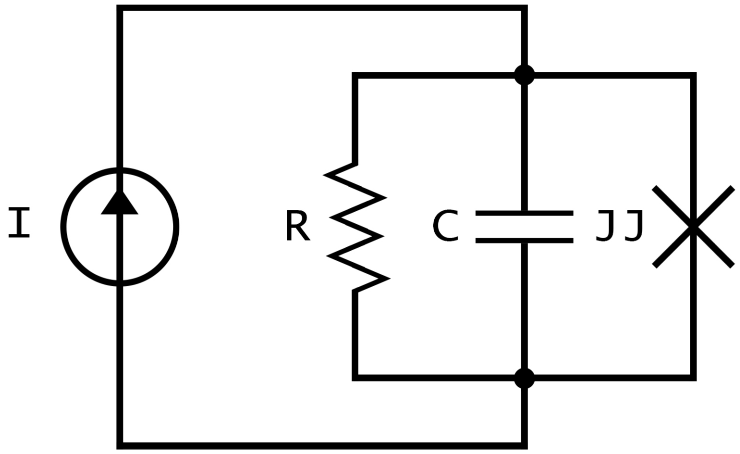

Figure 1.11: *The resistively and capacitively shunted Josephson junction (RCSJ) circuital model.*

The circuital model just introduced goes under the name of *resistively and capacitively shunted Josephson junction* (RCSJ) model, and in this case Eq. (1.91), reporting the Kirchhoff's law for currents, is modified to:

$$I = \frac{\Delta V}{R} + C\,\frac{\partial V}{\partial t} + I_c\,\sin{(\phi)} \tag{1.95}$$

where the injected current I is still assumed to be constant in time. The first two terms in Eq. (1.95) represent the current flowing inside the resistance and the one flowing within the capacitance respectively, while the last term represents the sinusoidal current-phase relation describing Josephson junctions, reported in Eq. (1.82) . For the superfluid Josephson junction, where the potential drop is replaced by the chemical potential difference ($\Delta V \to -\Delta\mu$) while the time evolution of the relative phase ϕ is given by Eq. (1.90), we can recast Eq. (1.95) in the form:

$$\tilde{C}\frac{\partial^2\phi}{\partial t^2} = I - I_c\,\sin{(\phi)} - \tilde{G}\frac{\partial\phi}{\partial t} \tag{1.96}$$

where we defined the quantities $\tilde{C} = \hbar C$ and $\tilde{G} = \hbar G$. In the atomic case, the capacitance C introduced in Eq. (1.95) is related to the reciprocal of the charging energy E_C defined in Eq. (1.89), such that $C = E_C^{-1}$. Eq. (1.96) represents the circuital analogue of the damped classical pendulum (i.e. a mechanical system), which is described by the following equation of motion:

$$m\frac{d^2x(t)}{dt^2} = F_c - \beta\frac{dx(t)}{dt} \tag{1.97}$$

so that $\tilde{C}$ plays the role of the particle's mass m, $\tilde{G}$ can be identified with a damping coefficient β, while $F_c = I - I_c\,\sin{(\phi)}$ represents a conservative force. In this mechanical context ϕ can be regarded as the position of the particle, while $\dot{\phi}$ and $\ddot{\phi}$ represent its velocity and acceleration respectively. The conservative force F_c admits the following potential, such that $F_c = -dU(\phi)/d\phi$:

$$U(\phi) = -\int\Big(I - I_c\,\sin{(\phi)}\Big)d\phi = -I\phi - I_c\,\cos{(\phi)} \tag{1.98}$$

which is called *tilted washboard potential*, and allows to study the dynamics of the relative phase ϕ as a function of the injected current. In fact, when applying an external current I, constant over time, we can distinguish between two different behaviors for the dynamical evolution of the phase:

1. When $I < I_c$ the particle is trapped in a minimum with constant relative phase, such that $\dot{\phi} = 0$, where no spontaneous $\Delta\mu$ develops. This situation corresponds to the non-resistive branch in the $\Delta\mu - I$ characteristic associated with the DC Josephson effect.

2. When $I > I_c$ the particle rolls down the potential curve $U(\phi)$ rapidly, with almost linearly increasing phase, entering the regime of running phase where $\dot{\phi} \neq 0$: as a consequence, in this regime, a non-zero $\Delta\mu$ is generated. This phenomena represents the resistive branch of the DC Josephson effect, where dissipative effects set in for external currents I higher than the junction's critical current I_c. Both of these regimes are shown in Fig 1.12, which reports the *tilted washboard potential* $U(\phi)$ as a function of ϕ for different I/I_c ratios.

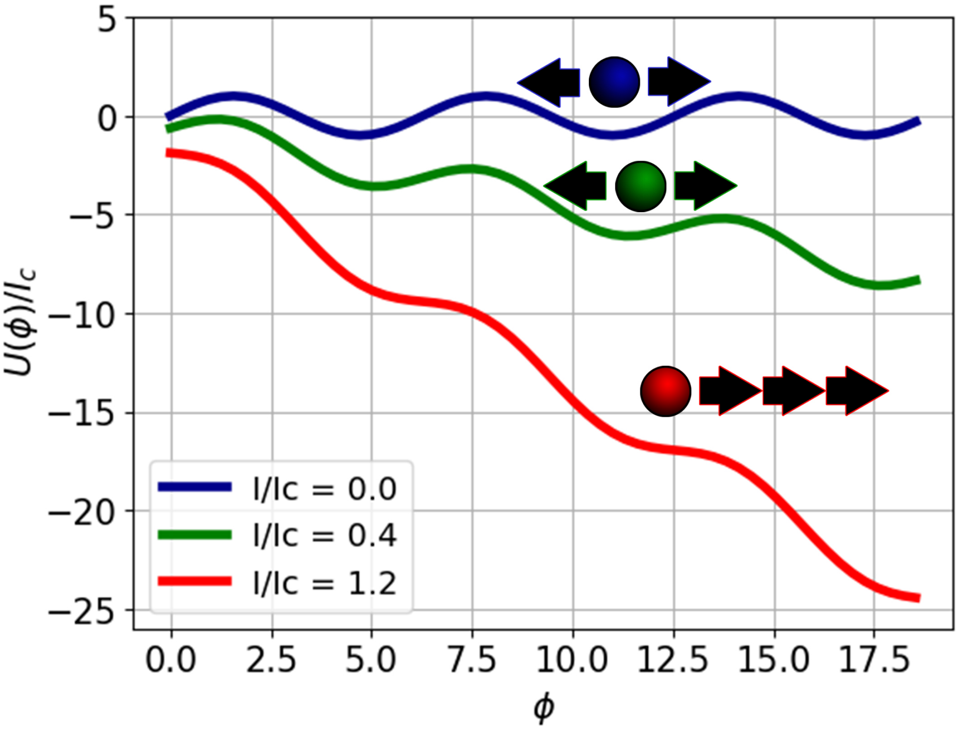

Figure 1.12: *Tilted washboard potential as a function of the relative phase for different values of the injected current I, normalized by the critical current I_c. For low enough values of the applied current I, the phase is trapped in a local minima of the potential, and no ΔV develops. When $I > I_c$, the phase can roll down the potential curve with increasing phase, resulting in a finite phase velocity $\partial\phi/\partial t$: this leads to a dissipative behavior, where a potential drop develops at the sides of the junction.*

The precise dynamics of the system depends on the ratio between the parameters $\tilde{G}$ and $\tilde{C}$, which represent damping and inertia respectively. When $\tilde{C} \gg \tilde{G}$, the mass is so big that the particle's inertia is almost unaffected by damping phenomena, while, on the other hand, if the damping term dominates ($\tilde{C} \ll \tilde{G}$) we expect the chemical potential difference $\Delta\mu$ to reach a smaller value with respect to the former case. In order to study this behavior is useful to introduce the *Steward-McCumber* parameter β_c:

$$\beta_c = \frac{I_c C}{\hbar G^2} \tag{1.99}$$

such that Eq. (1.97), which describes the motion of the particle, becomes, when dividing each side by the critical current I_c:

$$\frac{1}{\omega_j^2}\ddot{\phi} = \frac{I}{I_c} - sin(\phi) - \frac{1}{\omega_j}\frac{1}{\sqrt{\beta_c}}\dot{\phi} \tag{1.100}$$

where ω_j is the plasma frequency introduced in Eq. (1.87), which can be rewritten as:

$$\omega_j = \sqrt{\frac{I_c}{\hbar C}} \tag{1.101}$$

where we used the relation $E_C = C^{-1}$, together with $E_J = \hbar I_c$. In atomic Josephson junctions the charging energy E_C can be calculated as follows:

$$E_C = \frac{\partial \mu_L}{\partial N_L} + \frac{\partial \mu_R}{\partial N_R} \approx 2\,\frac{\partial \mu_L}{\partial N_L} = \frac{8}{3}\frac{\mu}{N} \tag{1.102}$$

where the second passage holds true only if the system presents a small chemical potential imbalance $\Delta\mu = \mu_L - \mu_R$ between the left and the right reservoir, while the number of atoms is approximately the same in both of them, $N_L \approx N_R$. Depending on the value of the parameter β_c, different situations can arise:

1. Overdamped regime, where $\beta_c \ll 1$, and friction dominates over the particle's inertia. The time averaged chemical potential difference $\langle\Delta\mu\rangle$ is the same of Eq. (1.94).

2. Underdamped regime, where $\beta_c \gg 1$, and the particle mass, represented by the capacitance C, is so big that the damping hardly affects the dynamics. This regime can show hysteresis, such that if we modulate the external current I from $I > I_c$ to $I < I_c$ the relative phase ϕ is not necessarily trapped in a local minima of the *tilted washboard potential*, but can continue to roll down the potential curve.

Phase dynamics in terms of the tilted washboard potential explains the behavior of the $\Delta\mu - I$ curves observed in the DC Josephson effect, where a direct current $I = const$ is applied to the junction, but can also describe more exotic phenomena; a noteworthy example is represented by the response of the system to an applied alternating current $I(t)$, modulated in time.

1.6.4 Shapiro steps in Josephson junctions

In Sec. 1.6.1 we described the Josephson effect, arising when two superconductors are separated by a thin insulating layer that allows for tunneling processes: below a critical value I_c, the injection of a direct current $I = const$ causes a dissipationless supercurrent to flow inside the junction (DC effect), while the application of a finite potential difference ΔV generates within the junction an alternating current (AC effect), which frequency of oscillation depends on the applied potential drop. The injection of a modulated current, periodic in time, causes the emergence of a new phenomenon linked to the Josephson dynamic: in the $\Delta V - I$ characteristic, the potential drop at the sides of the junction jumps almost discontinuously for certain amplitude values of the applied current. This peculiar structure is known as **Shapiro steps**, and represents the main subject investigated in the present thesis. These voltage jumps occurs, for superconducting Josephson junctions, at an average height of $\langle\Delta V\rangle_t = n\hbar\omega/2e$, where ω is the modulation frequency of the applied current (or, equivalently, of an external radio frequency), t is the time in which the current is injected, while n is an integer: an example of the typical $\Delta V - I$ curve which develops when applying a radio frequency to the system is reported in Fig. 1.13.

The behavior of a Josephson junction, current-biased through an alternating current $I(t)$, can be explained by means of the tilted washboard potential introduced in Sec. 1.6.3, in the context of the RCSJ circuital model. When a

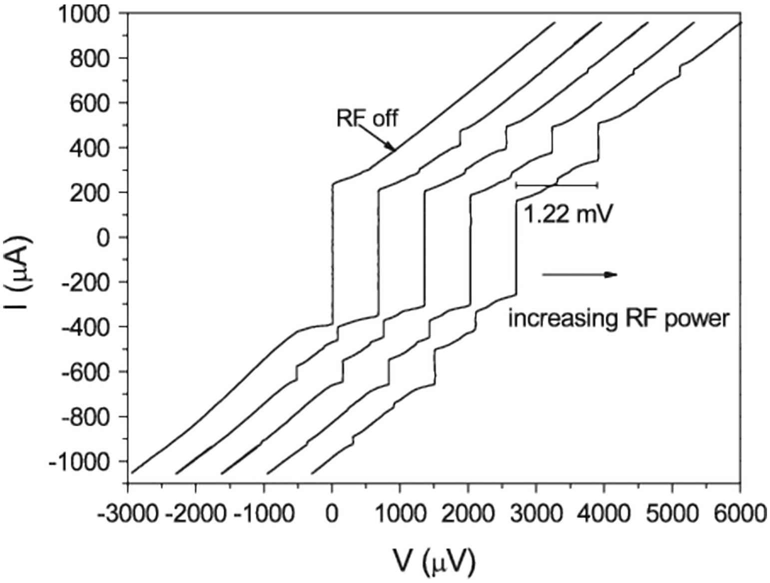

Figure 1.13: *Shapiro steps on the $I - \Delta V$ curves, induced by a radiation of* $0.6\,THz$. *The graphs for different radio frequency powers are shifted horizontally for clarity: the increment being* $3\,dB$ *each time. When the radio frequency is off, we retrieve the $I - \Delta V$ characteristic typical of the DC Josephson effect, shown in Fig. 1.9. Figure taken from Ref. [49].*

modulated current $I(t)$ is injected inside the system, Eq. (1.96), which describes the total current flowing within an ultracold Josephson junction, takes the following form:

$$I(t) = I_c \sin\phi + \hbar G\dot{\phi} + \hbar C\ddot{\phi} \tag{1.103}$$

such that the tilted washboard potential of Eq. (1.98) becomes:

$$U(\phi) = -I(t)\phi - I_c \cos(\phi) \tag{1.104}$$

In this discussion, the applied current $I(t)$ is supposed to be made up by a combination of a direct current I_{DC} and an alternating current I_{AC}:

$$I(t) = I_{DC} + I_{AC}\cos(\omega t) \tag{1.105}$$

where ω is the (angular) frequency of modulation. If we set $I_{AC} = 0$, the system experiences only the direct current I_{DC}, and the behavior of the relative phase ϕ is the same described in Sec. 1.6.3: for $I_{DC} < I_c$ the phase is located in one of the potential's local minima, and a dissipationless supercurrent flows inside the Josephson junction, while for $I_{DC} > I_c$ the washboard potential turns into a monotonous decreasing function of ϕ, such that the phase is no longer trapped within a minima, and is free to roll down the potential curve with increasing velocity $\partial\phi/\partial t$. When the applied current features an alternate component I_{AC} a new dynamic emerges, as the tilt of the washboard potential reported in Eq. (1.104) changes during time. The relative phase ϕ can undergo different processes during each modulation period: for sufficiently low driving ($I_{AC} \ll I_c$, with $I_{DC} < I_c$), the phase undergo small oscillations around a local minima of the washboard potential and it is consequently trapped, while for strong driving modulations or large enough direct currents ($I_{DC} + I_{AC} \sim I_c$) the phase acquires a sufficient speed $\partial\phi/\partial t$ to be able to escape from this minima. The oscillations of the current cause the phase to be trapped in the next local minima, as shown in Fig. 1.14: this dynamics may repeat many times during the driving time of the current.

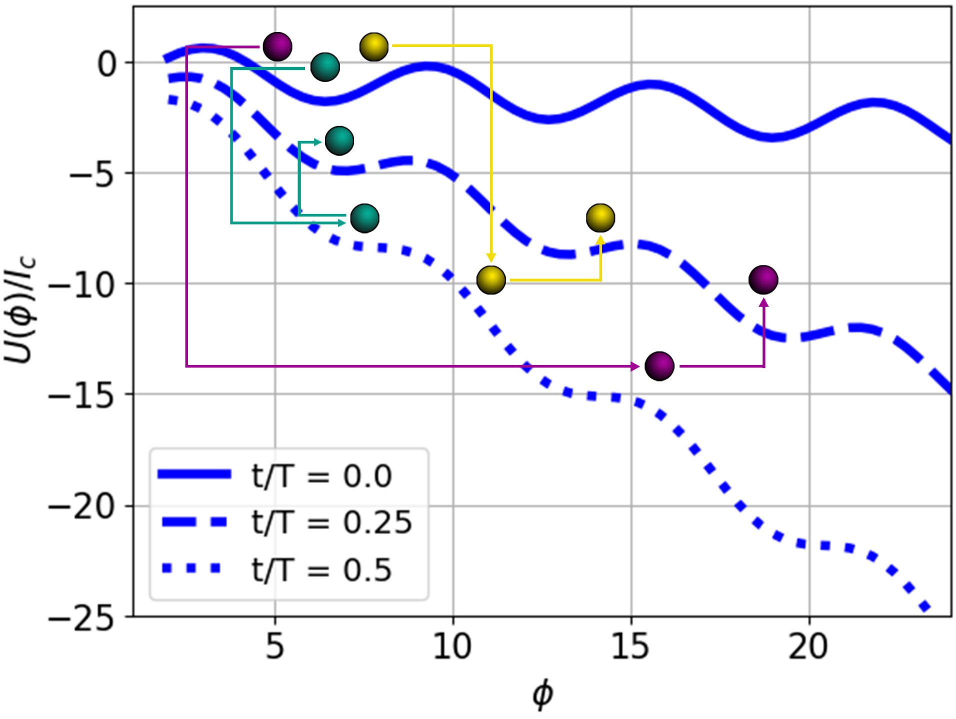

Figure 1.14: *Tilted washboard potential $U(\phi)$ as a function of the relative phase ϕ, shown at different times with a frequency of modulation of $\omega = 2\pi \cdot 175$ Hz, normalized by I_c. The tilt of the washboard potential changes during time due to the external modulation, influencing the dynamics of the phase and eventually giving rise to Shapiro steps.*

This process happens only when the phase velocity is resonant with the angular frequency of the modulation, such that its average during the driving time t_d reads:

$$\langle\dot{\phi}\rangle_{t_d} = n\omega \tag{1.106}$$

where n is an integer which corresponds to the number of times the relative phase has jumped across adjacent local minima during the modulation period. By exploiting Eq. (1.90) the time-average of the chemical potential difference $\langle\Delta\mu\rangle$ can be calculated:

$$\langle\Delta\mu\rangle_{t_d} = \hbar\langle\dot{\phi}\rangle_{t_d} = \hbar n\omega \tag{1.107}$$

such that, as a consequence of the phase dynamics due to the external modulation, a finite chemical potential difference $\Delta\mu$ develops. When the alternate current component I_{AC} is not strong enough to cause the aforementioned dynamics, oscillations of the phase trapped within a minima of the washboard potential still induce density modulations on both reservoirs: in this case, the chemical potential difference averages to zero during the driving time t_d, $\langle \Delta\mu \rangle_{t_d} = 0$.

Chapter 2

Experimental setup and ultracold Josephson junction

In order to probe the transport properties inside an atomic Josephson junction, it is first necessary to obtain an ultracold gas, cooling down the system below the degeneration temperature T_{deg} introduced in Sec. (1.2), under which the wave functions of contiguous atoms overlap and quantum effects become important. Moreover, it is also necessary to entrap the created ultracold gas within a certain region of the space; an atomic Josephson junction consists of two independent superfluid reservoirs, isolated from the external environment and separated by an insulating barrier, thin enough to allow tunneling phenomena. A low temperature gas can be experimentally obtained through laser cooling techniques, which exploit photon-electron interactions in order to modify the state of motion of the atoms. Subsequent evaporative cooling processes allow to obtain an ultracold degenerate gas in the superfluid state, and additional experimental techniques such as laser trapping can be employed to further slow down the atomic cloud and to confine it in the desired region of space. An atomic Josephson junction can be realized by trapping the ultracold cloud inside optical potentials; in particular, in this thesis work a digital micro-mirror device (DMD) permits to create a rectangular hybrid potential (see Sec. 2.1 and Sec. 2.3), presenting a thin Josephson barrier which splits the superfluid into two distinct regions. In Sec. 2.1 we will describe the geometry of the experimental setup and how it allows to realize an ultracold fermionic gas of ^{6}Li, through the employment of several laser cooling and laser trapping techniques. We will briefly discuss about the absorption imaging setup as well, which permits to measure the cloud's particle density $n(\vec{r})$: from this quantity, other important thermodynamic quantities can be extracted, as the chemical potential μ, the *Fermi energy* E_F or the atom number N. The working principle of the DMD is reported in Sec. 2.2; this device is employed for projecting the final repulsive optical trap that allows for the realization of a rectangular atomic Josephson Junction. In Sec. 2.3 we deal with the problem of interacting ultracold Fermi gases (see Sec. 1.3) along the BEC-BCS crossover introduced in Sec. 1.4, in the particular case of trapping due to a hybrid optical dipole potential with rectangular shape, achievable with the DMD: we will calculate the main physical properties of the trapped gas, namely the chemical potential μ, the Fermi energy E_F and the speed of sound c_s. Finally, in Sec. 2.4 we will discuss about the preliminary calibration procedure which permits to to estimate the depth of the potential barrier V_0, whose ratio to the chemical potential μ determines whether or not we are in the tunneling regime ($V_0/\mu > 1$), where the supercurrent flowing inside the Josephson junction is caused by quantum tunneling phenomena.

2.1 Experimental setup

In this section we will describe how ultracold ^{6}Li gas is made and manipulated in our experimental setup, in terms of laser cooling and trapping techniques. The starting point is an artificially enriched lithium bar, which is heated inside an oven to a temperature of 420° C in order to create an atomic beam, subsequently collimated by a copper cold finger. Before being sent to the science chamber, a custom-made octagonal stainless-steel cell kept under a pressure below 10^{10} mBar, the high temperature atomic beam is preliminary cooled by a Zeeman slower down to a speed of about $60\,m/s$. The main cooling/trapping processes, such as the magneto-optical trap and forced evaporation, will take place inside the science chamber structure. A detailed presentation about these processes is reported in App. A.2, together with the nature of the radiative forces (App. A.1) acting on the atomic system, and how they can be exploited to realize the various laser manipulation mechanisms. The experiment must be carried out under vacuum in order to isolate it from thermal background particles, which would limit the life time of the sample: our setup consists of an Ultra-High-Vacuum (UHV) system in order to overcome this problem. To manipulate ^{6}Li atoms resonant light is employed for slowing, cooling and imaging the sample, while confinement into optical dipole traps is achieved with off-resonant lights. In order to introduce the experimental apparatus it is therefore necessary to first discuss the energy levels of ^{6}Li and their possible transitions.

Fine and Hyperfine structure of ^{6}Li lower levels

Transitions between an atom's ground-state and its excited levels are employed in a wide variety of experimental techniques; for alkali atoms, like ^{6}Li, these transitions allow for the realization of laser cooling and laser trapping. A level scheme, not in scale, reporting the main transitions between the ^2S state and the ^2P states is shown in Fig. 2.1. The lines D_1 and D_2 represent the fine structure doublet, addressing the transition between the ground state $2^2S_{1/2}$, with $l = 0$, and the excited states $2^2P_{1/2}$ and $2^2P_{3/2}$, both with $l = 1$ but different total angular momentum $J = L \oplus S$. The wavelength associated with both of these transitions is almost 671 nm, and we employ two Toptica TA-Pro lasers, both amplified by a MOPA amplifier, to work around such wavelength. The lasers are locked to the corresponding frequency by means of a saturation spectroscopy apparatus. Transitions involving these hyperfine and excited levels are employed both in the MOT and in the optical molasses, which act on the atoms before the start of the evaporative cooling process, as explained in the following.

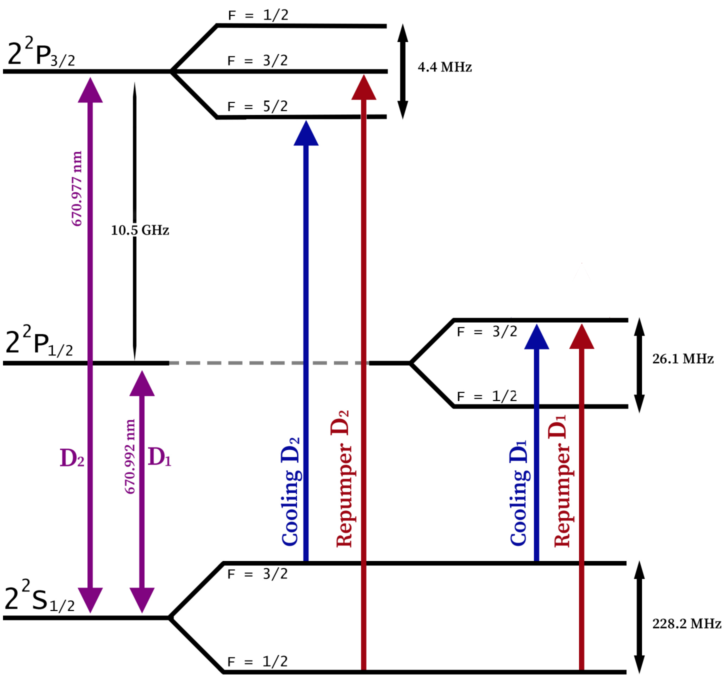

Figure 2.1: *Energy levels of* ^6Li*, in the absence of an applied magnetic field, showing the hyperfine structures of both the ground state* $^2S_{1/2}$ *and the excited levels* $^2P_{1/2}$ *and* $^2P_{3/2}$*.*

2.1.1 Ultracold gas realization

Here we report a brief summary of the experimental process followed to obtain the ultracold ^{6}Li gas investigated in our measurements: further information can be found in Refs. [50] and [51]. In the Zeeman slower, the atoms coming from the oven are cooled down from an initial average speed of $800\,m/s$ to a final value of about $60\,m/s$, thanks to the combined application of:

1. A counter-propagating laser wave with respect to the atomic beam, oscillating in resonance with the D_2 transition.
2. A non-uniform magnetic field $B(x)$ generated by a set of coils, which keeps the light in resonance with the atomic transition by exploiting the Zeeman shift of the hyperfine levels. This procedure is explained in details in App. A.2.

The atoms, slowed down, are directed towards the science chamber, where they are trapped and further cooled down by a magneto-optical trap composed of three retroreflected laser beams, acting on the D_2 transition and propagating along the x, y and z directions, while a quadrupolar magnetic field is produced by a pair of coils in anti-Helmotz configuration [52]. In the magneto-optical trap, approximately 10^9 atoms are loaded and reach a temperature of about $500\,\mu$K: the magnetic field and the lights of the MOT are subsequently switched off, and the system is further cooled down to a temperature of order of $50\,\mu$K thanks to an optical molasses acting on the D_1

transition, operating a sub-Doppler cooling procedure. A circuit of acusto-optic modulators is employed to modulate the frequency of re-pumping and cooling lights, which address the transitions of the ground state hyperfine levels during the MOT (D_2) and in the optical molasses (D_1); these transitions are shown in Fig. 2.1. The necessity of using a re-pumping light is to avoid atom losses, which happen for the following reason: the cooling light induces a transition between the ground-state level $2^2S_{1/2}$ with $F = 3/2$ and the excited level $2^2P_{3/2}$ with $F = 5/2$, but due to spontaneous emission processes the atom can subsequently de-excite with a small probability in the hyperfine ground-state $F = 1/2$, which is out of resonance with the cooling transition and behaves as a dark state. Since the MOT is realized with about 10^5 cycles of absorption/emission processes, during its loading a macroscopic number of atoms ends up in the $F = 1/2$ dark state; in order to overcome this problem another light re-pumps back these atoms in the desired $F = 3/2$ hyperfine ground state. After this cooling chain an evaporative cooling process is started in an optical dipole trap, created with the high intensity IPG laser, oscillating at a wavelength of 1073 nm with an initial power of about 130 W, in order to achieve the condition of quantum degeneracy: this laser beam is successively crossed with the 50 W Mephisto one ($\lambda = 1064\,\mathrm{nm}$), creating a cigar-shaped optical trap where the atomic sample completes the evaporation, giving approximately 10^5 atoms per spin state, at a temperature in the range of $50 - 100\,\mathrm{nK}$. Since we work with high magnetic fields ($B > 600\,\mathrm{G}$), the Zeeman effect causes an additional split of the hyperfine energy levels reported in Fig 2.1, separating states that correspond to a different angular momentum projection m_F along the quantization axis: our system is initially in a balanced mixture of the states $|1\rangle$ and $|2\rangle$, shown in Fig. 2.2, which are distinguishable and allow for low-energy collisions, such that forced evaporation is possible.
At the beginning of the evaporative cooling process, a radio frequency modulated over time is applied to the atomic cloud, forcing an adiabatic transition from the Zeeman sublevel $|2\rangle$ to sublevel $|3\rangle$. This procedure is justified for two main reasons:

1. The Feshbach resonance of the scattering channel $|1\rangle - |3\rangle$ occurs at a smaller magnetic field ($696\,G$) with respect of the resonance associated with channel $|1\rangle - |2\rangle$ ($832\,G$), as shown in Fig. (2.3). Smaller magnetic fields are easier and less cumbersome to realise in experiments, since they require flows of lower currents inside the coils.

2. In the $|1\rangle - |3\rangle$ scattering channel the resonance is more narrow, as again shown in in Figure (2.3), allowing for fast sweeps in the BEC-BCS crossover. In this condition we can observe quantized vortices, which nucleate in the unitary regime: in particular, we employ a technique where we quickly move from the unitary regime into the BEC regime, where vortices are detectable since they manifest as a singularity in the cloud's density profile only in this regime.

The net result of this process chain is the creation of an ultracold ^{6}Li fermionic gas in a balanced mixture of Zeeman substates $|1\rangle$ and $|3\rangle$, trapped in an attracting cigar-shaped optical dipole trap at the end of the evaporative cooling process. The optical setup and the various laser lights employed for realizing the ultracold gas is shown in Fig. 2.4.

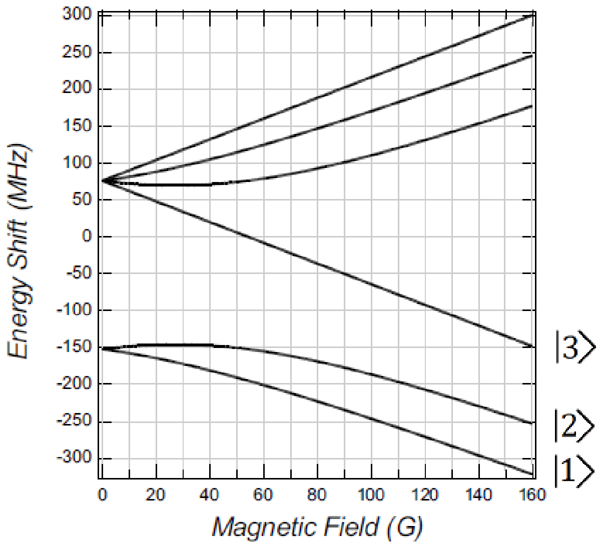

Figure 2.2: *Magnetic field dependence of the* $2^2S_{1/2}$ *ground state of* ^{6}*Li. States* $|1\rangle$ *and* $|2\rangle$ *correspond to the Zeeman sublevels of the hyperfine state* $F = 1/2$*, while* $|3\rangle$ *is the lowest Zeeman sublevel of the hyperfine state* $F = 3/2$*. For high magnetic fields states* $|2\rangle$ *and* $|3\rangle$ *are separated by an energy of about* $100\,MHz$*. Figure taken from Ref. [53].*

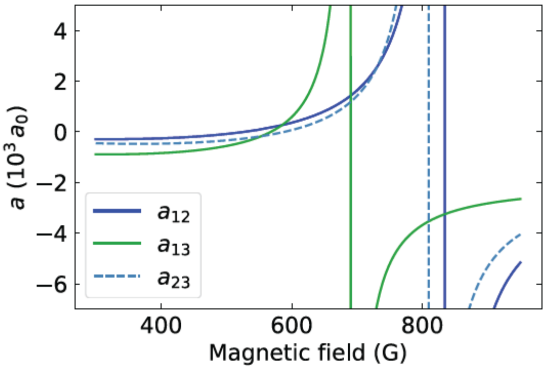

Figure 2.3: *Feshbach resonances of the three lowest* ^{6}*Li hyperfine states. Figure taken from Ref. [54].*

Eventual applications of external magnetic fields allow for the exploration of the BEC-BCS crossover, resulting in the creation of fermionic superfluids of different nature: in this thesis we will mainly study the BEC regime of weakly repulsive interacting fermions ($1/k_F\, a \gg 1$), obtainable with the application of a magnetic field of about $630\,G$. This ultracold gas can be further trapped in a repulsive potential of arbitrary shape, produced by a digital-micromirror device (DMD), which allows for the realization of an atomic Josephson junction having the desired geometry; in order to do so, it is first necessary to switch off the IPG and Mephisto lasers, at the end of the evaporation ramp. The condensate is simultaneously loaded onto an optical dipole trap, realized through another dedicated optical circuit, which employs a green 532 nm laser

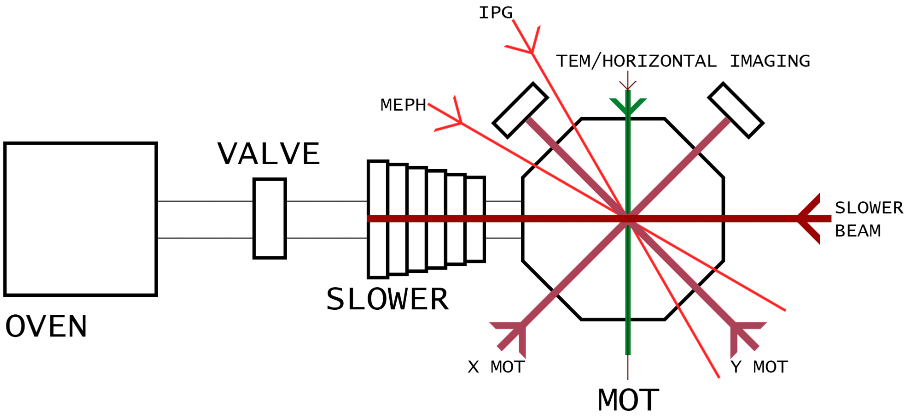

Figure 2.4: *Scheme of the experiment section reporting the cooling setup and the employed laser beams.*

described by the $\mathrm{TEM}_{0,1}$ Hermite-Gauss mode; this will ensure vertical trapping of the sample, which occurs at a trap frequency of about $w_z \sim 2\pi \cdot 420\,\mathrm{Hz}$. At the same time the DMD is also turned on, and the reflection of the 532 nm laser is projected onto the atoms, creating a repulsive confinement of arbitrary shape on the x-y plane, while on the vertical direction the harmonic confinement due to the green laser keeps the atoms from escaping the trap. An example of the Josephson junction which can be realised with the repulsive potential of the DMD is reported in Fig. 2.5, where the particular case of a rectangular potential, with a thin barrier in its centre, is shined onto the atomic cloud:

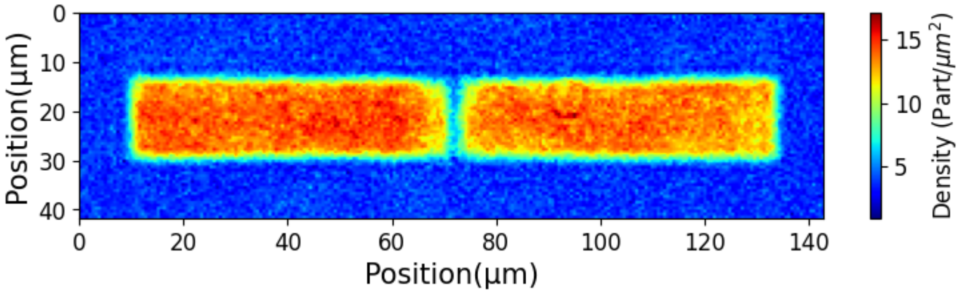

Figure 2.5: *Rectangular Josephson junction with a thin barrier in its centre, created by the DMD potential.*

In Sec. 2.2 we will describe the precise functioning of the digital micro-mirror device, and how it allows to create dynamic potentials of arbitrary shape.

2.1.2 Imaging setup

After the creation of the crossover superfluid, trapped within the DMD potential, we need to extract informations about the atomic cloud; in ultracold atoms experiments measurements are usually carried out by imaging processes, which permit to observe *in-situ* the realized ultracold gas density $n(\vec{r})$. The latter quantity allows to extract noteworthy physical quantities, like the number of atoms N, the temperature T of the cloud or the bulk chemical potential μ. The particular technique we employ is that of absorption imaging. In our experiment the imaging process is carried out by using the laser resonant with the D_2 transition in two distinct paths: one along the horizontal direction, with respect to the MOT chamber, and one along the vertical. Horizontal imaging employs a simple telescope, consisting of two lenses with focal lengths of 150 mm and 1000 mm respectively, providing a total magnification of 6.72. The atom image is focused on an Andor Ultra camera, set on the Fast Kinetic Series (FKS) acquisition mode, which allows for taking a sequence of a few images with a short delay time on the order of 200 μs. On the other hand, vertical imaging light propagates along the z-axis inside the science chamber, from top to bottom, passing through a high-resolution microscopic objective as shown in Fig 2.6: a resonant high-power laser beam is illuminated onto the atomic cloud, and the shadow due to the presence of atoms which have absorbed the light is focused by an optical setup on another Andor camera.

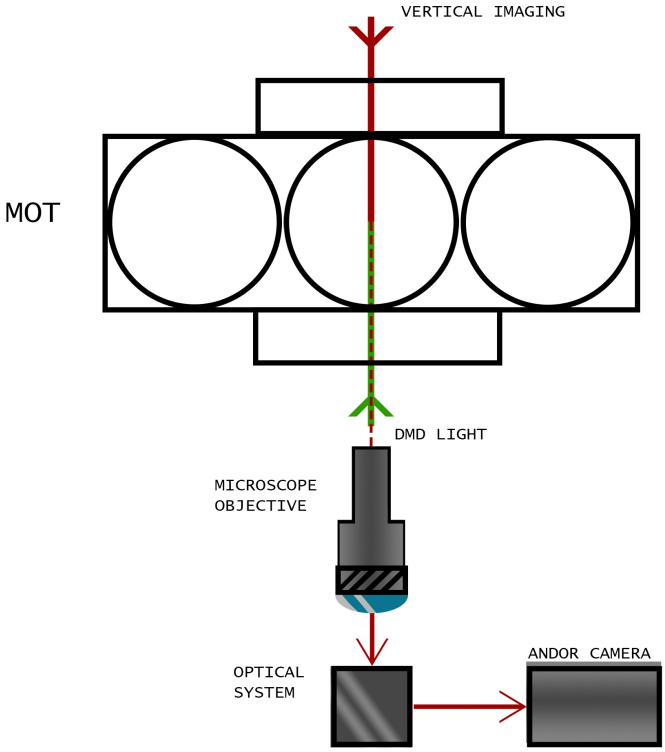

Figure 2.6: *Scheme of the lasers employed for the vertical imaging and the DMD trapping. Both employ a high-resolution microscopic objective. An optical system composed of elliptical mirrors and beam-splitter cubes focuses the laser light on the Andor camera.*

This process returns an image of the system together with a measurement of the optical column density OD, which is related to the atomic density $n(\vec{r})$ of the cloud on the x-y plane through a proportionality factor. The reason why we perform imaging with high intensity light is related to the optical density of the system: for low values of luminous intensity the number of transmitted photons through optically dense clouds is reduced, and the shadow of the atomic cloud saturates the image, since a small number of photons reaches the camera: in this situation the signal-to-noise ratio decreases accordingly. In addition we must also minimize the motion of atoms due to interactions with resonant photons, which occur during the imaging process, in order to increase the spatial resolution along the vertical direction. For this purpose we employ short imaging pulses with a duration of $4\,\mu$s and an intensity of $I \approx 3\,I_s$, where $I_s = \pi\,h\,c\,\gamma/3\lambda^3$ is the saturation intensity of the D_2 line; in these conditions, where the atomic transition is saturated, the *Lambert-Beer* law for light attenuation in materials modifies to:

$$\frac{dI}{dz} = -n(\vec{r})\,\sigma_{eff}\,\frac{I\,I_{eff}}{I + I_{eff}} \tag{2.1}$$

where I is the intensity of the light propagating along the z direction which shines the cloud of density $n(\vec{r})$, $\sigma_{eff} = \sigma_0/\alpha$ is an effective cross-section (where σ_0 is the cross section describing photon absorption processes for a non-saturated cloud), and $I_{eff} = I\beta$ is the effective saturation intensity. The factors α and β can be obtained by a calibration process, as discussed in Ref. [11]. Integrating Eq. (2.1) along the imaging direction (z-axis) yields the optical column density OD:

$$OD = -ln\left(\frac{I_{out}}{I_{in}}\right) + \frac{I_{in} - I_{out}}{I_{eff}} \tag{2.2}$$

where I_{in} and I_{out} are the incident and transmitted intensity, respectively. In our experimental setup, the 2-D atomic density on the trapping plane, $n_{2D}(x, y)$, can be calculated from the measured optical density OD by using the following relation [11]:

$$n_{2D}(x, y) = \frac{OD}{\sigma_0} \tag{2.3}$$

2.2 Digital micro-mirror device

In ultracold atom experiments Josephson junctions are made by trapping a gas in the superfluid state inside an optical dipole trap, usually realized with focused laser beams which produce an harmonic confining, as discussed in App. A.2. The atomic cloud is then bisected into two distinct reservoirs with the employment of an additional laser; this creates a potential barrier which acts as the analogue of the insulating layer used in superconducting Josephson junctions. If this barrier is sufficiently thin tunneling phenomena become important, and the Josephson dynamic sets in. In recent years the development of new technologies, such as spatial light modulators devices, has allowed for the possibility of sculpting the optical potential experienced by atoms. In our experiment we are able to confine the atoms in potentials of arbitrary shape thanks to the help of a *digital micro-mirror device* (DMD), allowing for the realization of Josephson junctions having different geometries: for this thesis work we mainly employed a hybrid potential that exerts an harmonic trapping along the vertical direction z, while in the x-y plane the cloud is confined within a rectangular box, to which corresponds an hard-box type potential. This hybrid confinement realizes the structure that makes up our atomic Josephson junction, where the ^{6}Li superfluid can be trapped. In our experiment we employ a Vialux V-7000 High-Speed Module DMD equipped with the Texas Instruments Discovery DLP7000 chip, which is composed by a 1024×768 array of square micro-mirrors of pitch $13.68\,\mu$m. When the device is powered down, each mirror lays on its rest position: the tilt state of a mirror can be controlled by turning on the DMD and by applying an external voltage, which can put the various micro-mirrors in the ON/OFF state depending on its sign. These two states correspond to an inclination of $12°/-12°$ with respect to the horizontal direction, as shown in Fig. (2.7).

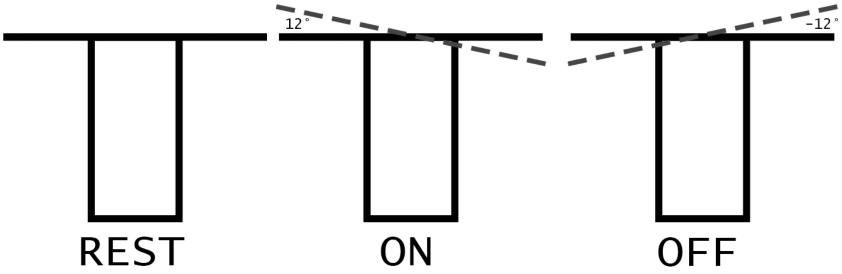

Figure 2.7: *Functioning of the DMD mirrors. When the device is turned off, the mirrors lay in the rest position. When the DMD is turned on, the application of an external voltage selectively turn the selected mirrors in the ON state: this results in the projection of the desired image on the atomic cloud.*

When an image is loaded onto the device, the mirrors of the DMD are arranged in a certain combination of ON-OFF states following the coding of the image, such that it is reproduced on the instrument's screen. If illuminated by an external laser source, the digital micro-mirror device reflects a pattern along the ON direction, having the same shape as the loaded image. In our experiment we shine on the DMD a green laser beam, with wavelength of 532 nm, and the reflection of the instrument is projected onto the atomic cloud, generating a repulsive optical dipole potential: this happens because the laser light is blue-detuned ($\delta = w_L - w_0 > 0$) with respect to the lithium fine doublet transitions. Since the DMD acts as a light mask, the potential which it creates mantains the original profile of the incident laser beam: in order to shine on the atoms dynamic potentials with an homogeneous profile, we need to remove the laser's Gaussian profile. This is done by a feedback program, which functioning is described in Ref. [40], that compares the measured DMD image with a target one and minimizes the error between the two by applying a pixel-by-pixel error correction matrix on the DMD mirror array configuration; the result is the creation of a spatially homogeneous potential. We can modulate the intensity of the trapping by adjusting an external parameter, the intensity threshold Int_{th}, which assumes values in the interval $\{0, 255\}$: the feedback program rescales the target image into grayscale at the beginning of the feedback routine, and the resulting potential will be more homogeneous for smaller values of Int_{th}. Another notable use of DMD is the possibility of creating obstacles within the Josephson junction; the most important of these is represented by a thin optical barrier, already shown in the center of Fig. 2.5, which allows for the study of Josephson dynamics. The barrier is realized as follows: first, we need to create a sequence of different images, such that the first image represents only the rectangular potential in the absence of the optical barrier, while in subsequent images a thin barrier is gradually raised in the desired position. This first image is then loaded onto the DMD, which proceeds to project it onto the atomic cloud. The loaded image is changed every 0.08 ms, following the order from the rectangular potential without the barrier up to the last image, where the thin barrier at its selected height is fully raised inside the junction. The DMD reproduces the different images by gradually turning various ON mirrors in the OFF state, so that at the end of the process the barrier is created almost adiabatically; this procedure is employed as it does not create perturbations related to density imbalances within the superfluid, like sound waves or shock waves. The created optical barrier has a width of about $1\,\mu$m (about 4 DMD pixels), which corresponds to our imaging resolution: its precise value, together with the trap depth V_0, has to be determined through a calibration procedure, as reported in Sec. 2.4. The microscope objective adopted in the absorption imaging setup along the vertical direction, where we employed a $621\,nm$ laser beam, can be also used to focus the $532\,nm$ light reflected by the DMD on the atomic cloud: this not only allows high resolution imaging, as already discussed, but also makes possible the projection of DMD made optical potentials defined over a micrometer length scale.

2.3 Hybrid trap properties

This section will be devoted in the calculation of thermodynamic properties of the ultracold ^{6}Li gas, trapped within the hybrid potential generated by the DMD; physical quantities like the Fermi energy E_F, the chemical potential μ or the speed of sound c_s will be investigated in our particular trap geometry. The rectangular hybrid potential, which creates an harmonic confinement along the vertical direction and behaves like a rigid box along the x-y plane, can be written as:

$$V_T(\vec{r}) = \frac{1}{2} m w_z^2 z^2 + V_{box}(x, y) \tag{2.4}$$

where w_z is the trapping frequency along the vertical, while $V_{box}(x, y)$ is the box potential on the x-y plane, supposed to be of the hard-wall type:

$$\begin{cases} V_{box}(x,y) = 0 & \text{for } |x| < L_x \ \vee \ |y| < L_y \\ V_{box}(x,y) = \infty & \text{for } |x| > L_x \text{ or } |y| > L_y \end{cases} \tag{2.5}$$

where L_x and L_y are the sides of the rectangle-shaped potential. We can calculate the Fermi energy E_F of a degenerate gas in such a potential by inserting the potential of Eq. (2.4) inside the expression for the total number of particles N, Eq. (1.17), obtaining:

$$N = \frac{g_s}{6\pi^2}\left(\frac{2m}{\hbar^2}\right)^{3/2} \int_{-L_x/2}^{L_x/2} dx \int_{-L_y/2}^{L_y/2} dy \int_{\mathbb{R}} dz \left(E_F - \frac{1}{2} m w_z^2 z^2\right)^{3/2} \tag{2.6}$$

Integrating Eq. (2.6) gives the total number of atoms N, and the Fermi energy E_F can be simply found by inverting:

$$E_F = \left(\frac{N 4\pi\hbar^3 w_z}{g_s m L_x L_y} \right)^{1/2} \tag{2.7}$$

We can also calculate the chemical potential μ in this particular trap configuration by integrating Eq. (1.67), in the different cases of the BEC-BCS crossover, to obtain the total number of atoms N: by inverting this result and inserting the appropriate coefficients γ and g_γ, shown in Tab. 1.1, we obtain the desired expression for μ. In the strongly interacting unitary regime we arrive at:

$$\mu_{UFG} = \xi^{3/4}\, E_F \tag{2.8}$$

where ξ is the Bertsch parameter defined in Sec. 1.4, while E_F is the Fermi energy reported in Eq. (2.7). The same calculation in the BEC regime returns the following chemical potential:

$$\mu_{BEC} = \left(\frac{N 3\pi\hbar^2 a_M w_z}{2 L_x L_y \sqrt{m}} \right)^{2/3} \tag{2.9}$$

Finally, in the BCS regime, we retrieve the non-interacting result of Eq. (1.58):

$$\mu_{BCS} = E_F \tag{2.10}$$

Sound velocity

We can also calculate the velocity of the sound modes in this trap profile. We recall that the sound velocity c_s is related to the chemical potential $\mu(\vec{r})$ by the following equation:

$$c_s = \left(\frac{n(\vec{r})}{M} \frac{\partial \mu}{\partial n(\vec{r})} \right)^{1/2} \tag{2.11}$$

where n is the cloud density, while M is the mass of the atom pair. In the framework of the polytropic approximation discussed in Sec. 1.4, we can substitute Eq. (1.66) for the chemical potential μ along the whole BEC-BCS crossover inside Eq. (2.11), obtaining the following expression for the sound velocity:

$$c_s = \left(\frac{\gamma\, g_\gamma\, n(\vec{r})^\gamma}{M} \right)^{1/2} = \left(\frac{\gamma \mu(\vec{r})}{M} \right)^{1/2} \tag{2.12}$$

We can calculate the speed of sound c_s across the BEC-BCS crossover by substituting the correct parameters γ and g_γ, reported in Tab. 1.1. We obtain the following results:

$$\begin{cases} c_s = \sqrt{\dfrac{\mu(\vec{r})}{M}} & \text{(BEC)} \\ c_s = \sqrt{\dfrac{\xi^{3/4}}{3}}\, v_F & \text{(UFG)} \\ c_s = \dfrac{1}{\sqrt{3}}\, v_F & \text{(BCS)} \end{cases} \tag{2.13}$$

where $v_F = \sqrt{2\, E_F / M}$ is the Fermi velocity. We notice how, in the BEC case, the speed of sound c_s depends on the square root of the chemical potential μ and, consequently, on the cube root of the average cloud's density on the x-y plane, $n = N/L_x L_y$.

2.4 Barrier creation and calibration

As explained in Sec. 2.2, the DMD employs a feedback program in order to cut the optical potential to the desired height, so that the resulting confinement is homogeneous in the x-y plane. Moreover, it is possible to separate the superfluid into two independent reservoirs by raising a thin repulsive optical barrier in the desired position, such that the two sides of the junction can communicate with each other through tunneling phenomena, as explained in Sec. 1.6. This potential barrier can be characterized by two notable quantities: the trap depth V_0 and the barrier width σ. To adjust the height of the optical potential we can vary two external variables:

1. The power of the green 532 nm laser illuminating the DMD, $P_{DMD}\,(\mathrm{mW})$.
2. The auxiliary variable intensity threshold Int_{th}, which value can be set between 0 and 255 and determines the combination of mirrors in the ON state.

In order to estimate the potential barrier's depth V_0 (in Hz units) and width σ (in μm units) a calibration process is required, in order to relate the intensity of the optical trapping with the adjustable parameters Int_{th} and $P_{DMD}\,(\mathrm{mW})$: the actual height U_0 of a generic optical potential, exerted on the atoms due to the DMD setup, is directly proportional to the product of these parameters through a proportionality factor α:

$$U_0 = \alpha \cdot Int_{th} \cdot P_{DMD}\,(\mathrm{mW}) \tag{2.14}$$

which has to be determined by the calibration. The technique we adopt for deriving this factor is that of *dynamical phase imprinting*: one of the two reservoirs composing the atomic cloud is illuminated with an optical dipole potential U_0, generated by the DMD, for a certain time interval Δt. If Δt is shorter than the typical time of atomic motion, $\Delta t < \hbar/\mu$, where μ is the chemical potential of the ultracold gas, the light imprints on the wave function Ψ of the selected condensate a phase of $\hbar\,\phi = U_0\,\Delta t$, which can be measured by exploiting interference phenomena, as described below. The phase imprinted on the illuminated side of the system, using Eq. (2.14), becomes:

$$\hbar\,\phi = \alpha \cdot Int_{th} \cdot P_{DMD}\,(\mathrm{mW}) \cdot \Delta t \tag{2.15}$$

Dividing Eq. (2.15) by the Planck constant h leads us to the following result:

$$\tilde{\phi} = \frac{\phi}{2\pi} = \frac{\alpha}{h} \cdot Int_{th} \cdot P_{DMD}\,(\mathrm{mW}) \cdot \Delta t = \tilde{\alpha} \cdot Int_{th} \cdot P_{DMD}\,(\mathrm{mW}) \cdot \Delta t \tag{2.16}$$

where $\tilde{\phi} = \phi/2\pi$, while $\tilde{\alpha} = \alpha/h$. On the other hand, the non-illuminated reservoir acts as a phase reference, such that we can measure the relative phase ϕ between the two reservoirs; this measurement is carried out by interfering the condensates wave functions through the *time-of-flight* technique (TOF). In this method, all optical trapping potentials are turned off and the system is left evolving, such that the matter waves associated with the two independent superfluids interfere: after 6 ms the absorption imaging process is performed, extracting the density profile of the cloud. First of all, the following periodic function is fitted to the interference pattern data, leaving the relative phase ϕ and the fringe wavelength λ as free parameters:

$$f(x) = A \cdot cos(\phi + 2\pi\,\lambda\, x) + off \tag{2.17}$$

An interference pattern is reported as an example in Fig. 2.8 (a), together with its corresponding density profile curve fit, shown in Fig. 2.8 (b).

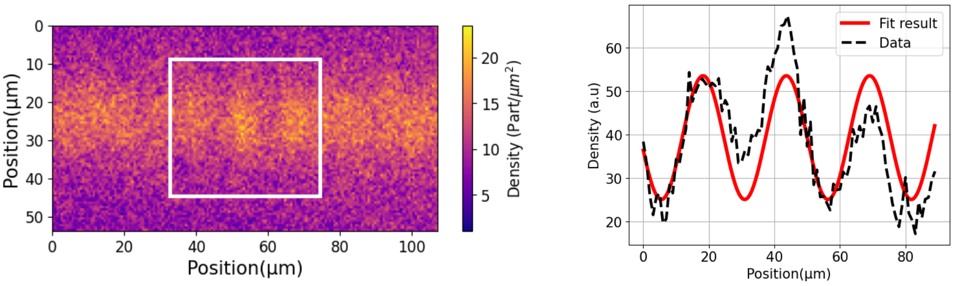

(a) Interference pattern. **(b)** Fit result.

Figure 2.8: *On the left panel (a), density profile of the two superfluids after a 6 ms TOF procedure, where we can see at least three separate fringes: its relative color scale is reported on the right side. On the right panel (b), the fit of such interference pattern, effectuated with Eq. (2.17), in the region surrounded by the white rectangle.*

We can calculate an average fringe wavelength $\bar{\lambda}$, by considering the mean value of the wavelengths λ extracted from the fits made with Eq. (2.17), shown in Fig. 2.9, obtaining the result $\bar{\lambda} = (25.4 \pm 0.4)$ Andor pixels.

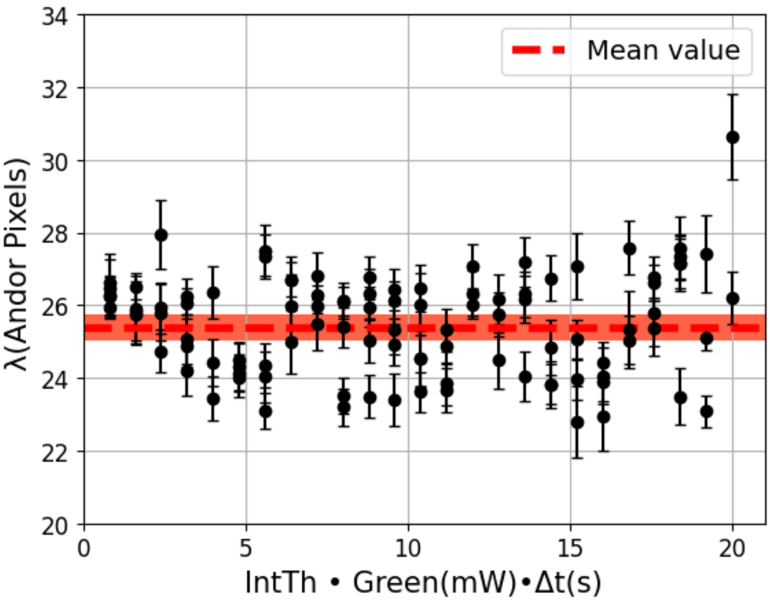

Figure 2.9: *Fringes wavelength extracted from various fits effectuated with Eq. (2.17), as a function of* $Int_{th} \cdot P_{DMD}\,(mW) \cdot \Delta t$*: an horizontal dashed line reports its mean value, which is found to be* (25.3 ± 0.4) *Andor pixels.*

The interference profiles are fitted again by fixing the wavelength to this average value $\bar{\lambda}$, leaving only the relative phase ϕ as a free parameter. This process is done since, in general, the parameters ϕ and λ could be dependent from each other: by constraining $\lambda = \bar{\lambda}$, a value which should only depend on the TOF duration (6 ms in this case), we obtain a better estimate for the relative phase ϕ. The phase extrapolated from the different fits, as a function of $Int_{th} \cdot P_{DMD}\,(\mathrm{mW}) \cdot \Delta t$, is finally fitted with a straight line, using Eq. (2.16). In our experiment we perform this process for five different phase imprinting times Δt: we report the fit results for the phase $\tilde{\phi}$ in Fig. 2.10 (a).

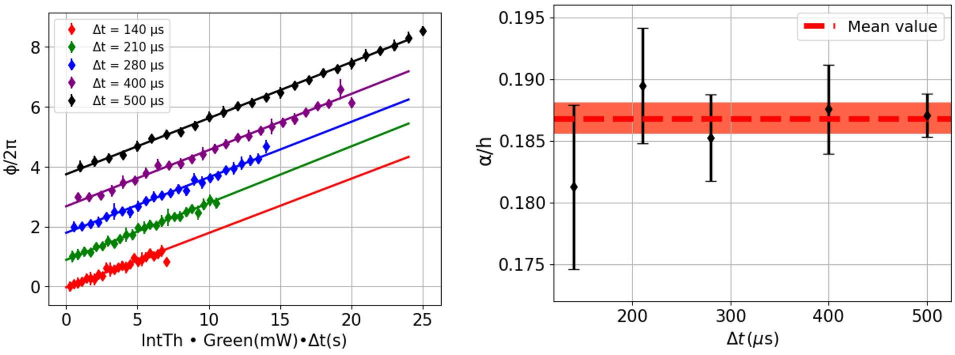

(a) Relative phase fit results

(b) Alpha fit results

Figure 2.10: *On panel, (a), the fit of the phase* $\bar{\phi}$ *for differents imprinting times, effectuated with Eq. (2.16), in order to extract the slope of the straight line. Data and fits are shifted in the vertical by* $\phi/2\pi = 1$ *between each other in order to to improve the visibility of the image. On panel (b), we report the value of* $\bar{\alpha}$ *extracted from fits, as a function of the imprinting time* Δt*. The dashed red line represent its mean value of* $\bar{\alpha} = 0.187 \pm 0.001$*, together with its error bar.*

The slope of the lines returns the value of the calibration factor $\tilde{\alpha}$ for the different imprinting times Δt. Since in principle the calibration parameter $\tilde{\alpha}$ should not depend on the imprinting time Δt, its mean value is assumed to be the best value, calculated by averaging the results of the various fits: this returns a mean value of $\bar{\alpha} = 0.187 \pm 0.001$, as shown in Fig. 2.10 (b). Knowing the value of $\tilde{\alpha}$, we could calculate the height U_0 of a generic potential just by using Eq. (2.14). Now the problem becomes how to determine the real height V_0 of the thin optical barrier, created inside the atomic Josephson junction, as a function of the set intensity threshold value Int_{th}^{Set} which, in principle, could differ from the measured value Int_{th}^{Meas} because of the finite resolution of the DMD-projecting optical system: another calibration procedure is therefore necessary, in order to relate together the latter quantities. Since the created Josephson barrier has a dimension comparable with the resolution of the imaging objective, equal to $1\,\mu$m, a final calibration is needed for calculating its effective trapping depth V_0, experienced by the atomic cloud. The first process to be carried out is the calibration of Int_{th}^{Set} itself: this is done by projecting an homogeneous area on a secondary Thorlabs camera placed in the DMD optical setup, and by calculating the average number of countings which occur in a certain cut region as Int_{th}^{Set} is modulated. This area must be small enough to present an approximately homogeneous counting profile, which for high intensity threshold values has a Gaussian profile. Specifically, the calibration is carried out by fitting the following function to the average of the counts in the area, as a function of Int_{th}^{Set}:

$$Int_{th}^{Meas} = \gamma \cdot Int_{th}^{Set} \tag{2.18}$$

thus returning the value of the proportionality factor γ between the effective intensity threshold Int_{th}^{Meas} and the set one Int_{th}^{Set}. An example of one homogeneous area and its corresponding cut, employed for fitting Eq. (2.18), is reported in Fig. 2.11 (a), while the obtained curve fit is reported in Fig. 2.11 (b).

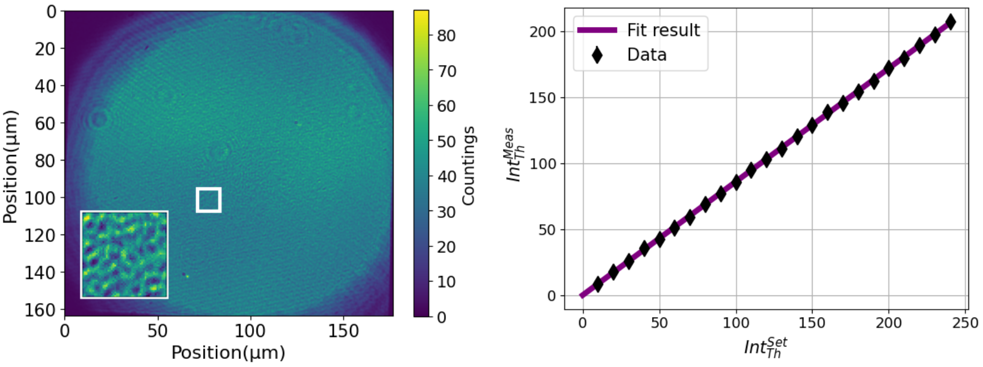

(a) Homogeneous area.

(b) Fit results.

Figure 2.11: ***(a)***: *Homogeneous area for a set value of* $Int_{th}^{Set} = 50$*, reported together with its corresponding cut (bottom left), effectuated in the region surrounded by the white rectangle where we calculate the average counting number* Int_{th}^{Meas}.
(b): *Fit result of equation Eq. (2.18), effectuated for the measured value of intensity threshold* Int_{th}^{Meas} *against the set value* Int_{th}^{Set} *. The slope of the straight is found to be* $\gamma = 0.859 \pm 0.002$.

In our experiments, the intensity threshold is always set to a constant value of $Int_{th}^{Set} = 110$ when realizing the thin optical barrier, constituting the Josephson insulating obstacle. The last necessary step for estimating the real height of the optical barrier, which depends on the provided Int_{th}^{Set} and on the applied power of the green laser P_{DMD}(mW), is to effectuate a 1-D Gaussian fit of the barrier profile through the following equation:

$$G(x) = off + H \cdot e^{-2(\frac{x-x_0}{\sigma_x})^2} \tag{2.19}$$

where x_0 is the Gaussian center, σ_x is the variance (estimating the barrier width σ) while H is the Gaussian amplitude, related to the barrier's height V_0. In order to probe the transport properties of our superfluid Josephson junction we have to inject a tunable particle current: this is operatively done by displacing the thin optical barrier inside the trapping potential, at a controllable velocity, as explained in Secs. 3.2 and 4.1. Therefore, we also need to investigate the barrier's properties as a function of the position within the junction, addressing eventual fluctuations or imperfections. This characterization is carried out by creating a rectangular potential which contains multiple barriers in different positions, each one of them having the same thickness, as shown in Fig. 2.12: their height H and width σ are extracted by fitting Eq. (2.19).

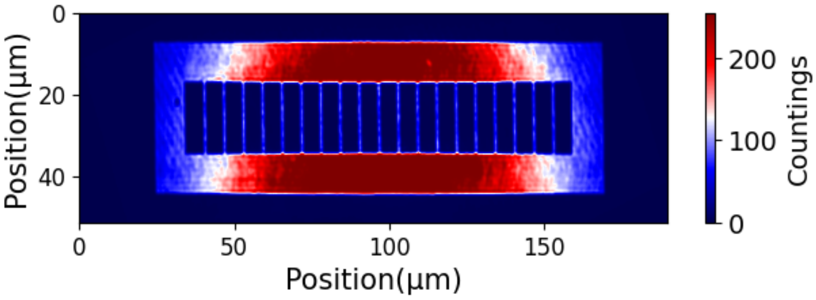

Figure 2.12: *Single rectangular optical dipole potential, having multiple thin barriers in different positions.*

Moreover, a 1-D Gaussian filter is applied to each image in order to keep into account the finite resolution of the optical system traversed by the laser beams: this technique gives a better estimate of the real optical potential experienced by the atoms. Fit results are reported in Figs. 2.13 (a) and 2.13 (b) as a function of the position within the optical potential: we notice how the Gaussian height H and width σ are approximately constant for different positions, reflecting how the Josephson barrier's properties are well defined throughout our junction. We can therefore provide a reliable estimate for the barrier's depth

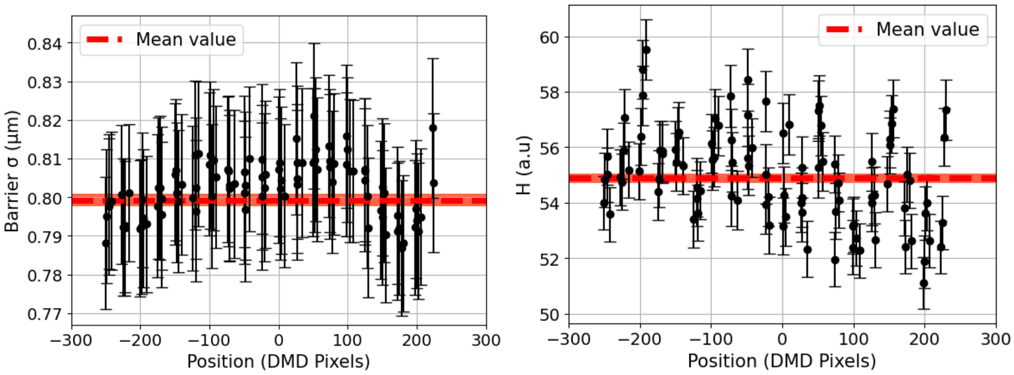

(a) Fit results (σ)

(b) Fit results (H)

Figure 2.13: ***(a)**: Fit results for the Gaussian variance σ, as a function of the position inside the trapping potential.*
***(b)**: Fit results for the barrier depth $\bar{H}$, here called amplitude. Red dashed lines report the mean value of both quantities, together with their error bars. We find that $\bar{\sigma} = (0.80 \pm 0.02)\,\mu m$, while $\bar{H} = (55 \pm 2)$ a.u.*

and width by taking the values $\bar{H} = (55 \pm 2)$ a.u. and $\bar{\sigma} = (0.80 \pm 0.02)\,\mu$m, obtained by averaging the fit results. The height of the barrier in terms of the set intensity threshold Int_{th}^{Set} can be calculated from the fitted $\bar{H}$ as follows:

$$Int_{th}^{Barrier} = Int_{th}^{Set} \cdot \frac{\bar{H}}{Int_{th}^{Meas}} = \frac{\bar{H}}{\gamma} \tag{2.20}$$

where in the second passage we used Eq. (2.18). Finally, the real barrier height in frequency units, $V_0\,(\mathrm{Hz})$, can be obtained by means of Eq. (2.14), dividing both sides of the equation by h:

$$V_0\,(\mathrm{Hz}) = P_{DMD}\,(\mathrm{mW}) \cdot \bar{\alpha} \cdot \frac{\bar{H}}{\gamma} = P_{DMD}\,(\mathrm{mW}) \cdot \Gamma \tag{2.21}$$

where $\Gamma = \bar{\alpha} \cdot \bar{H}/\gamma$ is the total calibration factor, which is measured to be $\Gamma = 11.9 \pm 0.6$. The obtained V_0 provides a scale of energy comparable with the chemical potential μ of the system; the V_0 over μ ratio allows to determine if the system can perform Josephson dynamics through tunneling phenomena. Typical values for the DMD optical potential power are about $P_{DMD}\,(\mathrm{mW}) = 130\,\mathrm{mW}$, while the chemical potential in the BEC regime can be calculated by using Eq. (2.9): in a rectangular Josephson junction of size $125 \times 17.5\,\mu\mathrm{m}^2$, having $N \sim 2 \cdot 10^4$ atoms and a vertical trapping (angular) frequency of $w_z = 2\pi \cdot 420\,\mathrm{Hz}$, its value is estimated to about $\mu_{BEC} \sim 1.2\,\mathrm{KHz}$ (in frequency units). The parameter V_0/μ is therefore found to be approximately $V_0/\mu \sim 1.3$ in this setup. Another interesting parameter to be considered is the ratio between the healing length ξ, introduced in Eq. (1.56), and the average barrier width $\bar{\sigma}$. Since for the parameters given above we have that $\xi \sim 0.6\,\mu\mathrm{m}$, this ratio is calculated to be approximately $\xi/\bar{\sigma} \sim 0.75$. As discussed in Sec. 1.4, the healing length ξ represent the distance over which a BEC restores its density after experiencing a perturbation, and can be associated with the extension of the macroscopic wave function Ψ associated the condensate: when this parameter is too small with respect to the average barrier size $\bar{\sigma}$, the order parameters associated with each reservoir do not overlap within the barrier region, which thus acts as a thick insulating barrier and inhibits tunneling phenomena. Conditions $V_0/\mu > 1$ and $\xi/\bar{\sigma} \sim 0.75$ ensure that we are fully in the tunneling regime, where the Josephson dynamics is capable of setting in and atom pairs can move from one side of the junction to the other, traversing the optical barrier.

Chapter 3

Atomic Josephson junction characterization

In ultracold atom physics experiments, Josephson junctions are constituted by two superfluid reservoirs separated by a thin optical barrier, such that the corresponding order parameters overlap within the barrier region; this situation allows for the tunneling of atoms across the obstacle. Superconducting and superfluids Josephson junctions are expected to posses similar transport properties since their macroscopic wave function Ψ, describing the low-temperature condensed state, is represented by Eq. 1.74 in both cases. These devices allow for a direct measurement of the most elusive physical quantity associated with the order parameter: the relative phase ϕ between the two superfluids, which, for barriers with a sufficiently low transmission probability, is connected with the supercurrent flowing inside the system through the sinusoidal current-phase relation reported in Eq. (1.82) [3, 19]. The latter dependence can be investigated by injecting a direct current inside the system, exploring the *DC Josephson effect*. On the other hand, when a finite initial chemical potential difference $\Delta\mu$ is preliminarly created within the system, we expect to observe coherent oscillations at the same frequency of both the relative phase ϕ between the superfluids and the atom density n (or, equivalently, of the $\Delta\mu$), out of phase by $\pi/2$ [55, 12, 25]; this constitutes the *AC Josephson effect*. Both of these phenomena are a manifestation of the system's macroscopic quantum phase coherence, and represents the physical basis of many remarkable applications: for example, in the field of metrology, it is employed for high-precision measurements [56]. Usually, ultracold Josephson junctions are realized with a superfluid trapped inside a 3-D harmonic optical trap, where a focused laser beam bisects the cloud into two distinct reservoirs, acting as a thin insulating barrier: this microscopic device has been studied under the theoretical framework of a two-well potential model [57, 58]. The system investigated in this thesis presents a simpler trapping geometry, as we employ a *digital micro-mirror device* in order to project onto the atomic cloud a rectangular optical potential, which exerts a repulsive trapping, as discussed in Sec. 2.2. In the present chapter we report the characterization of the elongated Josephson junction adopted in our experimental setup, investigating its transport properties and measuring its noteworthy physical quantities, like the critical current I_c, the speed of sound c_s or the plasma frequency ω_J, which describes the coherent oscillations in time occurring in the AC Josephson regime. In Sec. 3.1

measurements regarding the speed of sound modes c_s are reported, together with its expected value, calculated from Eq. (2.12): this allows to characterize the speed of density perturbations which can be excited inside the ultracold cloud, and how dissipative phenomena in the physical system affect its value with respect to the theoretical one. In order to investigate our physical system and its transport properties, we need to inject an external tunable current inside the optical potential; as our Josephson junction only contains neutral ultracold atoms, isolated from the external environment, this request constitutes a difficult challenge. In Sec. 3.2 we explain how the DMD ability of shining dynamic potentials onto the atomic cloud allows to inject a particle current within our system. The coherent oscillations of both the chemical potential difference $\Delta\mu$ and the relative phase ϕ between the reservoir's wave functions is reported in Sec. 3.3, where we observe the AC Josephson effect: by measuring the phase difference between these oscillations we demonstrate that our junction is indeed in the Josephson regime, where particle transport occur due to tunneling phenomena, probing also the macroscopic phase coherence which characterizes the superfluid state. In Sec. 3.4 we will report the measurements of the DC Josephson effect, obtained by displacing the thin optical barrier at a constant speed in order to generate a direct atomic current: the behavior of important parameters, namely the conductance G and the critical current I_c, will be investigated as a function of the system linear size L_x and of the applied laser power, P_{DMD}(mW). Finally, in Sec. 3.5 we report the measured frequency of the coherent oscillations which occur during the AC Josephson dynamics, as a function of the same quantities. We will also show the experimental results for the density oscillations triggered by the creation of an initial sound excitation, which tunnels back and forth through the optical barrier; the values of the measured frequency corroborates the hypothesis where the behavior of the Josephson oscillations is altered due to coupling mechanisms between the Josephson dynamics and the sound modes.

3.1 Speed of the sound modes measurements

A fundamental phenomena associated with ultracold quantum gases is constituted by the existence of collective modes. They can be divided into two distinct categories, which properties mostly depends on interparticle interactions: collisionless modes and hydrodynamic modes. In particular hydrodynamic modes emerge as a consequence of the presence of interactions in the condensate [59]. A notable example is represented by sound excitations, which propagate within a superfluid at the speed of sound c_s, as introduced in Sec. 2.3. This quantity, which depends on the junction's properties, can be easily measured in our experiment, where the tunability of the repulsive optical potential allows for a dynamical excitation of sound modes. The starting point for our experiment is the creation of a superfluid of ^{6}Li, in the desired interaction regime of the BEC-BCS crossover, trapped in the hybrid rectangular potential created by the DMD; this occurs after the various processes of laser cooling and trapping, as explained in Sec. 2.1. In particular, in this measurement, as in many others within this thesis work, we investigated the ultracold gas of ^{6}Li in the BEC regime, where interactions are weak and repulsive ($1/k_F a \gg 1$), and molecular bound states are allowed. This regime is obtained by applying a magnetic field of about 632 G, in order to exploit the Feshbach resonance of the $|1\rangle$ and $|3\rangle$ Zeeman substates, as discussed in Sec. 2.1. The presence of the thin optical barrier within the potential is not necessary to measure the speed of sound c_s, since we only need to generate a sound excitation which has to propagate freely inside the condensate. To create a sound wave we control the optical potential via an external program running on a python script, *Spyder*, which can create the desired sequence of images to be loaded onto the DMD; these images are shifted between each other via a series of subsequent triggers. This procedure allows to set a wide variety of parameters in order to modify the junction's geometry or its profile during time: in our case we compress one side of the junction, in a non-adiabatic process, to subsequently stretch it back to its original size. The latter process excites a sound mode, which propagates within the superfluid at a certain speed c_s, to be determined experimentally. Absorption imaging is then effectuated at different times, in order to record the time evolution of the density profile within the cloud; the starting time, $t = 0$, is taken when the shape of the potential is restored to its original condition, after the initial compression. The position of the density excitation within the cloud at a certain time can be found by fitting a $1 - D$ Gaussian curve on the integrated density profile along the y-axis:

$$f(x) = off + A \cdot e^{\dfrac{-(x-x_0)^2}{\sigma^2/2}} \tag{3.1}$$

where A is an amplitude, x_0 is the sound pulse position, σ is the variance and off is a constant offset. Examples of the generated sound wave propagation within the optical potential are reported in Fig. 3.1, at different times, together with the corresponding curve fits of their integrated density profiles, effectuated through Eq. (3.1); this fitting procedure returns the position $x(t)$ of the sound excitation as a function of the time. The speed of sound c_s, supposing a density propagation with constant velocity, can be extrapolated by fitting the following equation, describing an uniform linear motion, to the sound-wave position $x(t)$ as a function of the time t:

$$x(t) = c_s\, t + x_0 \tag{3.2}$$

where x_0 is a position offset. We report the obtained curve fit in Fig 3.2, for different compression sizes: the fitted straight lines are parallel to each other, compatibly with their error bars, suggesting that the excited density pulses propagate at a velocity which doesn't depend on the particular compression applied. Therefore, the speed of density excitations is well defined within our system. Its expected value, calculated from Eq. (2.13) with $N = 2.7 \cdot 10^4$ atoms, $\mu \sim 1440\,\mathrm{Hz}$ and $M = 2\,m = 2 \cdot 9.9883414 \cdot 10^{-27}\,\mathrm{Kg}$, in a trapping potential of sizes $125 \times 17.5\,\mu\mathrm{m}^2$, is found to be about $7\,\mathrm{mm/s}$; the measurement process returns an average speed of $\bar{c}_s = (6.09 \pm 0.04)\,\mathrm{mm/s}$, calculated by taking the mean value of the various c_s obtained through curve fitting. The latter value is of the same order of magnitude as the predicted theoretical value of $7\,\mathrm{mm/s}$, but not fully compatible within its experimental error bar. This small discrepancy may arise due to the fact that during the compression of the optical potential we aren't solely exciting sound modes, but also density shock

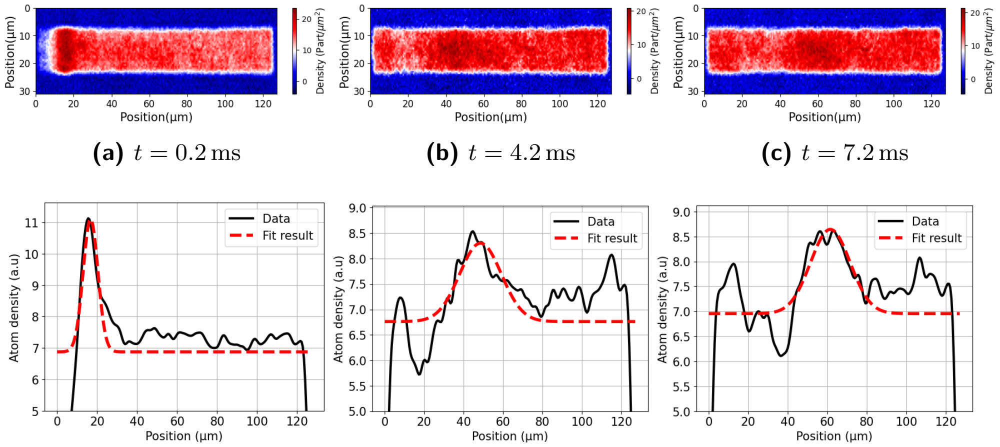

(a) $t = 0.2\,\mathrm{ms}$ **(b)** $t = 4.2\,\mathrm{ms}$ **(c)** $t = 7.2\,\mathrm{ms}$

Figure 3.1: *Sound excitation dynamics after the compression of the optical potential, where we clearly notice a density pulse (the dark red region, in our colorscale) propagating inside the cloud, from left to right, as time increases (Fig. (a) to (c)): its corresponding color scale, reporting the cloud's density, is shown on the right. The Gaussian fits of the density profiles as a function of the position, using Eq. (3.1), are reported underneath the corresponding figure; this procedure accurately extracts the pulse's position* x_0 *within the trapping potential, at different times.*

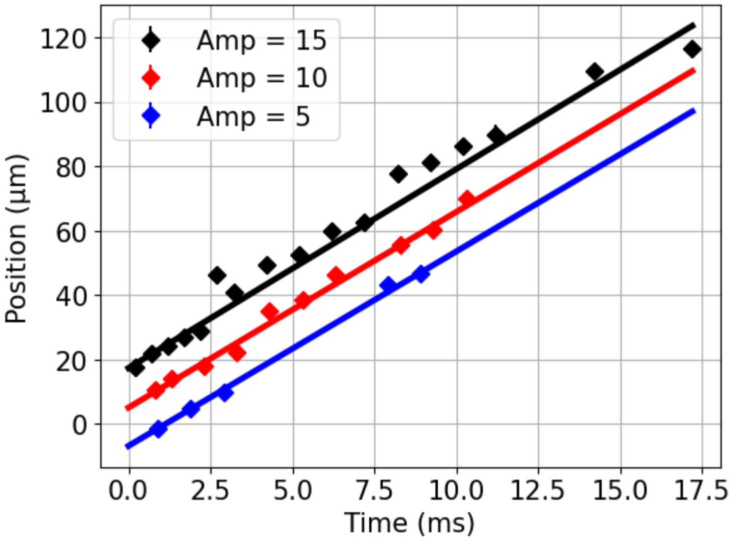

Figure 3.2: *Curve fit of the pulse's position (straight lines) at different times, for different compression amplitudes, labeled as* ***Amp*** *in the plot's legend; the three curves are shifted along the vertical direction in order to enhance visibility. Data is fitted with Eq. (3.2) in order to extract the straight's slope, giving an estimate of the sound velocity* c_s*. The three straight lines are approximately parallel between each other, returning a mean sound velocity of about* $\bar{c}_s = 6.09 \pm 0.04$ *mm/s.*

waves, whose propagation dynamics within the superfluid differ from those of the sound modes: in particular, their velocity is predicted to be higher than the corresponding sound velocity c_s [60].

3.2 Direct currents in isolated atomic junctions

In order to investigate the DC Josephson effect in superconducting junctions the application of a direct current I_{DC} is required, as it allows to study the transport properties of the system and to measure important parameters which characterize the junction itself, such as the critical current I_c; in the framework of circuital models, discussed in Sec. 1.6, quantities like the resistance R and the capacitance C can also be extracted, depending on the model chosen to represent experimental data. Being our atomic Josephson junction an isolated system composed of neutral atoms, unlike the corresponding superconducting device, the problem of injecting an external current in order to probe the DC Josephson effect represents a non-trivial task. To solve this problem, in our experimental apparatus we exploit the ability of the digital micro-mirror device to create dynamic potentials. In order to generate an atomic current, not provided from the outside, the optical barrier can be displaced inside the Josephson junction [19, 20]: this causes a non-resistive flow of atoms in the opposite direction due to the quantum tunneling if the velocity of the barrier is smaller than a critical value v_c, the critical velocity, which can be related to the Josephson critical current I_c described in Sec. 1.6. The trapping setup employed in our experiment is such that the ^{6}Li superfluid presents an homogeneous density profile on the x-y plane, enabling the stable injection of a current $I(t)$, which does not depend on the position but rather only on the instantaneous velocity $v(t)$ of the barrier:

$$v(t) = \frac{L_y \, I(t)}{\tilde{n}} = \frac{L_x \, I(t)}{N} \tag{3.3}$$

where we assumed propagation of the current along the x direction in the rectangle potential with sides L_x and L_y, while N is the total number of atoms in the junction and $\tilde{n}$ is the cloud density along the x-y plane. The movement of the optical barrier inside the Josephson junction is carried out by a Python program, which allows to select the desired barrier speed v_0: a certain number of images, representing the motion of the barrier in time, are then generated and loaded onto the DMD, which projects a repulsive potential on the ultracold cloud having the same shape of the chosen images, as explained in Sec. 2.2. The device is triggered to shift periodically between these images, following the barrier's motion: this produces an atomic current in the opposite direction with respect to the barrier's movement. We can modulate a wide range of parameters in order to represent different scenarios; in the case of a direct current (DC driving), the equation of motion of the barrier is set to be:

$$x(t) = x_0 + v_0 \, t \tag{3.4}$$

so that other than the barrier's velocity v_0 we can also adjust the initial position of the barrier x_0. Another parameter we can tune in our measurements is represented by the time of the barrier's movement t_{barr}, which establishes the distance covered by the barrier during its displacement through Eq. (3.4).

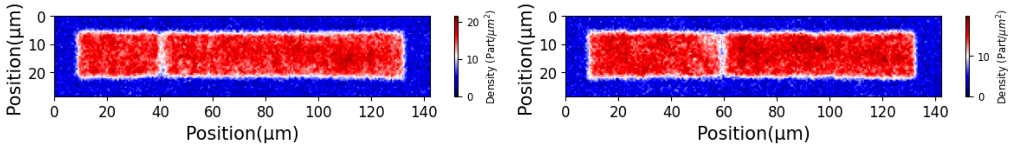

(a) $t = 0\,\mathrm{ms}$ **(b)** $t = 18.8\,\mathrm{ms}$

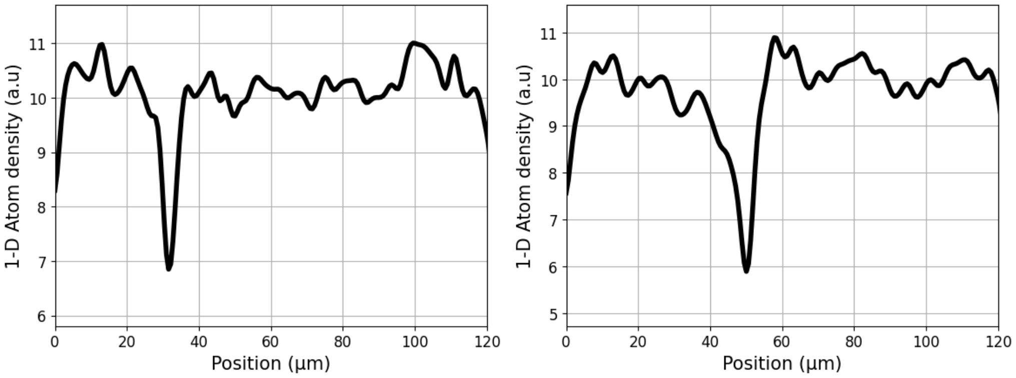

(c) $t = 0\,\mathrm{ms}$ **(d)** $t = 18.8\,\mathrm{ms}$

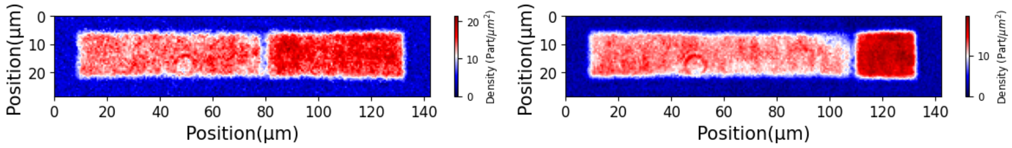

(e) $t = 38.8\,\mathrm{ms}$ **(f)** $t = 68.8\,\mathrm{ms}$

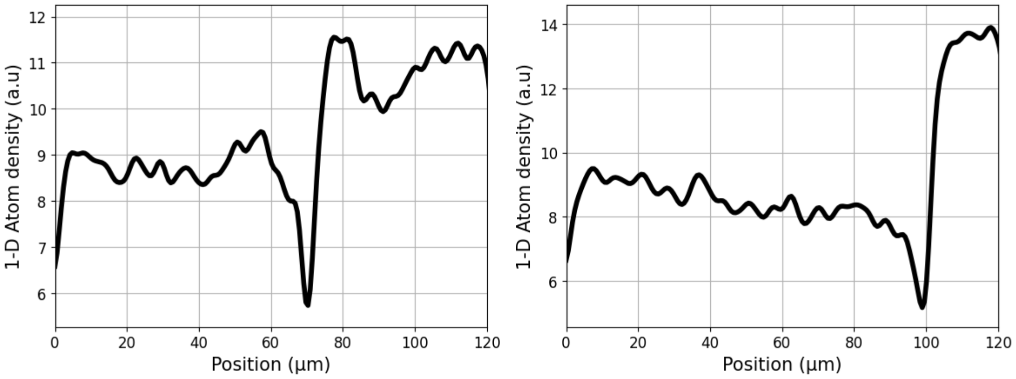

(g) $t = 38.8\,\mathrm{ms}$ **(h)** $t = 68.8\,\mathrm{ms}$

Figure 3.3: *Junction response to a DC current injection at different times, where the initial time* $t = 0\,ms$ *is taken when the optical barrier starts moving inside the Josephson junction. The color scale reports the cloud 2-D density. The barrier's velocity is set to* $v_0 = 1\,mm/s$. *The plots below report the corresponding 1-D density of the cloud, integrated along the y-axis,* $n_{1D}(x) = \int n_{2D}(x, y)dy$. *We clearly observe the build-up of a non-zero* $\Delta\mu$ *on the right side with respect to the barrier's driving, as time increases: atoms accumulate on one side of the junction due to resistive effects.*

An example of the barrier movement during time inside our junction is shown in Fig. 3.3, for a $125 \times 17.5\,\mu\mathrm{m}^2$ rectangular potential. The DMD therefore allows to explore different regimes within the Josephson junction: in the presence of a constant velocity v_0 we can probe the Josephson DC effect, where a finite chemical potential difference $\Delta\mu \neq 0$ is expected to occur when a certain critical barrier velocity v_c (or, equivalently, a critical current I_c) is exceeded. The DMD also permits to drive the barrier with an additional modulation, thus allowing to explore a totally different transport regime, physically enriched with respect to the DC Josephson effect: in fact the application of an alternating current $I_{ext}(t)$ to a superconducting Josephson junction causes the emergence of *Shapiro steps*, described in Sec. 1.6.4. The procedure for modulating the optical barrier is reported in Chap. 4, where the measurements of Shapiro steps are discussed.

3.3 Current-phase Josephson oscillations

In order to perform the characterization of the atomic Josephson junction inside the rectangular trap, it is first necessary to ensure that the many-body system we experimentally realize is well described in terms of the Josephson Hamiltonian shown in Eq. (1.86). Its major consequences, the Josephson-Anderson Eqs. (1.88) and (1.90), predict that for a small applied chemical potential difference, $\Delta\mu \neq 0$, the system should undergo Josephson oscillations at the plasma frequency ω_J, reported in Eq. (1.87). In particular, we expect that in the tunneling regime, where $V_0/\mu > 1$, the chemical potential difference $\Delta\mu$ and the relative phase ϕ between the two superfluids oscillate with the same frequency, having a relative phase shift $\Delta\Phi$ of about $\pi/2$: this is a consequence of the macroscopic quantum phase coherence of the condensed state, where the quantities $\Delta\mu$ and ϕ behave as canonically conjugate variables [12]. In the present section we have performed measurements of these quantities in order to observe their oscillations in time, ensuring that our system undergoes the Josephson dynamics: in this case, particle transport within the junction occurs due to tunneling phenomena, as explained in Sec. 1.6. In order to investigate the evolution over time of the chemical potential difference, it is necessary to generate an initial non-zero $\Delta\mu$ imbalance, which allows for the establishment of the AC Josephson effect. The creation of the $\Delta\mu$ imbalance occurs by varying the parameters controlling the acusto-optical modulator that acts on the IPG laser beam, such that the centre of the optical dipole trap due to its crossing with the Mephisto laser is displaced: the repulsive optical potential of the DMD therefore acts on an atomic cloud which is not symmetrical with respect to the trap center. The net result is the creation of two ultracold atomic reservoirs with a different particle density, separated by a thin optical barrier located at the centre of the trap. In this measurement the first image loaded on the DMD has already the optical barrier in the center of the potential, so that we avoid diffusion phenomena of the atomic cloud between the two superfluid reservoirs: this process could in fact re-balance the initial $\Delta\mu$ created. With respect to the previously discussed case, reported in Sec. 2.2, where the barrier is adiabatically raised by gradually increasing Int_{th} in order to not excitate perturbations in the superfluid, this initial barrier is particularly deep, presenting a set $Int_{th} = 255$: this way tunneling phenomena are practically suppressed and the starting system effectively represents a density imbalanced junction. Meanwhile, the power of the trapping 532 nm laser is progressively increased from $P_{DMD} = 0\,\mathrm{mW}$ to a final value of $P_{DMD} = 125\,\mathrm{mW}$. Only at the end of this ramp the intensity of the barrier is abruptly set to a final value of $Int_{th} = 110$, and the system can evolve through tunneling processes. The created junction contains roughly $21 \cdot 10^3$ atoms, in a rectangular potential of size $125 \times 17.5\,\mu\mathrm{m}^2$. The optical barrier depth V_0 can be calculated through Eq. (2.21): its corresponding ratio with the chemical potential μ returns a value of about $V_0/\mu \sim 1.2$, ensuring that the Josephson dynamics is capable of setting in. An example of the chemical potential imbalanced Josephson junction created in our setup by following the described procedure is reported in Fig. 3.4.

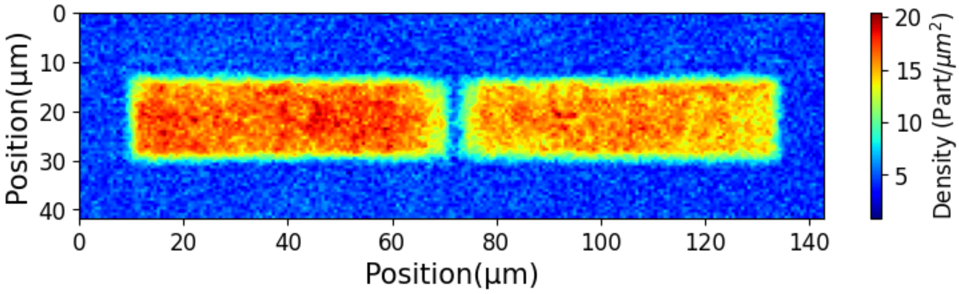

Figure 3.4: *Density imbalanced Josephson junction with a thin barrier in the centre, created by the DMD potential after displacing the optical dipole trap realized through the green laser: this is the configuration we probed for studying the coherent oscillations of $\Delta\mu$ and ϕ. The color scale on the right reports the cloud 2-D density $n(x,y)$. We notice a clear density accumulation on the left side of the junction, obtained with the procedure descripted in this section.*

After the creation of a junction presenting a non-zero $\Delta\mu$ between its superfluid reservoirs, the system is let to evolve freely without displacing the optical barrier, as we follow the time evolution of $\Delta\mu$ and ϕ by monitoring the *in-situ* density and the time-of-flight interference pattern during time, respectively. Using the absorption imaging technique the optical density OD of the atomic cloud is measured, as described in Sec. 2.1: the chemical potential difference $\Delta\mu$ can be successively calculated from Eq. (2.9), valid in the BEC case, once this quantity is known. As shown in Fig. 3.5, we observe density oscillations from one side to the other of the optical trap, which are damped in time due to resistive effects occurring during the motion of the atoms inside the cloud. The following equation is fitted to the $\Delta\mu - t$ experimental curve:

$$\Delta\mu(t) = off + A_0 \sin(2\pi\nu\, t + \phi) \cdot e^{(-t/\tau)} \tag{3.5}$$

where τ represents a characteristic damping time, while ν is the oscillation frequency and ϕ the associated phase shift. The corresponding curve fit (black line in Fig. 3.5) returns an oscillation frequency of $\nu = 18.07 \pm 0.07$ Hz. On the other hand, the interference profile, from which the relative phase ϕ between the condensates can be inferred, is obtained through the time of flight (TOF) technique already employed for the measurement of the phase

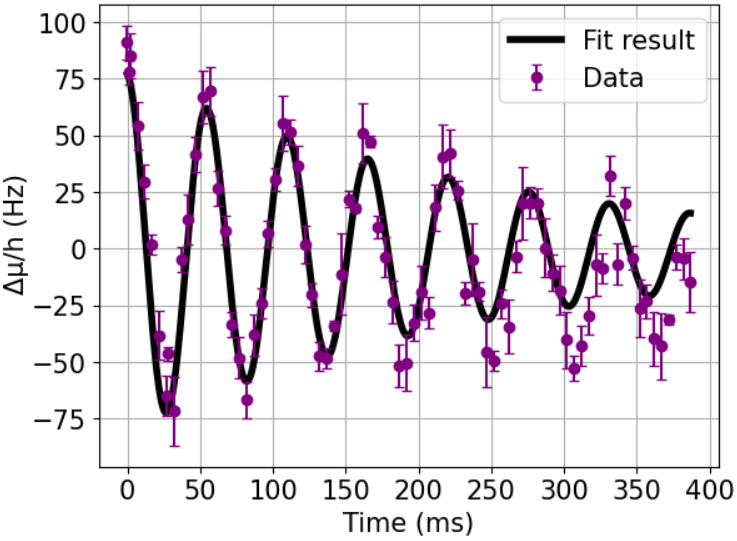

Figure 3.5: *Oscillations of $\Delta\mu$ inside the trap as a function of the time, occurring due to quantum tunneling effects. The time $t = 0$ corresponds to when the optical barrier is ramped down to $Int_{th} = 110$, and the system is able to evolve freely. Data is fitted with Eq. (3.5), where we extracted an oscillation frequency of $\nu = 18.07 \pm 0.07\, Hz$.*

during the barrier calibration, as shown in Sec. 2.4: in this procedure all optical traps are switched off, allowing for the interference of the two atomic clouds. The absorption imaging process is then effectuated after 3 ms with respect to the trap removal, in order to obtain the interference profile. The relative phase between the two reservoirs, ϕ, can be extrapolated by fitting the obtained interference patterns with Eq. (2.17), at different times with respect to the start of the Josephson dynamics, but always after a TOF of 3 ms. An example of such an interference pattern, together with its respective curve fit, is reported in Fig. 3.6.

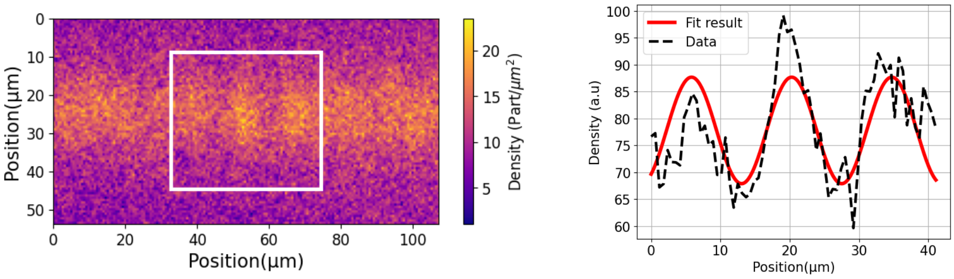

(a) Interference pattern

(b) Fit result

Figure 3.6: ***(a)**: On the left, the interference profile of the two superfluids after a 3 ms time of flight process, with the associated color-scale, reporting the 2-D density $n(x, y)$.*
***(b)**: On the right, the fit of such an interference pattern, effectuated with Eq. (2.17) on the integrated density along the y-axis as a function of the position, in the region surrounded by the white rectangle in Fig (a).*

The data for the relative phase as a function of the time $\phi(t)$ is reported in Fig. 3.7, and can be fitted with the following equation:

$$f(x) = A\,\sin\left(2\pi\nu\, t + \Phi\right) + off \tag{3.6}$$

in order to extract the frequency ν and the phase Φ of the oscillations.

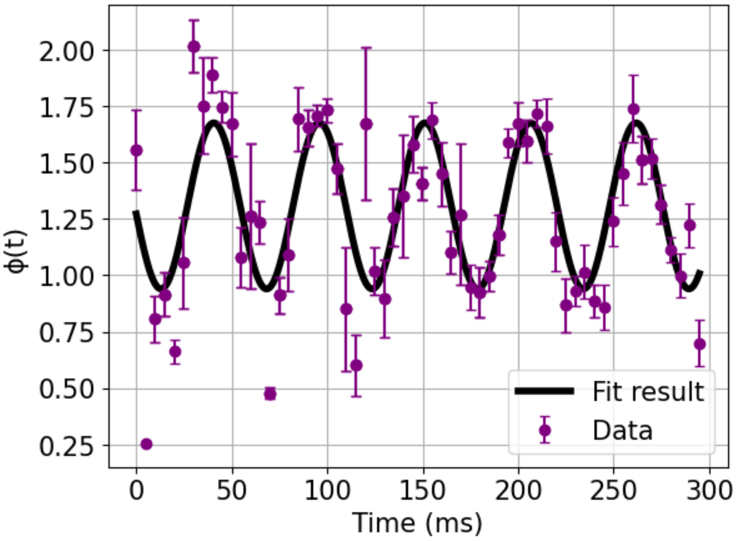

Figure 3.7: *Oscillations of the relative phase ϕ during time, obtained with a* 3 *ms TOF. Data is fitted with Eq. (3.6), where we extracted an oscillation frequency of* $\nu = 18.08 \pm 0.15$ *Hz. This value is compatible, within its errorbar, with the frequency found for the oscillations of* $\Delta\mu$ *in Figure (3.5), as predicted from the AC Josephson effect theory.*

The corresponding curve fit (black line in Fig. 3.7) returns an oscillation frequency of $\nu = 18.08 \pm 0.15$ Hz. As we can see from these results the extracted oscillation frequency, for both the relative phase ϕ (Fig. 3.7) and chemical potential difference $\Delta\mu$ (Fig. 3.5), has the same value of about $\nu \approx 18\,\mathrm{Hz}$, as expected. Moreover, the phase difference $\Delta\Phi$ between their oscillations in time is found to be $\Delta\Phi = \Phi_\phi - \Phi_{\Delta\mu} \approx (1.59 \pm 0.22)$ rad, compatible with the expected value of $\Delta\Phi = \pi/2$ within the experimental error bar. From these measurements we proved how the Josephson dynamics, predicted by Eqs. (1.88) and (1.90), is well reproduced inside our system, where the thin optical barrier produced by the DMD behaves as an effective Josephson barrier; therefore we can study the ultracold gas, trapped in the hybrid repulsive potential, in the framework of Josephson junctions. These results also show the conjugate nature of the relative phase ϕ and of the chemical potential difference $\Delta\mu$ between the superfluid reservoirs, representing a striking manifestation of the system's macroscopic quantum phase coherence. This is a consequence of the spontaneous symmetry breaking associated with the transition to superfluidity.

3.4 DC Josephson effect characterization

In the present section we investigate the DC Josephson effect in our particular experimental setup, where we have an elongated superfluid Josephson junction of ^{6}Li atoms in the BEC state of tightly-bound molecules, held together by weakly repulsive interactions, as explained in Sec 1.4. For barriers with sufficiently low transmission probability ($V_0/\mu > 1$ in superfluid junctions), where tunneling processes can be treated as perturbations, a sinusoidal current-phase relation is expected to hold, as reported in Eqs. 1.82 and 1.88. A current-biased ultracold Josephson junction can be realized by displacing the thin optical barrier within the trapping potential at a constant speed over time, as previously discussed in Sec. 3.2, generating an atomic current between the two superfluid reservoirs; if this movement occurs with a sufficiently small speed, with respect to a certain critical value v_c of the barrier's velocity, no finite difference in chemical potential develops as all the particles tunnel from one side of the barrier to the other. On the other hand, since at high barrier velocities dissipative phenomena set in, the tunneling of atoms occurs only partially, causing a density accumulation in the direction of the barrier's movement. This results in the creation of a non-zero $\Delta\mu$, which increases almost linearly while increasing the velocity of the barrier above its critical value v_c; we recall that, in solid-state Josephson junctions, the Ohm law $\Delta V = IR$ is retrieved when applying an external current I_{ext} such that $I_{ext} > I_c$, where I_c is the junction's critical current, as shown in Fig. 1.9. Moreover the Python program, which permits to set the desired barrier parameters as its initial position x_0 and velocity v_0, also allows for the tuning of hybrid potentials with different sizes $L_x \times L_y$ along the x-y plane. Therefore, it is possible to probe the system's response to an external current as its linear size changes: in Sec. 3.4.1 we investigated the transport properties of the junction by fixing the linear size L_y of the rectangle along the y-axis while we varied the system size L_x along the x-axis. The green laser's power $P_{DMD}(\text{mW})$ is kept constant during this part of the experiment, resulting in a fixed value of V_0/μ. We can also study the behavior of the system in the opposite case, changing the power of the trapping laser which generates the optical potential while not altering the junction's dimensions, as done in Sec. 3.4.2. In both cases, we will show how the measured critical current I_c and conductance G depend on these tunable parameters, adjustable from the outside, characterizing the Josephson DC dynamics within our experimental setup.

3.4.1 DC response for different size junctions

We want to study how the Josephson DC dynamics, triggered by a constant current, behaves for different horizontal sizes L_x, which is the dimension of the junction along the direction of the particle current, or, equivalently, along the barrier's movement. In particular, we will investigate the behavior of both the critical current I_c and the conductance G as a function of the horizontal length L_x, while fixing the vertical length at a value of $L_y = 17.5\,\mu\text{m}$: the particle density is always kept at a constant value of about $n \sim 13.6\,\text{Part}/\mu\text{m}^2$ between the various measurements such that all the different junctions present the same chemical potential μ. The power of the green laser ($\lambda = 532\,\text{nm}$) is also set at a constant value of $P_{DMD}(\text{mW}) = 135\,\text{mW}$ during this part of the experiment, resulting in a barrier depth, in frequency units, of about $V_0 \sim 1.6\,\mathrm{KHz}$ (see Sec. 2.4). Its corresponding ratio with the chemical potential μ is approximately $V_0/\mu \sim 1.1$ for all horizontal sizes investigated in this section, ensuring tunneling phenomena. Measurements are made as follows; after creating a superfluid Josephson junction in the hybrid box potential of Eq. (2.4), with the procedure described in Sec. 2.1, we make sure that the system's density is initially balanced before starting the dynamics, such that the difference of chemical potential $\Delta\mu$ between the two reservoirs is approximately zero at the beginning of the experiment. This process occurs via precise displacements of the final repulsive optical dipole trap, the latter realized through the green $532\,\mathrm{nm}$ laser which causes an harmonic confinement along the vertical direction; this is performed in order to change the position of the atomic cloud with respect to the center of the rectangular repulsive trap, realized with the DMD optical setup. These fine movements are made through the use of a pico-motor, which allows to displace the optical dipole trap along both the horizontal and vertical directions, of the desired amount of micro-steps. After this preliminary density balancing, the measurement starts by moving the thin optical barrier inside the junction with the desired speed v_0, for a time equal to t_{barr}, with the procedure explained in Sec. 3.2: this generates an atomic current in the opposite direction with respect to the barrier's motion. At the end of this displacement the absorption imaging process is performed, allowing to obtain the value of the optical density OD of the system, and, consequently, the value of the atomic 2-D density $n(x, y)$. Using the measured result for the atom density, the chemical potential difference $\Delta\mu$ corresponding to the velocity v_0 can be evaluated by using Eq. (2.9) from the number of atoms in the left and right reservoir. This process has to be repeated for different values of the barrier velocity v_0, in order to obtain the $\Delta\mu - v_0$ characteristic of the junction, while keeping the system's total size fixed. Next, we can set different values of the horizontal length L_x and perform the same measurements, in order to study the transport properties as a function of the system's size. The velocity v_0 set by terminal can be converted into a particle current I, since the latter represents a more significant physical quantity, by exploiting Eq. (3.3), where the number of atoms N is obtained by averaging the measured atom number over the many repetitions done at a fixed velocity. The obtained $\Delta\mu - I$ curves are then fitted with one of the circuital models introduced in Sec. 1.6, in order to extract the notable parameters that characterize our atomic junction: the critical current I_c and the conductance G, which have to be studied as a function of the system's size. We chose to fit the data with Eq. (1.94), which reports the stationary solution for the chemical potential difference $\Delta\mu$ (in the overdamped regime $\beta_c \ll 1$) that occurs when injecting a current (i.e. driving the optical barrier) for a sufficiently long time with respect to the transport dynamics: in what follows we will suppose to satisfy this assumption. Typical values for the total atom number inside the system are about $N \sim 10^4$ atoms, for a junction with an horizontal size of about $L_x = 50\,\mu\mathrm{m}$: these values correspond to an estimated critical particle current of order of $I_c \sim 1.5 \cdot 10^5\,\mathrm{Part/s}$. The measurement results, together with their corresponding curve fits, are reported in Fig. 3.8, for both driving times $t_{barr} = 10\,\mathrm{ms}$ and $t_{barr} = 5\,\mathrm{ms}$, at different values of the horizontal length L_x: we notice how the chosen fitting function well interpolates

Table 3.1: *Fit results for G and I_c with their relative error bars, obtained by fitting Eq. (1.94) to experimental data, as shown in Fig. (3.8).*

L_x (μm)	t_{barr} (ms)	$G \cdot h$	I_c (10^5 Part/s)	v_c (mm/s)
50	10	584 ± 55	2.08 ± 0.05	0.99 ± 0.03
75	10	749 ± 38	2.05 ± 0.04	0.99 ± 0.02
100	10	854 ± 51	2.14 ± 0.06	1.09 ± 0.03
50	5	1001 ± 68	2.09 ± 0.12	0.99 ± 0.04
75	5	1586 ± 67	2.48 ± 0.02	1.21 ± 0.01
100	5	1658 ± 73	2.33 ± 0.06	1.17 ± 0.03

the experimental data. We also report in Fig. 3.9 the 1-D integrated density plot, which shows the establishment of a density imbalance in the compressed reservoir as the displacement velocity of the barrier is increased. In particular, we observe a noticeable density accumulation on the left side of the junction after the critical velocity v_c (white dashed line) is overcome. Fit results for the extrapolated values of the conductance G and the critical current I_c are reported in Fig. 3.10 and in Tab. 3.1. For both driving times t_{barr}, the conductance increases monotonically with the system size, showing a reduction in the resistive behavior, while the critical current stays approximately constant as the horizontal length is varied: this is expected because the junction's density profile is homogeneous in the x-y plane, depending only on the trapping laser power P_{DMD}(mW), regardless of the dimension of the trap. As a consequence,

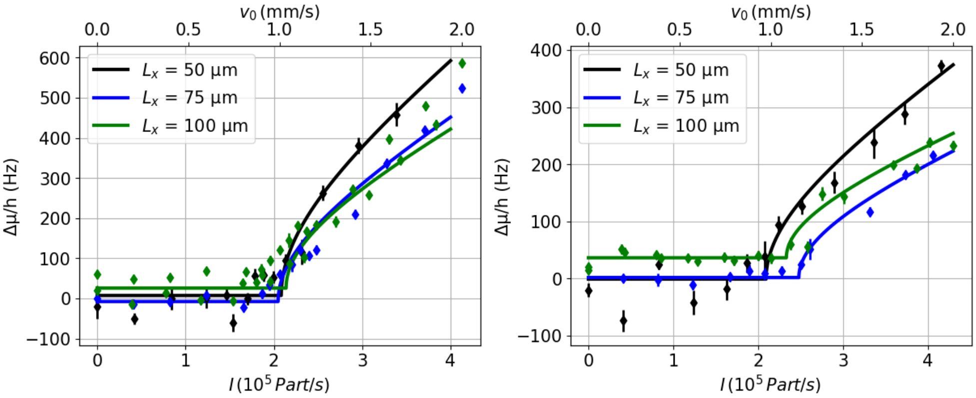

(a) $t_{barr} = 10\,\mathrm{ms}$ **(b)** $t_{barr} = 5\,\mathrm{ms}$

Figure 3.8: *Measured $\Delta\mu$-I characteristic, for different junction sizes and driving times: Fig. (a) reports $t_{barr} = 10\,ms$, while Fig. (b) shows $t_{barr} = 5\,ms$. Data is fitted with Eq. (1.94) (solid lines). The different colors correspond to different horizontal lengths L_x of the junction, expressed in μm, as shown in the plots legend. Along the upper x-axis we report the values of the barrier velocity which correspond to the particle current I. In both panels, the measurements corresponding to different system sizes $\{50, 75, 100\}$ μm are respectively shifted on the vertical axis by $\{-20, 0, 20\}$ Hz, in order to increase visibility.*

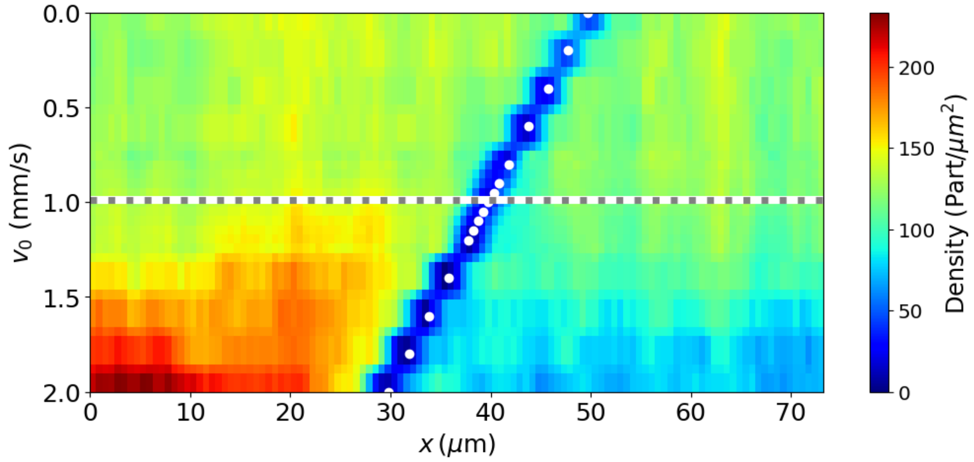

Figure 3.9: *1-D density profile, showing the integrated particle density along the y-axis as a function of the barrier's velocity (y-axis). The corresponding color bar is reported on the right. We note that, for high barrier velocities ($v \gtrsim v_c$), a density accumulation sets in along the direction of the barrier's displacement. White dots correspond to the position of the barrier's center during time, calculated through Eq. (3.4), while the dashed horizontal line represents the critical velocity $v_c = (0.99 \pm 0.02)$ mm/s, obtained by fitting Eq. (1.94).*

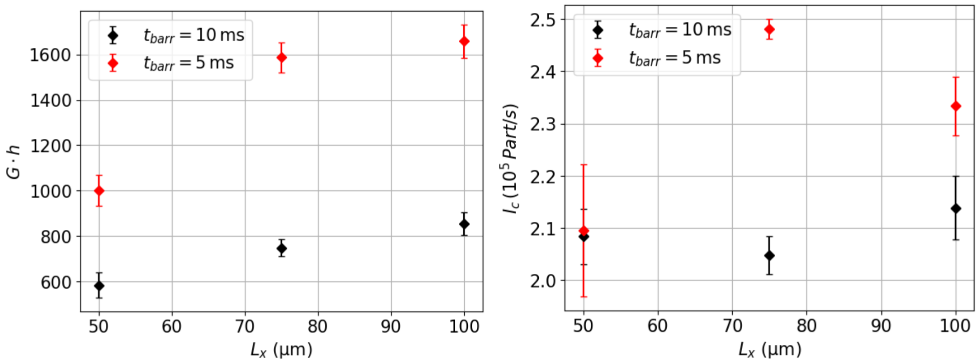

(a) $G \cdot h$ *vs* L_x. **(b)** I_c *vs* L_x.

Figure 3.10: *Fit results for the various DC Josephson effect measurements: in panel (a) we report the extracted values of G, while I_c is reported in panel (b). Both of these quantities are plotted a function of the horizontal length L_x. When the system's size is increased we observe a monotonic increasing behavior for G, while I_c is approximately unaffected. These results are true for both driving times $t_{barr} = 10$ ms and $t_{barr} = 5$ ms.*

the critical current I_c, which depends only on the density of the cloud (together with the condensed fraction N_0/N and the interaction parameter $1/k_F a$, as shown in Ref. [19]), should be independent on the system size. Moreover, the conductance G is found to be higher for the smaller driving time $t_{barr} = 5$ ms, as the chemical potential difference $\Delta\mu$ saturates to a lower value with respect to the $t_{barr} = 10\,\text{ms}$ case, where the barrier is driven for a longer time: in fact, lower values of the final $\Delta\mu$ correspond to less-resistive systems, which should present an higher conductance. The dependence of the conductance on the driving time, related to how information propagates in our system (that is, at the speed of sound c_s), is discussed more deeply in Sec. 4.3. The critical velocity of the barrier's displacement, reported in Tab. 3.1, is a fraction of the measured speed of sound c_s, for the same experimental conditions: the latter quantity represents the Landau critical velocity for superfluidity in the case of Bose-Einstein condensates, as discussed in Sec. 1.5. Actually, when the DC Josephson effect sets in and a finite $\Delta\mu$ develops, the driving velocity v_0 of the optical barrier overcomes the local speed of sound near the barrier itself, and excitations are created as Landau's criterion is violated. The local value of the speed of sound is lower than its bulk value c_s, measured in Sec. 3.1, as the density of the cloud near the barrier region is lower and the speed of sound depends on the superfluid density n, as $c_s \propto \sqrt{n}$: this scaling as a function of the particle density is due to the presence of the chemical potential μ in Eq. (2.13), which reports the expression for the speed of sound in the BEC regime.

3.4.2 Different barrier velocity junction

We now investigate the transport properties of our superfluid junction as we change the power of the green laser which realizes the trapping, $P_{DMD}(\text{mW})$, while we keep unaltered the system size: the horizontal length is here fixed at a value of about $L_x = 50\,\mu\text{m}$, while $L_y = 17.5\,\mu\text{m}$. The process to collect the experimental data is exactly the same described for the previous case of a junction with variable length L_x, where the optical barrier is displaced within the junction at a certain constant velocity v_0. We report in Fig. 3.11 the collected $\Delta\mu - I$ data, together with its corresponding fit carried out via Eq. (1.94); again, the chosen fitting function nicely interpolates the experimental data.
We notice that the critical current of the junction I_c occurs at lower values for increasing power $P_{DMD}(\text{mW})$ of the green laser. This is caused by the fact that increasing the power of the laser also increases the depth of the trap, and tunneling phenomena are gradually suppressed (while V_0/μ increases). The critical current I_c subsequently decreases, since its value depends on the tunneling amplitude $|t|$ as $I_c \sim |t|$, as shown in Ref. [19]; the critical velocity v_c of the barrier, at which tunneling processes are not sufficient to cause the passage of all atoms from one side to the other, decreases accordingly. Therefore, for

Table 3.2: *Fit results for G and I_c with their relative error bars, obtained by fitting Eq. (1.94) to experimental data, as shown in Fig. 3.11.*

$P_{DMD}(\text{mW})$	$G \cdot h$	$I_c\,(10^5\,\text{Part/s})$	$v_c\,(\text{mm/s})$	V_0/μ
135	590 ± 93	2.08 ± 0.05	0.99 ± 0.02	1.1
200	394 ± 23	0.73 ± 0.04	0.37 ± 0.02	1.6
300	284 ± 19	0.16 ± 0.04	0.09 ± 0.02	2.4
400	260 ± 15	0.04 ± 0.008	0.024 ± 0.05	3.3

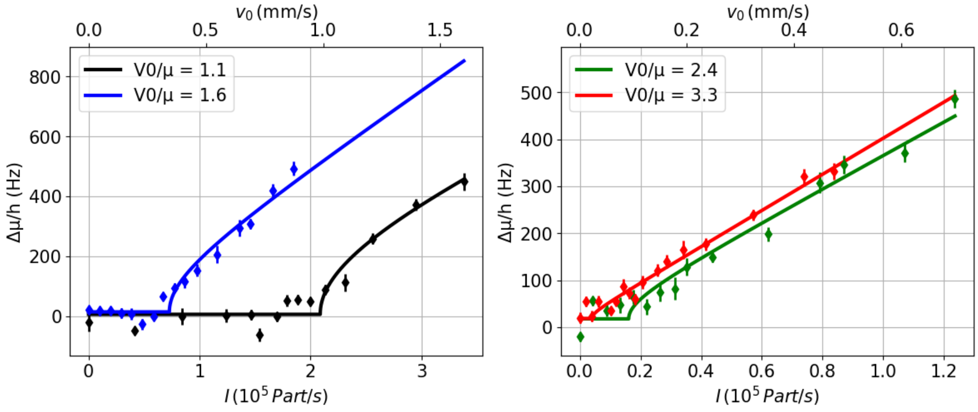

(a) $G_{Barr}(mW) = 135,\ 200\,mW$. **(b)** $G_{Barr}(mW) = 300,\ 400\,mW$.

Figure 3.11: *Measurements of the* $\Delta\mu - I$ *characteristic for different* V_0/μ *ratios, together with their corresponding curve fits (solid lines) done via Eq. (1.94). The chemical potential difference* $\Delta\mu$ *is reported in frequency units* ($\Delta\mu/\hbar$)*. Different colors correspond to different* V_0/μ *ratios, as shown in the figure's legends. In both panels (a) and (b), measurements are shifted by* $\{-20, +20\}$ *Hz along the vertical direction, in order to increase visibility.*

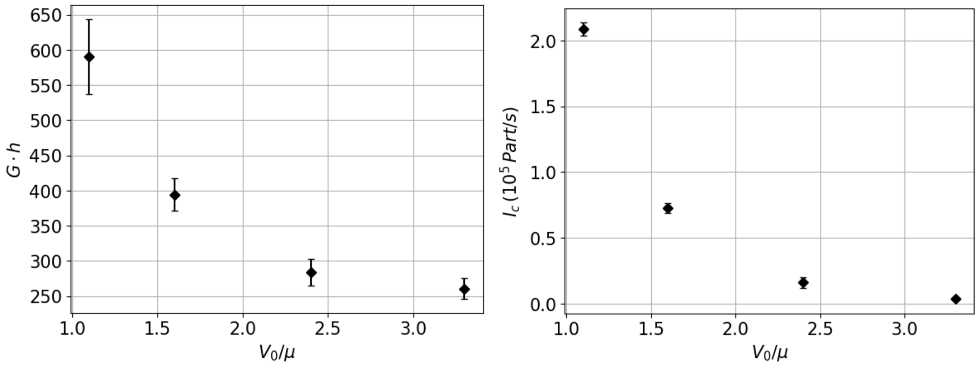

(a) $G \cdot h$ vs V_0/μ. **(b)** I_c vs V_0/μ.

Figure 3.12: *Fit results for the DC Josephson effect measurements, reporting the extracted values of* G *and* I_c *as a function of the* V_0/μ *ratio; we clearly observe a monotonic decrease for both quantities while increasing the trap depth* V_0*, which is directly proportional to the applied laser power* $P_{DMD}(mW)$*, as reported in Eq. (2.21).*

very deep barriers (corresponding to high laser intensities) a small displacement velocity is enough to cause density accumulations along the direction of the barrier's movement, in the compressed reservoir. This ultimately generates a finite chemical potential difference $\Delta\mu \neq 0$, even when low currents are applied. We report in Fig. 3.12 and in Tab. 3.2 the results of the fit of the $\Delta\mu - I$ characteristics, as a function of the applied laser power P_{DMD}(mW). These results confirm the observation we just made, as the critical current I_c is a monotonous decreasing function of the laser power, and, therefore, of the barrier depth V_0. The same is true for the conductance G, which shows the same behavior of the critical current, as a function of the laser intensity. Again, this occurs because for higher trapping intensities the system becomes more resistive as tunneling processes become less relevant; in particular, the conductance depends on the tunneling amplitude as $G \sim |t|^2$, as shown in Refs. [40] and [48]. Therefore, the junction's conductance G has to decrease, resulting in an increasing resistance $R = G^{-1}$.

3.5 AC Josephson effect characterization

In the present section we will investigate more thoroughly the AC Josephson effect, introduced in Sec. 1.6 and probed in Sec. 3.3, by characterizing the Josephson oscillation modes as a function of the trapping parameters. In superconducting Josephson junctions, the application of an initial ΔV at the sides of the device generates an alternating current $I(t)$, which flows inside the junction and is driven solely by the relative phase difference ϕ: by integrating Eq. (1.83), we obtain that the phase difference between the order parameters evolves over time as $\phi(t) = \Delta V_0 \sin(\omega_J t)$, oscillating at the plasma frequency ω_J. When considering a superfluid Josephson junction, an initial imbalance of $\Delta\mu$ between the two reservoirs induces a time evolution of the relative phase similar to that of the superconductive case, $\phi(t) \sim \sin(\omega_J t)$. By inserting this expression for the phase difference inside Eq. (1.88), we obtain that inside the atomic Josephson junction an alternating particle current flows, as in the superconductive case. In this regime, the chemical potential difference $\Delta\mu$ oscillates in time between the two reservoirs, $\Delta\mu(t) \sim \cos(\omega_J t)$, at a frequency still given by the plasma frequency ω_J, reported in Eq. (1.87); this process ultimately corresponds to coherent density oscillations within the junction, as those measured in Sec. 3.3. When the density imbalanced junction presents a large enough initial $\Delta\mu$, density pulses are expected to propagate within the junction at the speed of sound c_s in finite size systems: we therefore expect the Josephson oscillations phenomena, occurring at the plasma frequency ω_J, to mix with the sound excitations. We investigate density oscillations within the junction by measuring their corresponding frequency ω_J, in two different ways:

1. The first method, as mentioned above, consists in creating a certain non-zero chemical potential difference, $\Delta\mu \neq 0$ between the two reservoirs constituting the junction. The system is then allowed to evolve, keeping the barrier in the center of the junction without moving it: tunneling phenomena will set in causing density oscillations, and it is possible to image the junction at different times in order to obtain the temporal evolution of the density ($\Delta\mu$-t curves). We probe these oscillations as done before with the DC Josephson effect, by varying the system size and the intensity of the optical barrier. This is reported in Sec. 3.5.1.

2. Another technique for probing the AC Josephson effect in our system consists in exciting a density pulse, which propagates at the speed of sound c_s within the junction. This is done by compressing one side of the optical potential, with the same modality discussed in Sec. 3.1, where we excited sound modes. If a thin barrier is present inside the junction

Josephson, separating two independent superfluid reservoirs, oscillations of the cloud's density should be observed, roughly at the sound modes frequency $\nu_s = c_s/2L_x$. We will compare these oscillations with the Josephson oscillations reported in Sec. 3.5.1, which occur due to a finite initial $\Delta\mu$ that trigger the tunneling dynamics. This measurement is shown in Sec. 3.5.2, and the results we obtain suggest the existence of a coupling mechanism between the Josephson oscillation frequency $\nu_J = \omega_J/2\pi$ and the frequency of the sound modes ν_s.

3.5.1 Oscillations with $\Delta\mu$ imbalance

In order to generate a starting non-zero $\Delta\mu$ within the superfluid Josephson junction, we proceed as described in Sec. 3.3, displacing the optical dipole trap center first while successively ramping up the trapping potential. The optical barrier is subsequently lowered, leading to the creation of a density imbalanced junction where atom pairs can tunnel through, and the system begins to effectuate density oscillations between the two sides of the device.

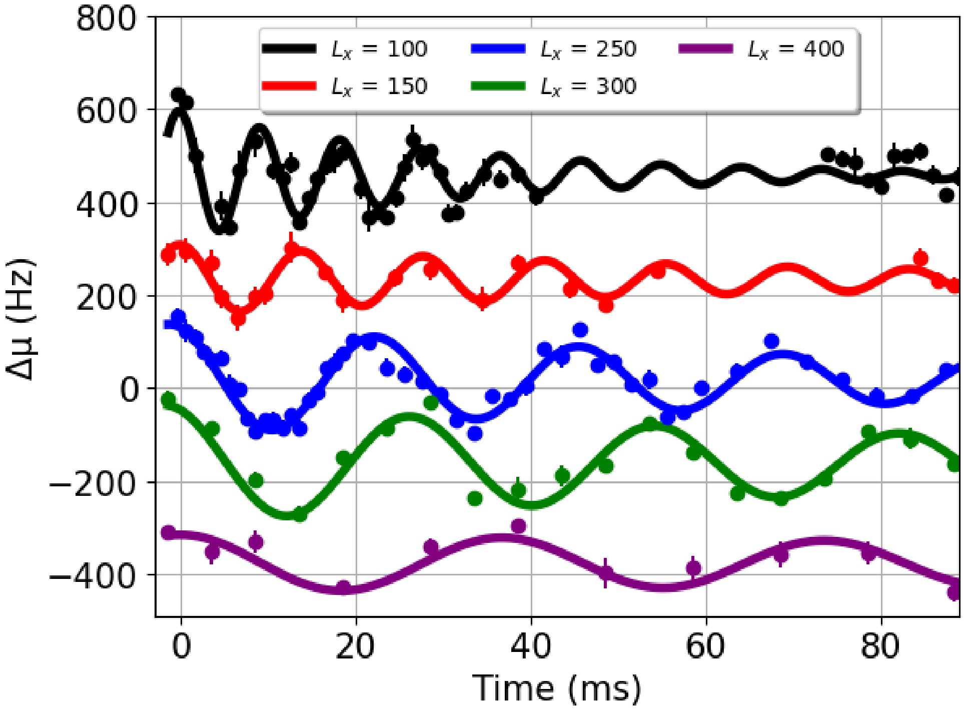

Figure 3.13: *Measurement results of the $\Delta\mu(t)$ oscillations, obtained in the AC Josephson effect measurements for different horizontal lengths L_x. Data is fitted through Eq. (3.7). The laser power is fixed to a value of $P_{DMD} = 135\,mW$, corresponding to a ratio of $V_0/\mu \sim 1.1$. We clearly see that for higher system sizes the period T of the oscillations increases, resulting in a smaller frequency ν_J. Plot are respectively shifted from the measured values along the y-axis, in decreasing order from the vertical, by $\{400, 200, 0, -200, -400\}$ Hz, in order to increase visibility.*

To extract the $\Delta\mu$-t curves we carry out the absorption imaging process *in* *situ* at different times, in order to calculate the chemical potential imbalance within the junction. During measurements the trapping parameters, namely the junction horizontal size L_x and the power $P_{DMD}(\mathrm{mW})$ of the green laser realizing the optical trap, can be set as desired: therefore, Josephson oscillations can be studied as a function of these quantities. We report in Fig 3.13 the experimental results for Josephson oscillations occurring for different system size, with an applied laser power of $P_{DMD}(\mathrm{mW}) = 135\,\mathrm{mW}$, the corresponding trap depth to chemical potential ratio being of about $V_0/\mu \sim 1.1$: this data is fitted with a damped periodic function, chosen as follows:

$$\Delta\mu(t) = off + A_0 \cos\left(2\pi\nu\, t + \phi_0\right) \cdot e^{(-t/\tau)} \tag{3.7}$$

where A_0 is the amplitude of the oscillations, ν is the oscillation frequency, τ is the time scale associated with the damping of $\Delta\mu$ over time, while ϕ_0 is a phase factor. The results of the fit for the oscillation frequency ν, as a function of L_x and of $P_{DMD}(\mathrm{mW})$, are shown in Fig 3.14 and in Tab. 3.3. We can see how the measured frequency ν of the Josephson oscillations decreases monotonously as the size of the system increases, with an approximately hyperbolic dependence of the type $\nu \propto 1/L_x$. This scaling property is shown in Fig. 3.14 along with curve fits, which corroborate the latter observation as the data well matches the fitting function $\nu = off + \nu_0/L_x$, where ν_0 is a fixed amplitude. The same monotonic decreasing behavior of the frequency is found when increasing the power of the trapping laser $P_{DMD}(\mathrm{mW})$, and consequently, when increasing V_0 with respect to μ. This phenomena is shown in Ref. [41], where, in the framework of a LCSJ model the Josephson inductance L_J is shown to increase when increasing the barrier's depth, resulting in a decrease of the oscillation plasma

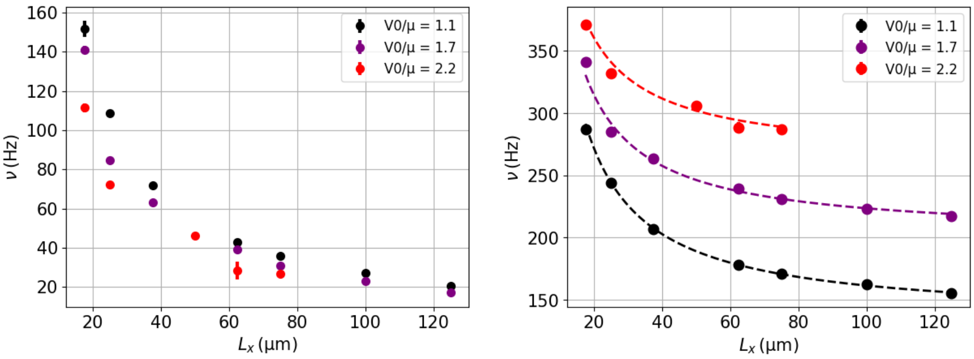

(a) Fit result for ν

(b) ν vs L_x hyperbole fits

Figure 3.14: *(a): Fit results of ν curves, extracted from the measured $\Delta\mu(t)$ curves by fitting Eq. (3.7). The frequency ν_J decreases as the system size is increased.*
(b): Fit of the experimental results with a function of the type $f(x) = off + \nu_0/L_x$, reported as a dashed line in the plot: in our setup the frequency ν_J seems to have an approximately hyperbolic dependence on the system's size. Plot are respectively shifted from the measured values along the y-axis, in decreasing order from the vertical, by $\{260, 200, 135\}$ Hz, in order to increase visibility.

P_{DMD} :	135 mW
V_0/μ :	1.1
$L_x(\mu\text{m})$	$\nu(\text{Hz})$
17.5	152 ± 4
25	109 ± 1
37.5	72 ± 1
50	N.M
62.5	42.7 ± 0.2
75	35.7 ± 0.3
100	27.1 ± 0.6
125	20.3 ± 0.3

P_{DMD} :	200 mW
V_0/μ :	1.7
$L_x(\mu\text{m})$	$\nu(\text{Hz})$
17.5	141 ± 2
25	84.6 ± 0.8
37.5	63 ± 1.3
50	N.M
62.5	39.3 ± 0.4
75	30.8 ± 0.9
100	23.2 ± 1.2
125	17.2 ± 0.4

P_{DMD} :	260 mW
V_0/μ :	2.2
$L_x(\mu\text{m})$	$\nu(\text{Hz})$
17.5	111.4 ± 2.2
25	72.1 ± 1.4
37.5	N.M
50	46.2 ± 0.4
62.5	28.4 ± 4.5
75	26.8 ± 0.4
100	N.M
125	N.M

Table 3.3: *Fit results for ν, obtained by fitting Eq. (3.7) to experimental data curves of $\Delta\mu$ as a function of t, as done in Fig. 3.14.*

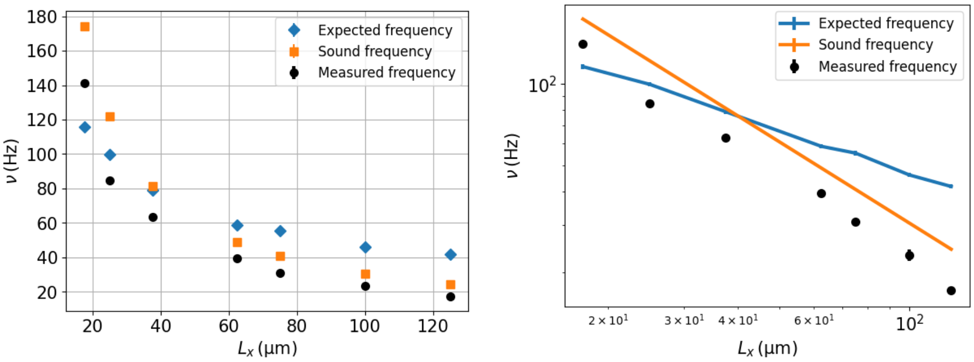

(a) Measured ν, expected ν_j and ν_s

(b) Logarithmic scale plot

Figure 3.15: ***(a)**: Fit results of ν curves (black dots), reported together with the values of $\nu_s = c_s/2L_x$ (orange dots), for the sound modes frequencies (blue dots), and the expected values of the plasma frequency $\nu_j = \sqrt{E_C E_J}/h$. We observe that for increasing system size the measured frequency becomes more compatible with the sound frequency.*
***(b)**: On the right, we report a plot which shows these results in a logarithmic scale. Here we can see how the slope of the curve describing the measured frequency changes as we increase the system size. For small sizes, it is compatible with the slope of the calculated plasma frequency ν_J (blue solid line), while for high values of L_x it seems almost parallel with the sound frequency curve (orange solid line).*

frequency ω_J: this is compatible with the expected behavior of the frequency in such a model, $\omega_J = 1/\sqrt{(L_B + L_J)C}$, where L_B and L_J represent the bulk and the Josephson inductance respectively. We also report in Fig. 3.15 (a) the obtained results for the speed of sound frequency $\nu_s = c_s/2L_x$ (orange dots) and the expected plasma frequency $\nu_J = \sqrt{E_C E_J}/h$ (blue dots), compared with the measured Josephson oscillation frequency (black dots), for the measurements with $P_{DMD} = 200\,\mathrm{mW}$; a plot in log-log scale is also reported by side in Fig. 3.15 (b), in order to highlight the different scaling powers with respect to the system's size of the various frequencies. The value of the charging energy E_C (required to calculate the plasma frequency ω_J) is found through Eq. (1.102), while the Josephson tunneling energy $E_J = \hbar I_c$ has to be calculated in the hypothesis that I_c stays constant if the laser intensity is kept fixed while varying the system's longitudinal length L_x. This was shown to be true in the analysis effectuated in Sec. 3.4: we therefore take the measured value of $I_c = (2.08 \pm 0.05) \cdot 10^5$ Part/s for the considered case of $P_{DMD} = 135\,\mathrm{mW}$, the former being reported in Tab. 3.2. In the AC Josephson regime we expect these $\Delta\mu$ oscillations in time to occur at the plasma frequency ω_J, as predicted by the Josephson-Anderson Eqs. (1.88) and (1.90). The discrepancy between the measured value of the oscillation frequency and the predicted value ν_J, observed in Fig. 3.15, may arise because of dissipative mechanisms during the density propagation inside the cloud and through the optical barrier, which could decrease the frequency of oscillation. For high values of the horizontal length L_x some kind of coupling mechanism between the coherent Josephson oscillations and the sound modes seems to exist: this could change the scaling of the oscillation frequency ν with respect to L_x. This phenomena may happen because the two-mode model, which predicts the expression of the plasma frequency reported in Eq. (1.101), is valid only for point-like systems [61]; the more we increase the system size, the more we are likely to stray from this assumption. A more detailed discussion of this intrinsic coupling between Josephson oscillation modes and sound modes in elongated bosonic Josephson junctions is found in Ref. [62].

3.5.2 Oscillations with sound waves

In this section we want to confirm that the dynamics of the Josephson oscillations observed in our system, which should be characterized by the plasma frequency ω_J, becomes gradually more intertwined with the phenomena of sound excitations as the system's linear size L_x is increased. The measurement is effectuated as follows: one side of the junction is quickly compressed, to be then returned to its initial condition. This process, as already discussed in Sec. 3.1, generates a sound wave that propagates within the superfluid at a speed equal to c_s. In the present case, the thin Josephson barrier in the middle of the junction causes the AC Josephson dynamics to occur, where the density imbalance generated within the cloud starts oscillating between the two reservoirs.

Table 3.4: *Fit results for ν, obtained by fitting Eq. (3.7) to experimental data, as done in Fig. 3.16.*

P_{DMD}(mW)	V_0/μ	ν (Hz)
70	0.6	38.0 ± 0.2
135	1.1	36.6 ± 0.2
898 200	1.6	32.2 ± 0.2

Measurements are taken by fixing the side of the junction $L_x = 75\,\mathrm{nm}$, while varying the intensity P_{DMD}(mW) of the DMD trapping laser. Fit curves are reported in Fig. 3.16, while fit results for the frequency ν as a function of the applied laser power are reported in Tab. 3.4.

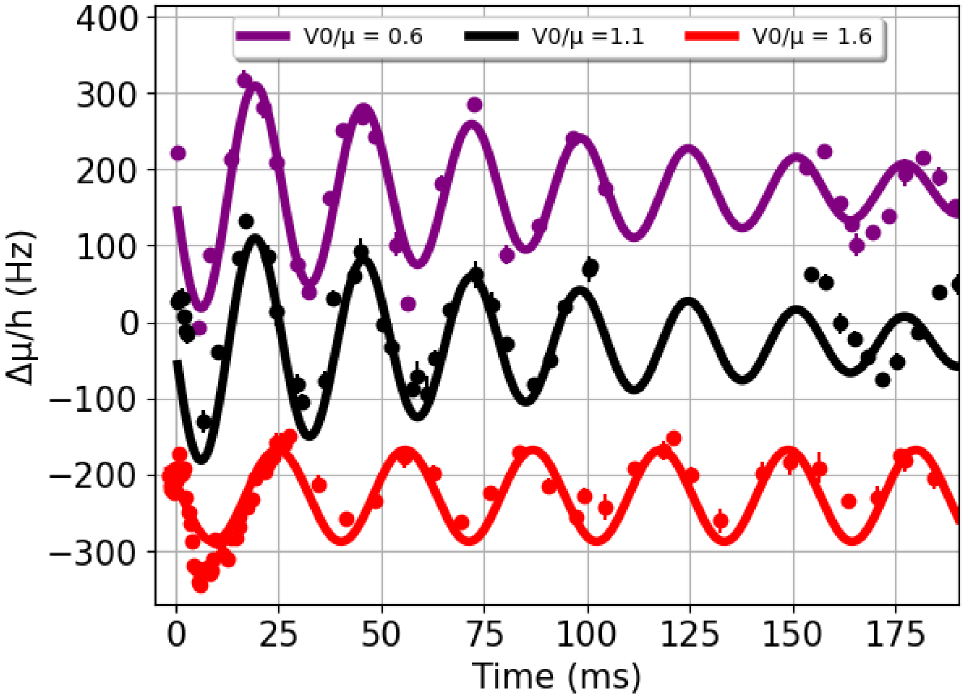

Figure 3.16: *Measurements of the $\Delta\mu(t)$ oscillations for different V_0/μ ratios, together with their corresponding curve fits, obtained by fitting Eq. (3.7), for the case of a sound-wave excitation. Plot are respectively shifted from the measured values, in decreasing order from the vertical, by $\{200, 0, -200\}$ Hz, in order to increase visibility. We observe how in the red curve ($V_0/\mu \sim 1.6$) the initial part (before ~ 10 ms) is clearly not sinusoidal: this is probably related to the fact that the corresponding speed pulse is very small at the beginning of the dynamics, and the crossing of the optical barrier through tunneling effects changes the curve's behavior, which then oscillates as a sine.*

This results are comparable with the measured Josephson oscillation frequencies at the same experimental conditions, being $L_x = 75\,\mathrm{nm}$ and identical P_{DMD}(mW), reported in Tab. 3.3; this again suggests that for long junctions the Josephson oscillations of $\Delta\mu$ may experience a coupling with the sound modes, propagating at a speed of c_s inside the cloud. We also report in Fig. 3.17 the 1-D density profile of the AC Josephson effect measurement with $L_x = 62.5\,\mu\mathrm{m}$ and $P_{DMD} = 135\,\mathrm{mW}$ (reported in Fig. 3.13 and Tab. 3.3), integrated along the y-axis, as a function of both the time (vertical axis) and the position (horizontal axis). We clearly see the propagation in time of a density pulse inside the optical potential, tunneling through the barrier and moving at approximately the speed of sound c_s.

The latter statement can be verified by plotting two straight lines $f(t) = c_s t + x_0$ (white dots), having angular coefficient equal to the measured speed

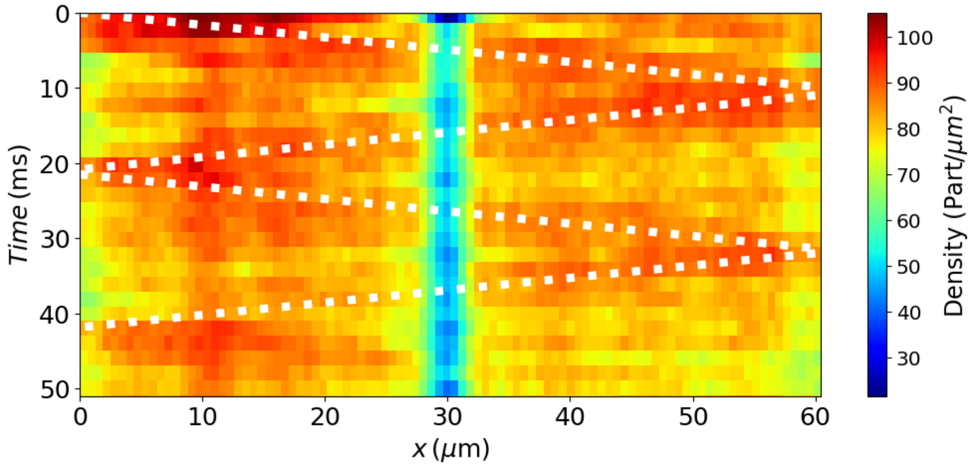

Figure 3.17: *1-D density profile (of the measurement having $L_x = 62.5\,\mu m$ and $P_{DMD} = 135\,mW$) as a function of the time t, taken with respect to the start of the oscillation dynamics. We notice the propagation of a density pulse from the left side to the right side of the junction, tunneling through the optical barrier. Two straight lines, having angular coefficient equal to the measured speed of sound c_s, are plotted above the experimental density profile (dotted lines), in order to corroborate our claims regarding the propagation of density pulses at the speed of sound c_s.*

of sound $c_s \sim 6.09\,\text{mm/s}$, reported in Sec. 3.1: these lines overlap compatibly with the underlying density pulses, confirming that the density oscillations which occur during the AC Josephson effect propagate at the speed of sound c_s inside our system.

Chapter 4

Shapiro steps in the ^{6}Li atomic Josephson junction

In the present chapter we will report the experimental results relating to the main physical phenomena investigated in this thesis: the emergence of **Shapiro steps** in the $\Delta\mu - I$ curves, characterizing the transport response of our superfluid Josephson junction when an alternating current $I(t)$ is injected inside the system, as discussed in Sec. 1.6.4 for the particular case of a superconducting junction. The mechanism underlying their occurrence can be understood in the framework of the tilted washboard potential $U(\phi)$, introduced in Eq. (1.98), where we expect a Shapiro step to occur whenever the relative phase ϕ jumps between n nearby local minima of the potential curve, undergoing *phase-slip* processes and changing its value by $2\pi n$. This last chapter is organized as follows: first and foremost, in Sec. 4.1 we explain how an alternating current $I(t) \propto I_{AC} \cos(2\pi\nu t)$, oscillating at a certain frequency ν, can be experimentally generated inside our atomic Josephson junction with the DMD optical setup. This will extend the treatment given in Sec. 3.2, describing the process behind the creation of a direct current I_{DC}, which involves the displacement of the thin barrier at a constant speed v_0 inside the optical potential. Time evolution measurements of the chemical potential imbalance $\Delta\mu$ for the case of an applied oscillating current, carried out both during and after the barrier dynamics (i.e, the current's injection), are reported in Sec. 4.2. In particular, AC Josephson oscillations are observed when the system is let to evolve freely after the barrier's movement: these oscillations occur at the same frequency reported in Sec. 3.5, for the same experimental conditions. Measurements of the $\Delta\mu - I$ characteristic associated with alternating current-biased atomic Josephson junctions, carried out through a periodic displacement of the optical barrier within the system, are reported in Sec. (4.3), leading to the observation of Shapiro steps: data is collected for different values of the driving frequency ν and of the driving amplitude x_1. Noteworthy quantities, namely the i-th step height $\Delta\mu_{S_i}$ and the i-th step position I_{S_i}, can be extracted by fitting to experimental data an opportune phenomenological function $f(I)$: the main objective is to compare the measured step height $\Delta\mu_S$ with its expected value, reported in Eq. (1.6.4), which predicts that this quantity should depend only on the modulation frequency ν and on the number n of relative phase jumps, occurring between different local minima of the tilted washboard potential. The emergence of *quantized vortices* in our experimental system is analyzed in Sec. 4.4: here we measure that phase slippage processes, which lead to the emergence of Shapiro steps, occur together with the nucleation of vortex dipoles within the superfluid. Therefore, we expect vortex excitations and Shapiro dynamics to be intertwined in our atomic Josephson junction. The former statement is supported by investigating the behavior of the vortex number N_{vort} as a function of the driving velocity v_0 of the barrier, and by comparing the obtained results with the respective $\Delta\mu - v_0$ curve. Finally, in Sec. 4.5 we showcase the measurement of the $\Delta\mu - I$ characteristic within a Josephson junction in the strongly interacting regime (UFG) of the BEC-BCS crossover, described in Sec. 1.4. When driving the optical barrier with a modulated trajectory $x(t)$ (or, equivalently, by injecting an alternating current) we expect to observe Shapiro steps also in this interaction regime, occurring with the same modality already discussed for the BEC case.

4.1 Alternate currents in isolated atomic junctions

As explained in Sec. 1.6.4, the application of an alternating atomic current $I(t) \sim I_{AC} \sin(2\pi\nu t)$ inside the system is necessary in order to probe the emergence of Shapiro steps, which arise due to a resonance between the velocity of the relative phase $\partial\phi/\partial t$ and the modulation frequency ν. In Sec. 3.2 we discussed how to generate a direct atomic current I_{DC} in our experiment; the optical barrier is displaced at a constant speed inside the superfluid ^{6}Li junction, allowing to investigate the DC Josephson dynamics. This is operatively done by loading a certain sequence of images onto the DMD that can be shifted via a series of equally time-spaced triggers. Our experimental setup allows to investigate the system more thoroughly: we can in fact not only apply a direct atomic current I_{DC}, but also an alternating atomic current $I(t)$ whose value oscillates in time at a given frequency. The procedure which we employ to generate a modulated current is exactly the same described for the DC case, where we can set the value of a certain number of parameters associated with the barrier's movement. When injecting an alternating current $I(t)$, the equation of motion of the barrier is described by:

$$x(t) = x_0 + v_0\, t + x_{osc}(t) = x_0 + v_0\, t + x_1\, \sin(2\pi\nu\, t) \tag{4.1}$$

so that we can also adjust the initial position of the barrier x_0 and its initial velocity v_0, together with the amplitude x_1 and the frequency ν of the oscillating modulation $x_{osc}(t)$. The velocity associated with the barrier's motion can be calculated by differentiating Eq. (4.1) with respect to time:

$$v(t) = \frac{dx(t)}{dt} = v_0 + v_{osc}(t) = v_0 + 2\pi\,\nu\, x_1\, \cos(2\pi\nu\, t) \tag{4.2}$$

so that the velocity of the barrier is made up by two contributions: a constant velocity term v_0 and an alternate velocity term $v_{osc}(t)$, which oscillates at a frequency ν and with an amplitude of $v_1 = 2\pi\,\nu\, x_1$. We report in Fig. 4.1 the plots of Eq. (4.1) and Eq. (4.2), effectuated for different values of experimentally feasible parameters x_1 ($\sim \{0, 5\}\,\mu$m), ν ($\sim \{70, 280\}$ Hz) and v_0 ($\sim \{0, 2\}$ mm/s). By combining Eq. (4.2). and Eq. (3.3), we obtain the expression for the injected current in the AC case as a function of the motion

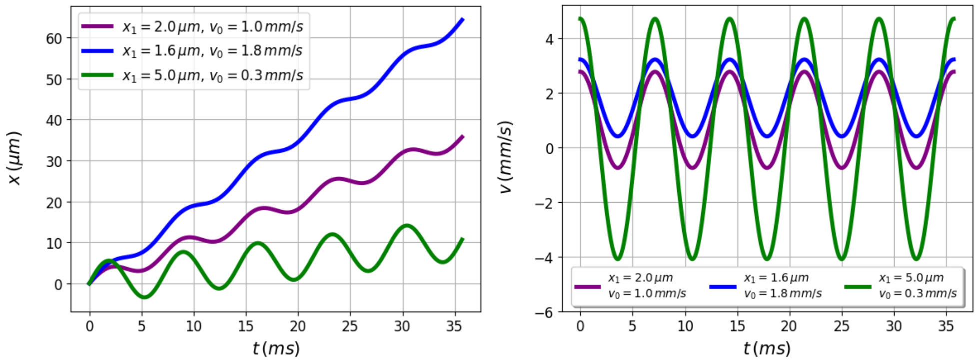

(a) $x(t)$ vs t.

(b) $v(t)$ vs t.

Figure 4.1: ***(a)***: *Plot of Eq. (4.1), describing the law of motion $x(t)$ of the optical barrier when subjected to an modulated driving.*
(b): *Plot of Eq. (4.2), representing the barrier's velocity $v(t)$ obtained by differentiating Eq. (4.1). Both panels show various curves, corresponding to the same modulation frequency of $\nu = 140\,Hz$ but different values of the driving amplitude x_1 and of the initial velocity v_0, as shown in the plot's legend.*

parameters x_1, ν and v_0:

$$I(t) = \frac{v_0\,N}{L_x} + \frac{2\pi\nu x_1\,N}{L_x}\cos\left(2\pi\nu\,t\right) = I_{DC} + I_{AC}\,\cos\left(2\pi\nu\,t\right) \tag{4.3}$$

where we defined $I_{AC} = 2\pi\nu x_1\,N/L_x$ as the amplitude of the oscillating current term, while I_{DC} is the direct current component. By tuning the aforementioned parameters, namely I_{DC}, I_{AC}, and ν, we can explore the junction's transport properties under different driving conditions. We can also change the time of the barrier's movement (or, equivalently, of the current's injection) before the absorption imaging process; we often choose to image the system, with respect to the start of the dynamics, at a time equal to t_{barr}, which is related to the chosen modulation by the following equation:

$$t_{barr} = \frac{N_{Cycles}}{\nu} \tag{4.4}$$

where ν is the set modulation frequency, while N_{Cycles} is the number of oscillation periods considered when driving the barrier. The $v_0\,t$ term reported in Eq. (4.1) represents the DC component of the barrier driving: this obstacle always travels a distance given by $v_0\,t_{barr}$, since its movement is modulated for an integer number of periods N_{Cycles}. In fact, the oscillatory driving term $v_{osc}(t)$ presented in Eq. (4.2) averages to zero over a driving period ($\int_0^T \cos\left(2\pi\nu\,t\right) = 0$), resulting in no net barrier displacement due to this modulation. The only contribution to the total distance spanned by the barrier is thus given by the DC term $v_0\,t$. An example of the thin barrier movement during time inside our junction, obtained by driving the system via the modulated trajectory of Eq. (4.1), is shown in Fig. 4.2: this corresponds to the injection of a periodic atomic current, whose expression is described by Eq. (4.3), for a time period equal to $t_{barr} = 45.4\,\mathrm{ms}$ ($N_{Cycles} = 11$).

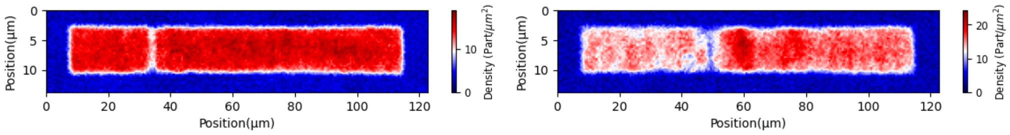

(a) $t = 0\,\mathrm{ms}$ **(b)** $t = 14.4\,\mathrm{ms}$

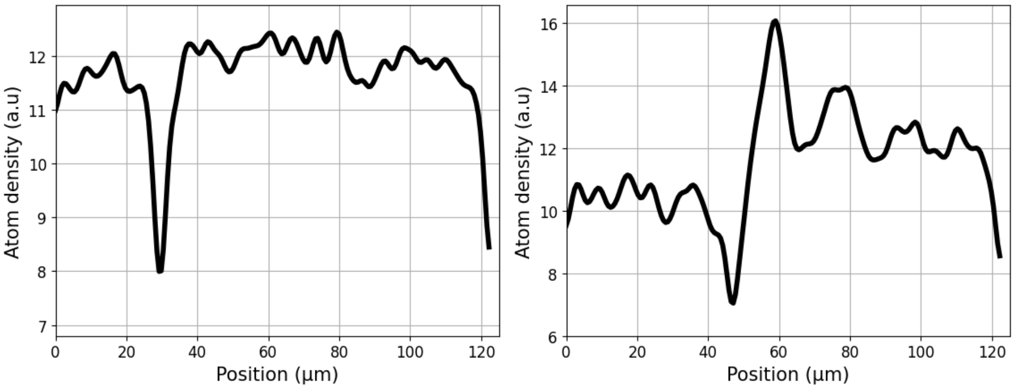

(c) $t = 0\,\mathrm{ms}$ **(d)** $t = 14.4\,\mathrm{ms}$

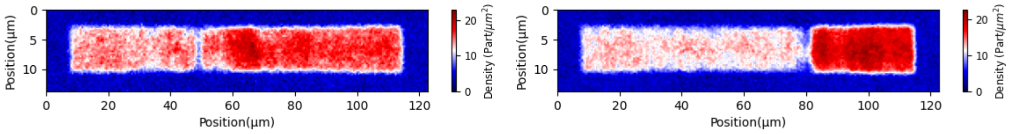

(e) $t = 15.4\,\mathrm{ms}$ **(f)** $t = 45.4\,\mathrm{ms}$

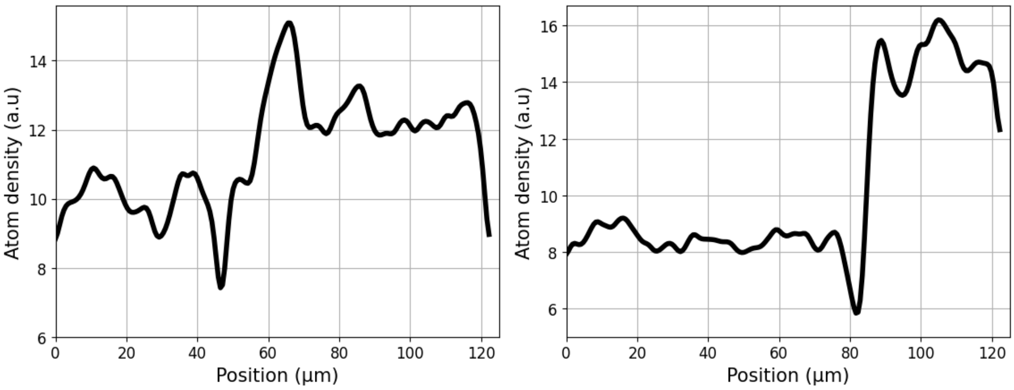

(g) $t = 15.4\,\mathrm{ms}$ **(h)** $t = 45.4\,\mathrm{ms}$

Figure 4.2: *Josephson dynamics due to the AC barrier's displacement at different times, such that the initial time* $t = 0\,ms$ *is taken when the optical barrier starts moving within the Josephson junction. The color scale reports the cloud 2-D density* $n(x, y)$*. The law of motion is described by Eq. (4.2), where the velocity is set to a value of* $v_0 = 1.2\,mm/s$*, with a modulation amplitude of* $x_1 = 1.14\,\mu m$ *and an oscillation frequency of* $\nu = 245\,Hz$*. The power of the trapping laser is set to* $P_{DMD} = 135\,mW$*.*

As in the DC driving case, reported in Sec. 3.2, we clearly observe the build-up of a non-zero $\Delta\mu$ on the same direction of the barrier's movement (right side), as time increases: this phenomena manifests as a density imbalance within the junction, occurring since the average driving velocity $\langle v(t)\rangle_T = v_0$ is comparable with the junction's critical velocity v_c (of order of $\sim 1\,\mathrm{mm/s}$ in these experimental conditions, as shown in Sec. 3.4).

4.2 Time evolution of $\Delta\mu$ during the barrier driving

Before discussing the experimental measurement of Shapiro steps we want to observe how the chemical potential difference $\Delta\mu$ evolves over time during the movement of the barrier. The latter is driven via an oscillating modulation, such that its law of motion is described by Eq. (4.1): the corresponding trajectory parameters are here set as $\nu = 245\,\mathrm{Hz}$, $v_0 = 1.2\,\mathrm{mm/s}$ and $x_1 = 1.14\,\mu\mathrm{m}$. Moreover, since the displacement of the optical barrier generates a nonzero $\Delta\mu$ after a certain critical velocity v_c is exceeded, we can also observe the density oscillations typical of the AC Josephson effect, discussed in Secs. 3.5.1 and 3.5.2, once the movement of the barrier is halted and the system is left evolving through tunneling phenomena. In this measurement we employ a rectangular Josephson junction with linear sizes $L_x = 125\,\mu\mathrm{m}$ and $L_y = 17.5\,\mu\mathrm{m}$, realized by following the procedure described in Sec. 2.1, which contains $N \approx 20\,\mathrm{K}$ atoms. The trapping laser power is here set to $P_{DMD} = 130\,\mathrm{mW}$, resulting in a trap depth to chemical potential ratio of about $V_0/\mu \sim 1.3$, the latter quantity being calculated through Eq. (2.21). For all the measurements reported in this chapter, unless otherwise specified, the Josephson junction is created under the same experimental conditions. The first measurement is effectuated as follows: the thin optical barrier is set into an oscillatory motion, described via Eq. (4.1), allowing the chemical potential difference within the junction to grow over time: the absorption imaging process, described in Sec. 2.1, is carried out at different times in order to extract the $\Delta\mu(t)$ curve during the barrier's driving. Since the displacement of the optical barrier is modulated by an oscillatory term with frequency $\nu = 245\,\mathrm{Hz}$, we expect the $\Delta\mu$ to oscillate in time at the same frequency ν while the optical barrier is displaced across the Josephson junction. We report in Fig. 4.3 the time evolution of the chemical potential difference $\Delta\mu$, which occurs during the alternating motion of the optical barrier. Experimental data is fitted by the following equation, representing a straight line modulated by a periodic function:

$$f(t) = A\,\cos\left(2\pi\nu\,t + \phi_0\right) + m\,t \tag{4.5}$$

where ν is the oscillation frequency, A is the modulation amplitude, ϕ_0 is the starting phase and m is the angular coefficient of the line. In Fig. 4.3, the chemical potential difference $\Delta\mu$ (or, equivalently, the density imbalance) between the reservoirs increases over time during the barrier's driving, since the constant velocity term of the displacement (v_0) is higher than the junction's critical velocity in these experimental conditions ($v_c \sim 1\,\mathrm{mm/s}$). This growth does not occur in a linear way, but $\Delta\mu$ oscillates in time with a certain frequency ν due to the fact that the barrier's trajectory is described by Eq. (4.1): this causes a time-modulated velocity $v(t)$ which oscillates above and below the critical velocity v_c. Therefore, the junction experiences both resistive ($\Delta\mu$ increases) and unresistive ($\Delta\mu$ constant) dynamics as the barrier is moved, depending on whether the speed at a certain time is supercritical or not. The

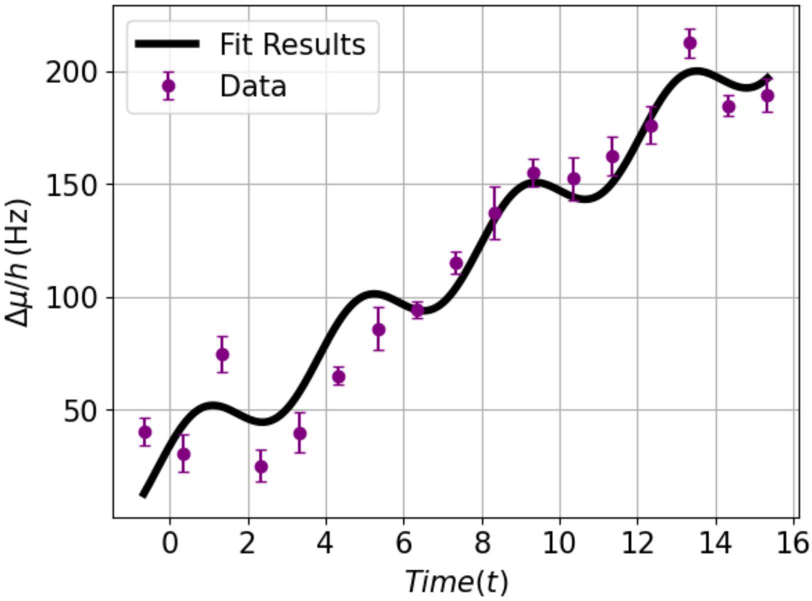

Figure 4.3: *Time evolution of the chemical potential imbalance $\Delta\mu$, occurring during the displacement of the Josephson barrier. Data is fitted with Eq. (4.5), in order to extract the oscillation's frequency. The observed oscillation during the growth of the $\Delta\mu$ in time is due to the periodic driving of the barrier via Eq. (4.1). The modulation frequency was set to $\nu = 245\,Hz$, while the measured oscillation frequency is found to be $\nu_{meas} = 242 \pm 8\,Hz$.*

extracted oscillation frequency is measured to be $242 \pm 8\,\text{Hz}$, compatible with the set modulation frequency within its error bar. The corresponding 1-D density profile of the superfluid cloud, measured during the barrier's movement inside the junction and integrated along the y-direction, is shown in Fig. 4.4 as a function of both the position within the optical potential ($x-$axis) and of the driving time ($y-$axis). In Fig. 4.4 we reported the predicted barrier's position as a function of time (white solid line and dots), effectuated by plotting Eq. (4.1) above the 2-D density profile. This curve overlaps compatibly with the actual position of the optical barrier, represented by the blue region inside the density profile: the Josephson barrier is therefore in the expected position during time, confirming that its movement is being performed correctly. On the other hand, the chemical potential imbalance $\Delta\mu$ observed in Fig. 4.4 was induced by driving the potential barrier with a periodic motion, having a mean velocity $\langle v(t)\rangle_T > v_c$ over a modulation period: therefore, density accumulations occur along the direction of the atomic current (or, equivalently, along the direction of the barrier's displacement), from right to left in Fig. 4.4. These density pulses are expected to propagate within the junction at a speed comparable with the speed of sound c_s, as discussed in Secs. 3.1 and 3.5.2. This statement is corroborated by plotting above the experimental profile the function $f(t) = c_s t + x_0$, describing an uniform motion occurring at the speed of the sound modes: this curve follows correctly the density pulses which are created during the barrier's driving, confirming that they represent sound excitations. In order to effectuate the second measurement (i.e. Joseph-

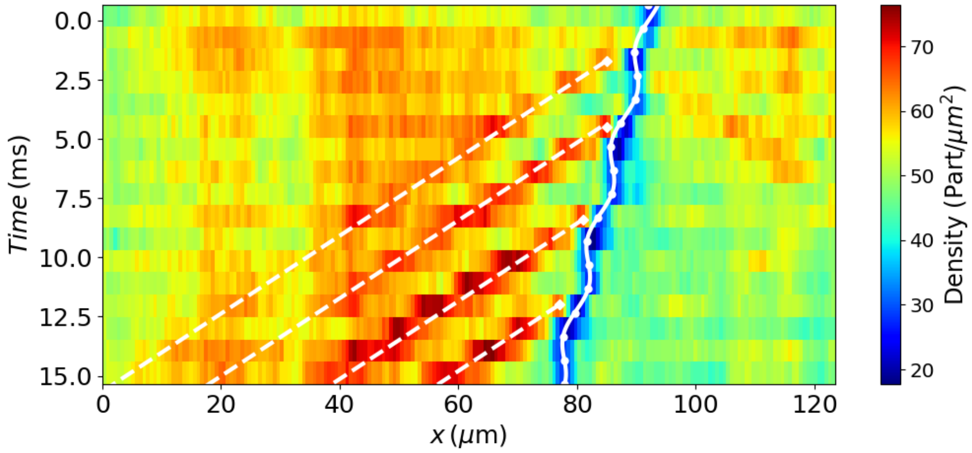

Figure 4.4: *1-D density profile of the junction as a function of time during the barrier's movement, integrated along the y-axis. The position of the barrier at different times (calculated through Eq. (4.1)), that are the ones reported on the x-axis of Fig. 4.3, is represented by white dots on the plot: the law of motion of the barrier is instead shown by plotting Eq. (4.1) with a white solid line. We observe the excited density pulses propagating inside the junction due to the movement of the barrier (the red structures going left-downwards). As discussed in Sec. 3.1, these excitations propagate at the speed of sound* c_s*: this is verified simply by plotting a series of straight lines with an angular coefficient equal to* c_s *(white dashed lines), which overlap nicely over the red pulses. These lines are described by the function* $f(t) = c_s t + x_0$*, where* x_0 *is their starting point (white diamonds).*

son oscillations) we halt the displacement of the optical barrier, and the $\Delta\mu$ imbalance which has been created during the driving triggers the AC Josephson dynamics: the absorption imaging process, done at different times after the barrier is stopped, allows to obtain the $\Delta\mu(t)$ curve during the Josephson oscillations. The measured $\Delta\mu - t$ oscillation is shown in Fig. 4.5, together with its corresponding curve fit; the latter is effectuated through the damped periodic function reported in Eq. (3.5). A priori, we expect the $\Delta\mu$ oscillations in time, which set in at the end of the barrier's movement, to occur at a frequency comparable with the result reported in Sec. 3.5, obtained for the same experimental conditions (namely, junction size $L_x \times L_y$ and trapping laser power P_{DMD}). In the latter case, where the density dynamics was triggered by a preliminary $\Delta\mu$ imbalance realized by displacing the optical dipole trap position, the oscillation frequency was found to be $\nu_J = (20.3 \pm 0.3)\,\text{Hz}$, as reported in Tab. 3.3. In the present measurement, the extracted oscillation frequency is found to be $\nu_J = (19.7 \pm 0.2)\,\text{Hz}$, compatible within its error bar with the previous result. This outcome confirms that the behavior of the Josephson oscillations, occurring in the AC regime and discussed in Sec. 3.5, does not depend on the particular mechanism employed for generating the initial non-zero $\Delta\mu$.

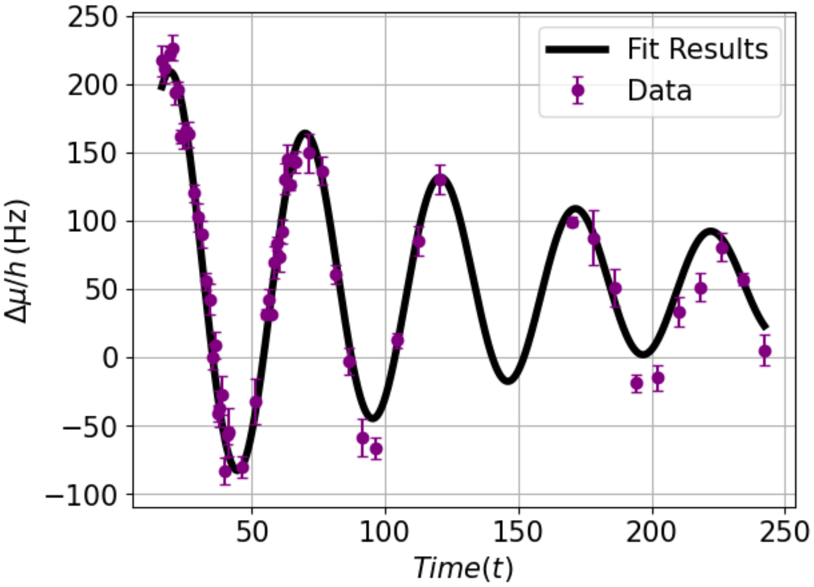

Figure 4.5: *Damped oscillations of $\Delta\mu$ during time occurring due to tunneling phenomena, which set in at the end of the barrier's movement when a non-zero $\Delta\mu$ has accumulated between the sides of the junction. Experimental data is fitted with Eq. (3.5) in order to extract the oscillation frequency, returning a value of about $\nu_J = (19.7 \pm 0.2)$ Hz.*

4.3 Shapiro steps measurements

As we discussed in Sec. 1.6, the application of an alternating current $I(t)$ inside a superconducting Josephson junction causes the emergence of particular structures in the $I - \Delta V$ characteristic, known as Shapiro steps, where almost discontinuous jumps between plateaus having constant potential difference ΔV occurs, as shown in Fig. 1.13. In the present section we will report the measurement results associated with this phenomena, obtained by current-biasing our ^{6}Li superfluid Josephson junction with the procedure described in Sec. 4.1: an atomic oscillating current $I(t) = I_{DC} + I_{AC}\ \cos(2\pi\nu\, t)$ is generated by driving the optical barrier through the law of motion reported in Eq. (4.1). Measurements are made as follows: the atomic Josephson junction is realized in the rectangular hybrid potential of the DMD, in the same experimental conditions reported in Sec. 4.2. Since approximately $N = 20\,\mathrm{K}$ atoms are loaded before starting the barrier's dynamics, the calculated trap depth to chemical potential ratio is found to be about $V_0/\mu \sim 1.3$. The cloud's density within the two reservoirs composing the junction is preliminary balanced by finely displacing the TEM$_{0,1}$ optical dipole trap through a pico-motor, so that at the beginning of the measurement we have $\Delta\mu = 0$: this is done in order to avoid couplings between the barrier's driving and the oscillations of density occurring in the AC Josephson dynamics, which could set in if a finite $\Delta\mu$ is initially present. The thin optical barrier is then set into motion, its velocity during time being described by Eq. (4.2), in order to generate the alternate current which triggers the dynamics: this displacement occurs for a time equal to t_{barr}, which value depends on the particular modulation employed through Eq. (4.4). When the barrier's movement is halted, the absorption imaging process described in Sec. 2.1 is carried out, extracting the *in-situ* 2-D optical density OD and, consequently, the chemical potential difference $\Delta\mu$ between the two sides of the junction, which can be evaluated through Eqs. (2.3) and (2.9). The aforementioned process is repeated for different values of the initial velocity v_0, representing the DC driving component of the barrier's motion, in order to obtain the $\Delta\mu - v_0$ (or, equivalently, the $\Delta\mu - I_{DC}$) characteristic, in which we expect to observe the Shapiro steps if a modulated component $I_{AC} \neq 0$ of the current is present. As discussed in Sec. 3.2, the displacement velocity of the barrier can be converted into a particle current by means of Eq. (3.3). The injection of the alternating current $I(t)$ is effectuated with the possibility of varying two external parameters, other than the direct current term I_{DC}: the modulation amplitude x_1 and the oscillation frequency ν. These quantities are chosen such that their product $\nu \cdot x_1$ assumes only certain values: in the following, we fix this amount to either $\nu \cdot x_1 = 140\,\mu\text{m/s}$ or $\nu \cdot x_1 = 280\,\mu\text{m/s}$. As a consequence, the I_{AC} term of Eq. (4.3), which represents the intensity of the alternate driving component of the total current $I(t)$, remains constant for different measurements having the same value of $\nu \cdot x_1$. Moreover, for each Shapiro steps measurement obtained through the application of an alternate current $I(t)$, we also measure the respective $\Delta\mu - I_{DC}$ characteristic occurring in the DC Josephson dynamics, where a direct non-modulated current I_{DC} is applied: since the modulation frequency ν changes between the various measurements, this procedure allows also to extract the critical current I_c as a function of the driving time t_{barr}, which value depends on the particular driving via Eq. (4.4). An example of the measured $\Delta\mu - v_0$ DC characteristic, occurring due to the application of a direct current I_{DC} within our junction, is reported in Fig. 4.6, together with its corresponding AC-driven characteristic (where the modulation amplitude is set to $x_1 = 2\,\mu\text{m}$): the optical barrier is driven for a time of approximately $t_{barr} = 21.4\,\text{ms}$ (corresponding to $N_{Cycles} = 3$, for $\nu = 140\,\text{Hz}$). The extracted critical current I_c and the conductance G, obtained by fitting Eq. (1.94) on the DC data, are shown in Figs. 4.7 (a) and 4.7 (b) as a function of the driving time t_{barr}: we expect the value of the critical current to be approximately constant between the various measurements, as it shouldn't depend on the time of the barrier's dynamics but rather on the applied trapping laser's power (which influences the barrier's depth V_0), on the bulk chemical potential μ of the ultracold cloud, on the condensed fraction N_0/N and the interaction parameter $1/k_F a$, which are kept approximately constant for different measurements [19]. The fitted critical current I_c shown in Fig. 4.7 (a) is found to fluctuate a bit between the various measurements (around a value of $I_c = 1.65 \pm 0.05 \cdot 10^5\,\text{Part/s}$), carried out for different driving times t_{barr}. This possibly occurs due to the fact that during the junction's realization the various quantities presented before (μ, N_0/N, $1/k_F a$) inevitably fluctuate for different experimental realizations, and since the focus of the microscopic objective is done manually it can change slightly for successive days: nevertheless, every measurement is compatible with a value of order of $10^5\,\text{Part/s}$, which constitutes the typical order of magnitude of the critical current within our junction, for the experimental conditions presented in Sec. 4.2. For a Josephson junction where the driving parameters are chosen such that $\nu \cdot x_1 = 280\,\mu\text{m/s}$, the amplitude of

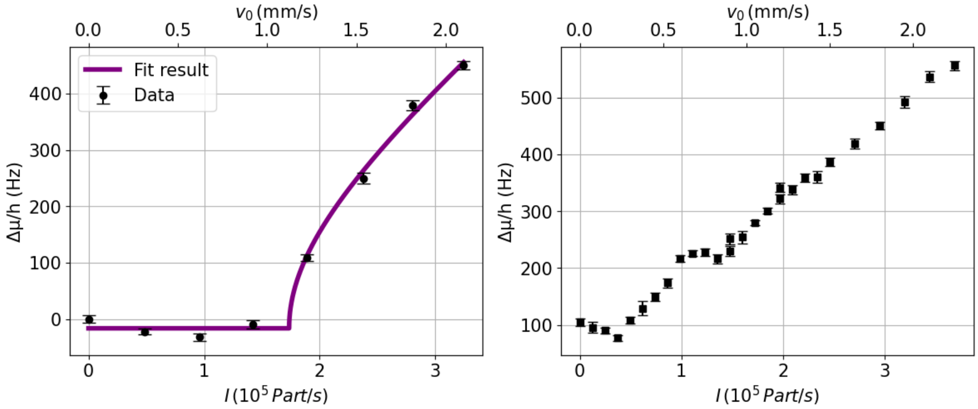

(a) DC Characteristic **(b)** AC Characteristic

Figure 4.6: *Experimental results for the $\Delta\mu - I$ characteristic of the Josephson junction in the case of a DC (panel (a)) and an AC driving (panel (b)) where the driving amplitudes are set respectively to $x_1 = 0$ and $x_1 = 2\,\mu m$. The optical barrier is displaced for time equal to about $t_{barr} \sim 21.4\,ms$, corresponding to $N_{cycles} = 3$ and $\nu = 140\,Hz$. The purple line in panel (a) represents the curve fit of the data, effectuated via Eq. (1.94). The corresponding conductance is found to be $G \cdot h = 580 \pm 10$, while the critical current is given by $I_c = (1.73 \pm 0.02) \cdot 10^5\,Part/s$. On panel (b) we observe the typical plateau-like structure exhibited by Shapiro steps, obtained by injecting an AC current.*

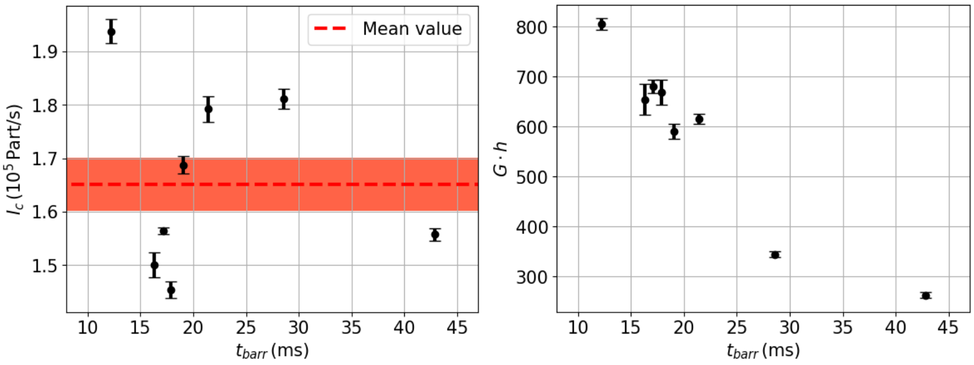

(a) I_c vs ν **(b)** G vs ν

Figure 4.7: ***(a)**: Extracted critical current I_c as a function of the driving time t_{barr}: this quantity is approximately centered towards a mean value of $I_c = (1.65 \pm 0.05) \cdot 10^5\,Part/s$. We represent this amount with the red dashed horizontal line reported in figure, together with its error bar (orange shaded region).*
***(b)**: Extracted conductance G as a function of the driving time t_{barr}.*

the alternating current is approximately $I_{AC} = 2\pi\nu x_1 N/L_x \approx 2.8 \cdot 10^5$ Part/s: this value is greater than the measured average value of the critical current

($I_c = (1.65 \pm 0.05) \cdot 10^5\,\text{Part/s}$), and resistive behaviors occur during the barrier's movement, as explained in Sec. 4.2. On the other hand, the value of the conductance G, reported in Fig. 4.7 (b), decreases while increasing the driving time t_{barr}. This behavior has already been observed in Sec. 3.4, and occurs due to the fact that for longer driving times the chemical potential difference $\Delta\mu$ grows to larger values when v_0 is fixed: the system is therefore found to be more resistive for longer times, resulting in a higher resistance R and a smaller conductance $G = R^{-1}$. The reason behind the dependence of the measured conductance G on the driving time t_{barr} is to be found in the way we measure the $\Delta\mu$: in fact, by displacing the optical barrier we generate an excitation that propagates within the system at the speed of sound c_s, as shown in Secs. 3.1 and 3.5.2. The density imbalance is successively measured along the entire junction, regardless of the particular driving time chosen. If this value is too small, the density impulse does not propagate across the whole junction, and the information created due to the injected current does not reach all particles within the system: this results in a measured lower $\Delta\mu$ and a higher conductance G. Conversely, if the driving time is too high, these excitations can rebound on the edge of the optical potential. The chemical potential difference which sets in after this phenomena is therefore due to the combined action of the external current and the free propagation of density pulses inside the system. As an estimate of the true value of the conductance G characterizing our system, we choose the one measured at a driving time such that a density pulse generated at $t = 0$ in the initial position of the barrier ($92.5\,\mu$m from the left side of the junction) is able to propagate exactly to the end of the junction (left side), in order to avoid the problems discussed above: a sound mode having a speed of $c_s = 6.09 \pm 0.04\,\text{mm/s}$ (see Sec. 3.1) covers this distance in a time equal to about $t = (15.4 \pm 0.1)\,\text{ms}$. Therefore, since for the measurement effectuated with $N_{cycles} = 3$ and $\nu = 175\,\text{Hz}$ the barrier's driving time (at the end of which absorption imaging is performed) is set to $t_{barr} = 17\,\text{ms}$, similar to the required time $t \approx 15.4\,\text{ms}$, its corresponding value of the conductance $G \cdot h = 680 \pm 5.8$ represents the best estimate of this quantity for our experimental system.

4.3.1 Data analysis

As we observe from Fig. 4.6 (b), a different behavior from a typical $\Delta\mu - I$ DC characteristic is observed when injecting an alternating current $I(t)$, having plateaus of almost constant chemical potential difference $\Delta\mu$ separated by resistive regions: the measured structure corresponds to the phenomena of *Shapiro steps*, introduced in Sec. 1.6.4. This paragraph is devoted in discussing how to perform the data analysis of such experimental curves, obtained by displacing the thin optical barrier with different driving frequencies ν. In particular, we will study the behavior of two physical quantities as a function of the modulation frequency ν: the position of the first step I_{S_1} (in current units) and the distance (in frequency units) between two successive plateaus at constant $\Delta\mu$, the step height $\Delta\mu_S$. As we discussed in Sec. 1.6.4, we expect the latter quantity to be comparable with the oscillation frequency ν of the barrier's motion, as a consequence of the resonance between the modulation of the barrier and the phase velocity $\partial\phi/\partial t$: on the other hand, the step position value I_S is predicted to depend on the driving current $I_{AC} = 2\pi\nu x_1 N/L_x$

Table 4.1: *Fit results for $\Delta\mu_{S_1}$ and I_{S_1} of the first step together with their relative error bars, obtained by fitting Eq. (4.6) to the experimental data reported in Fig. 4.9.*

ν (Hz)	x_1 (μm)	$\Delta\mu_{S_1}$ (Hz)	I_{S_1}/I_c	I_c (10^5 Part/s)	$\nu \cdot x_1$ (μm/s)
105	1.3	156 ± 28	0.66 ± 0.03	1.81 ± 0.02	140
175	0.8	122 ± 7	0.77 ± 0.02	1.56 ± 0.01	140
245	0.57	178 ± 11	0.79 ± 0.03	1.64 ± 0.02	140
70	4	80 ± 14	0.14 ± 0.02	1.55 ± 0.01	280
105	2.6	120 ± 23	0.16 ± 0.03	1.81 ± 0.02	280
140	2	129 ± 7	0.45 ± 0.02	1.79 ± 0.02	280
175	1.6	156 ± 18	0.47 ± 0.03	1.56 ± 0.01	280
210	1.3	205 ± 7	0.59 ± 0.02	1.68 ± 0.01	280
245	1.14	182 ± 13	0.61 ± 0.04	1.64 ± 0.02	280
280	1	243 ± 8	0.72 ± 0.02	1.45 ± 0.01	280

in a non-trivial way, being analytically represented by Bessel functions. In order to extract $\Delta\mu_S$ and I_{S_1} from experimental data, we decide to carry out a phenomenological fit through a function able to pinpoint these quantities from the $\Delta\mu - I$ curve. The chosen fitting curve is the following multiple sigmoid function:

$$f(I_{DC}) = off + \sum_{i=1}^{2} \frac{\Delta\mu_{S_i}}{1 + \exp\left(-(I_{DC} - I_{S_i})/s_i\right)} \tag{4.6}$$

where s_i quantifies the steepness of the $i - th$ sigmoid, while $\Delta\mu_{S_i}$ and I_{S_i} represent respectively the relative height and the position of the $i - th$ Shapiro step. The second step height (with respect to the $\Delta\mu$ value obtained at $v_0 = 0$) is calculated by fitting the sigmoid function reported in Eq. (4.6) on the experimental data, and then by summing the height values of the first and second plateau, $\Delta\mu_{S_{2nd}} = \Delta\mu_{S_1} + \Delta\mu_{S_2}$. We report in Fig. 4.8 examples of such a curve fit, carried out on various datasets having different modulation frequency ν and different driving amplitudes x_1. The height $\Delta\mu_S$ and the position I_{S_1} of the first Shapiro step, both quantities obtained by fitting Eq. (4.6) to experimental data, are reported in Fig. 4.9 as a function of the modulation frequency ν, for two different values of the $\nu \cdot x_1$ product (140 and 280 μm/s): the step height $\Delta\mu_S$, reported in frequency units, has been normalised by the corresponding modulation frequency, while the step position I_S is divided by the critical current I_c. We also report in Tab. 4.1 the fitted values for the position I_{S_1} and the height $\Delta\mu_{S_1}$ of the first Shapiro step. We observe that the $\Delta\mu_{S_1}/h\nu$ ratio, reported in Fig. 4.9 (a), is compatible with unity for low-frequency measurements within the experimental error bar: this behavior is explained in the framework of the tilted washboard potential discussed in Sec. 1.6.4, where Shapiro steps are predicted to occur due to a synchronization between the phase dynamics and the barrier's displacement, resulting in Eq. (1.107). On the other hand, this ratio is found to be a bit lower for the high-frequency ones since the barrier is moved for a lower driving time $t_{barr} = N_{Cycles}/\nu$, and the chemical potential imbalance does not saturate around its maximum value for this time. The position of the first step I_{S_1}, normalised by the critical current

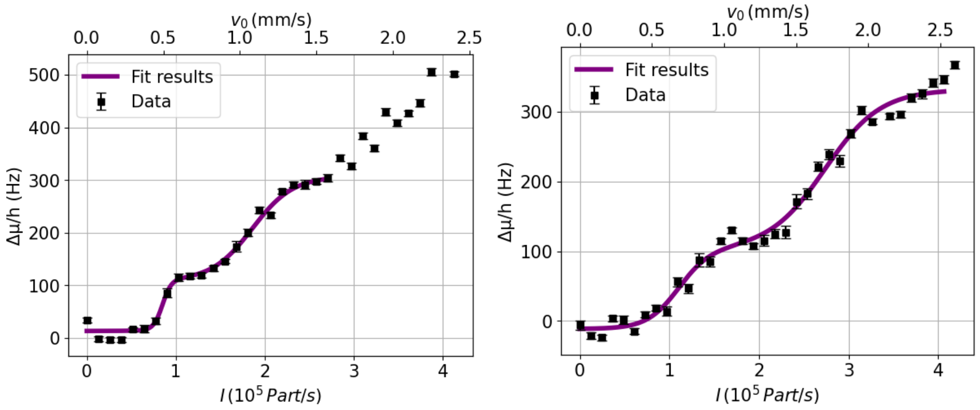

(a) $\nu = 140\,\mathrm{Hz},\ x_1 = 2.0\,\mu\mathrm{m}$ **(b)** $\nu = 245\,\mathrm{Hz},\ x_1 = 1.14\,\mu\mathrm{m}$

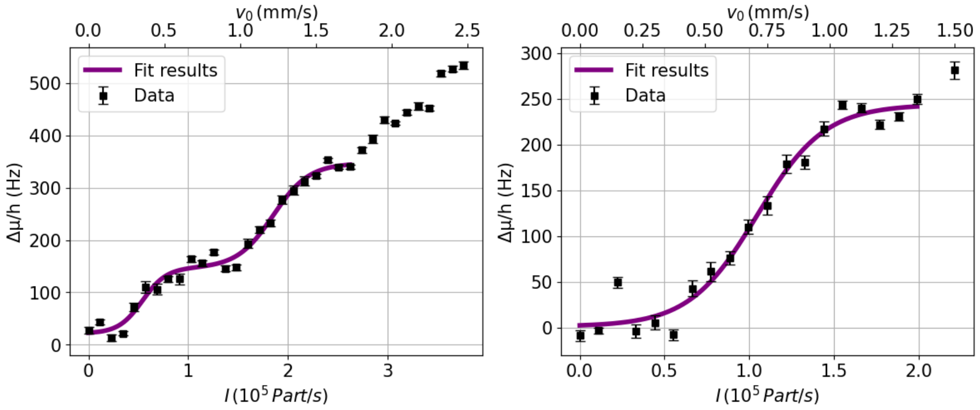

(c) $\nu = 175\,\mathrm{Hz},\ x_1 = 0.8\,\mu\mathrm{m}$ **(d)** $\nu = 280\,\mathrm{Hz},\ x_1 = 1\,\mu\mathrm{m}$

Figure 4.8: *Experimental data together with multiple Shapiro steps fit, performed via Eq. (4.6), for different values of the driving amplitude* x_1 *and of the modulation frequency* ν. *The first Shapiro step is always fitted in our data analysis, while the second step is fitted whenever possible.*

(a): *Experimental data obtained by setting* $\nu = 140\,Hz$ *and* $x_1 = 2.0\,\mu m$, *such that* $\nu \cdot x_1 = 280\,\mu m/s$. *The extracted step height is* $\Delta\mu_{S_1} = 123 \pm 6\,Hz$ *for the first step, and* $\Delta\mu_{S_{2nd}} = 282 \pm 22\,Hz$ *for the second step.*

(b): *Experimental data obtained by setting* $\nu = 245\,Hz$ *and* $x_1 = 1.14\,\mu m$, *such that* $\nu \cdot x_1 = 280\,\mu m/s$. *The extracted step height is* $\Delta\mu_{S_1} = 137 \pm 6\,Hz$ *for the first step, and* $\Delta\mu_{S_{2nd}} = 343 \pm 20$ *for the second step.*

(c): *Experimental data obtained by setting* $\nu = 175\,Hz$ *and* $x_1 = 0.8\,\mu m$, *such that* $\nu \cdot x_1 = 140\,\mu m/s$. *The extracted step height is* $\Delta\mu_{S_1} = 122 \pm 5\,Hz$ *for the first step, and* $\Delta\mu_{S_{2nd}} = 343 \pm 20\,Hz$ *for the second step.*

(d): *Experimental data obtained by setting* $\nu = 280\,Hz$ *and* $x_1 = 1\,\mu m$, *such that* $\nu \cdot x_1 = 280\,\mu m/s$. *The extracted step height is* $\Delta\mu_{S_1} = 243 \pm 7\,Hz$.

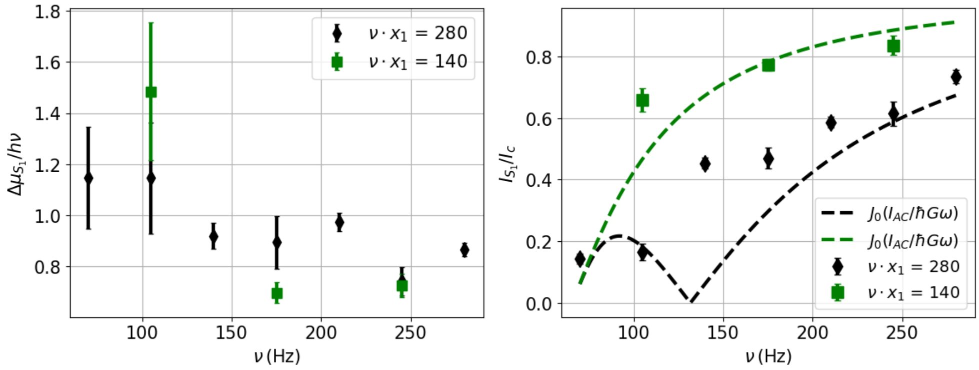

(a) $\Delta\mu_S/\hbar\nu$ vs ν **(b)** I_{S_1}/I_c vs ν

Figure 4.9: *(a): Step height $\Delta\mu_{S_1}$, normalised by the modulation frequency ν, as a function of the latter.*
(b): Step position I_{S_1}, normalised by the critical current I_c extracted by the associated DC fits, as a function of the modulation frequency ν, reported together with its corresponding Bessel function J_0 (dashed line). In both figures, different data for $\nu \cdot x_1 = 280\,\mu m/s$ (black points) and for $\nu \cdot x_1 = 140\,\mu m/s$ (green squares) are shown.

I_c, is reported in Fig. 4.9 (a) as a function of the modulation frequency ν: we can see a monotonically increasing behavior of this quantity with increasing frequency. More specifically, it is expected that the half-width of the n-th step can be analitically represented by the n-th order Bessel function [63, 4, 64], such that $\Delta I_n/I_c = |J_n(\frac{I_{AC}}{\hbar G\omega})|$ (where $\omega = 2\pi\nu$), in presence of a voltage-biased junction and in the overdamped regime of the RCSJ model ($\beta_c \ll 1$), where the particle's inertia (C) is dominated by dissipative processes (G). The curves $J_0(x) = \sin(x)/x$ (where $x = I_{AC}/(\hbar G\omega)$), describing the position of the first step I_{S_1} normalised by the critical current I_c, are reported in Fig. 4.9 (b), plotted by using the value of the conductance estimated in the precedence ($G = 680 \pm 5.8$): they catch at least phenomenologically the behavior of the measured data. The discrepancy with the experimental data is given by the fact that Bessel functions predict the behavior of the steps position only in the case of an applied alternating voltage $V(t)$, as $\Delta I_n/I_c = |J_n(\frac{V}{h\nu})|$ [27]: since in our experiment the external driving is due to an alternating current $I(t)$, the width of the steps for low values of the modulation amplitude I_{AC} can deviate from this predicted behavior. For completeness, we report in Fig. 4.10 the y-axis integrated density profile associated with the AC curve of Fig. 4.8 (b), as a function of the constant speed v_0: we observe that, for high DC velocities v_0, a density accumulation sets in along the direction of the barrier's displacement, as shown in Fig. 3.9 for the case of a purely DC driving. In the AC case, this occurs because the mean driving velocity $\langle v(t)\rangle_T$ is higher than the junction's critical velocity v_c. We report in Fig. 4.11 the results of numerical simulations of the RSJ model, compared with experimental data: the simulations are done by numerically solving Eq. (1.93) using the set modulation frequency ν , while G and v_c are extracted from the DC curves by fitting Eq. (1.94).
From Fig. 4.11 we see that numerical solutions are compatible with experimen-

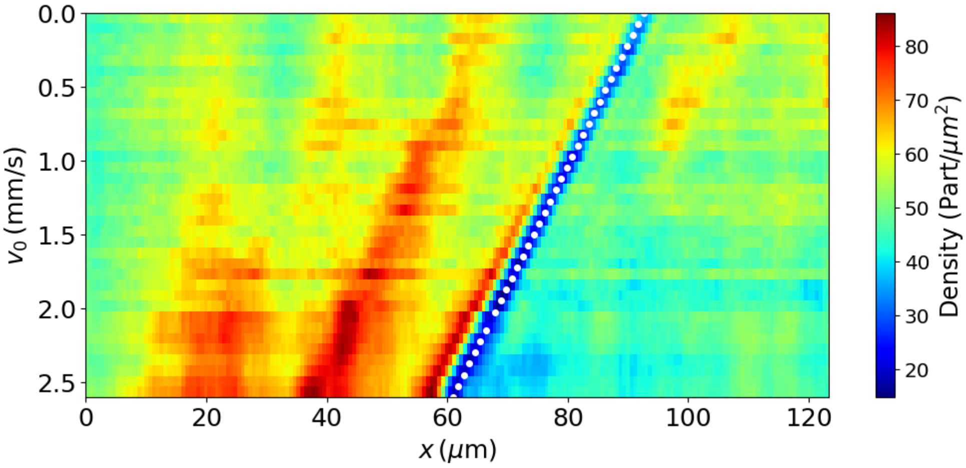

Figure 4.10: *Integrated density along the y-axis as a function of v_0, obtained from the data of Fig. 4.8 (b). White dots correspond to the position of the barrier's center at the end of the driving process (occurring in a time equal to $t_{barr} = 12.2\,ms$), calculated through Eq. (4.1).*

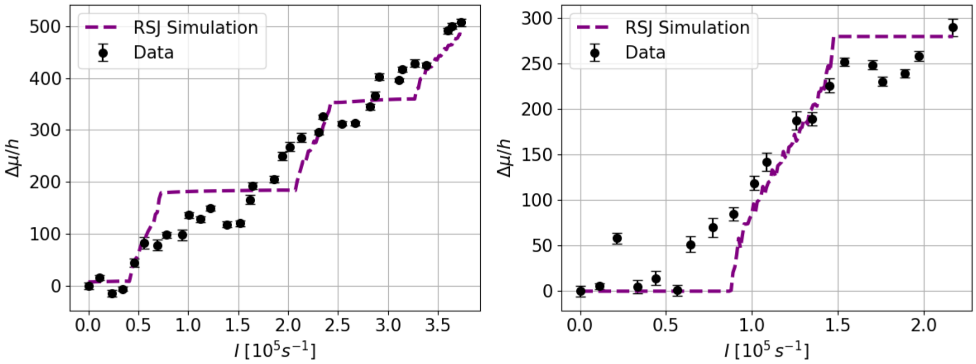

(a) $\nu = 175\,\mathrm{Hz}$, $x_1 = 1.6\,\mu\mathrm{m}$ **(b)** $\nu = 280\,\mathrm{Hz}$, $x_1 = 1\,\mu\mathrm{m}$

Figure 4.11: *Numerical solutions of the RSJ model, compared with the experimental data. Fig.(a) is reporting the dataset (black dots) with $\nu = 175\,Hz$ and $x_1 = 1.6\,\mu m$, and the corresponding simulation (purple dashed line). In Fig.(b), the data with $\nu = 280\,Hz$ and $x_1 = 1\,\mu m$ is shown.*

tal data: this confirms that the transport properties of our atomic Josephson junction are well described in terms of the RSJ circuital model, where $C = 0$. In order to extend the obtained results for the chemical potential difference jump $\Delta\mu_{S_2}$ occurring in the second plateau, we report in Fig. 4.12 the measured values of the step height for the first and the second Shapiro step as a function of the driving frequency ν, extracted by fitting Eq. (4.6) on the experimental data.

The extracted values of the second Shapiro step height reported in Fig 4.12 are reported in Tab. 4.2, together with their corresponding error bars. In Fig. 4.12 two straight lines described by the equation $f(\nu) = n \cdot \nu$ are shown together

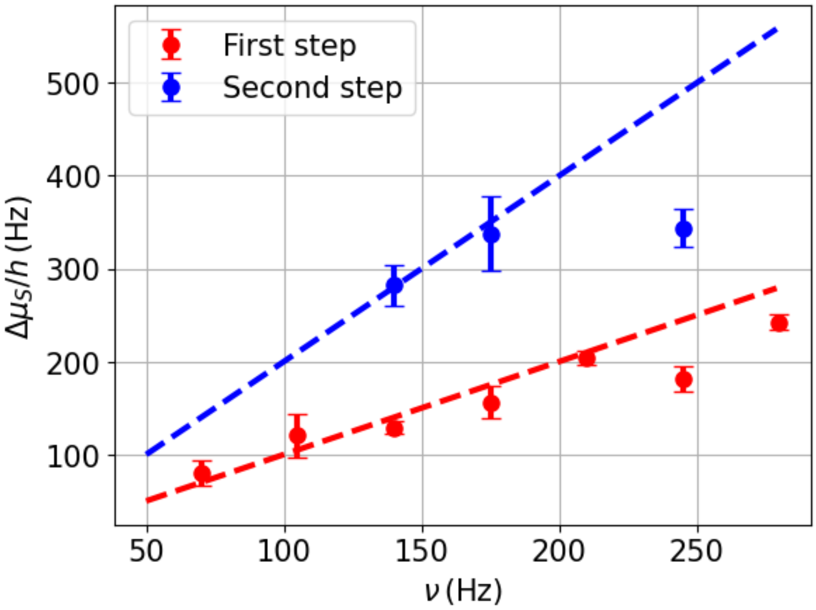

Figure 4.12: *Measured height for the first and the second Shapiro step, reported as a function of the modulation frequency* ν*. The dashed lines represent the curve* $f(\nu) = n \cdot \nu$*, where* n *is the step number.*

Table 4.2: *Fit results for the second step height* $\Delta\mu_{2nd}$*, obtained by fitting Eq. (4.6) to the experimental data reported in Fig. 4.12.*

ν (Hz)	x_1 (μm)	$\Delta\mu_{2nd}$ (Hz)
140	2	282 ± 22
175	1.6	338 ± 40
245	1.14	343 ± 20

with the experimental points, in order to further validate the expected behavior of the n-th Shapiro step height, reported in Eq. (1.107). As already discussed, we expect that for each Shapiro step, occurring due to phase slippage phenomena, the chemical potential must jump by $\Delta\mu_S \sim h\,\nu$. Since the plotted lines are compatible with the measured data for low-frequency measurements, within the latter's error bar, this prediction is well reproduced in our experiment. The discrepancy observed for the high-frequency points may again occur due to lower driving times t_{barr}, which cause the chemical potential imbalance $\Delta\mu$ to not be measured at its real maximum value as the density perturbation has not spread throughout the whole junction yet. Nevertheless, the results obtained in this section clearly show how the height of the Shapiro steps strongly depends on the set modulation frequency ν, as expected.

4.4 Vortex nucleation and Shapiro steps

As described in Sec. 1.5, one of the possible types of excitations which can be generated within a condensate is represented by quantum vortices: they are closely related to the peculiar rotational properties of a superfluid, whose irrotational velocity field ($\vec{\nabla} \times \vec{v} = 0$, consequence of the gauge symmetry breaking) is associated with a quantized circulation through any closed path. Each vortex is characterized by an integer index, the winding number w, which has been introduced in Eq. (1.77) and determines the amount of angular momentum carried by the excitation. In particular, this latter quantity is found to be a multiple of the circulation quanta h/m via the aforementioned index w, such that $L_{vort} = w\, h/m$. In the present section we investigate the relationship between the emergence of Shapiro steps and the nucleation of quantized vortices during the barrier's modulated driving: in our physical system vortex excitations can be observed as density depletions within the cloud's profile, generated due to dissipative effects. The measurement procedure employed for detecting these excitations is carried out as follows: first, a density balanced superfluid Josephson junction is realized in the optical hybrid potential of the DMD with the specifics reported in Sec. 4.2, employing the experimental sequence discussed in Sec. 2.1. The thin optical barrier is then set into motion within the potential, according to the trajectory described by Eq. (4.1). When the external driving is stopped, we remove the optical barrier through a 0.24 ms ramp down process: after waiting for a time of about 4 ms with respect to the barrier removal, a 2 ms time-of-flight (TOF) is effectuated by turning off all optical traps, as explained in Sec. 2.4. This technique further increases the vortex's visibility inside the atomic cloud. Finally, at the end of the TOF the absorption imaging process is carried out, allowing to measure the number of vortices N_{vort} that have been generated during the barrier's driving. This number has to be manually counted for each different repetition. We report in Fig. 4.13 an example of the superfluid Josephson junction, imaged at the end of the barrier's movement for both DC and AC drivings, where single vortices and vortex dipoles are observable. One possible way for studying the connection between Shapiro steps and vortex dipoles consists in measuring the number of vortex N_{vort} as a function of the barrier's velocity v_0: this result can be compared with the $\Delta\mu - v_0$ characteristic which we observe as a consequence of the external driving. For extracting the $N_{vort} - v_0$ curve we carry out the absorption imaging process at the end of the barrier's movement, which is stopped after a time equal to $t_{barr} = 17\,\text{ms}$ ($N_{Cycles} = 3$, for $\nu = 175\,\text{Hz}$), for different values of the driving velocity v_0. We effectuate this measurement both in the presence of a DC driving ($x_1 = 0$) and in the case of a modulated trajectory (AC current, $x_1 = 1.6\,\mu\text{m}$, $\nu = 175\,\text{Hz}$). The measurement results of the vortex number N_{vort} are reported in Fig. 4.14 for both cases of DC and AC driving, together with their corresponding chemical potential difference characteristic, $\Delta\mu - v_0$. In our system, quantized vortices can be therefore observed during the displacement of the Josephson barrier inside the superfluid junction. Their nucleation is associated with the exceedance of the Landau's critical velocity near the thin optical barrier, where the local particle density n_{loc} is lower than the average density n within the rest of the junction: in Bose-Einstein condensates this critical value is represented by the sound velocity c_s, which depends on the cloud's density through the chemical potential μ_{BEC}, as reported in Eq. (2.13). For smaller densities, the resulting sound velocity decreases: therefore, it is much easier to generate this kind of excitations in the proximity of the optical barrier since the thresh-

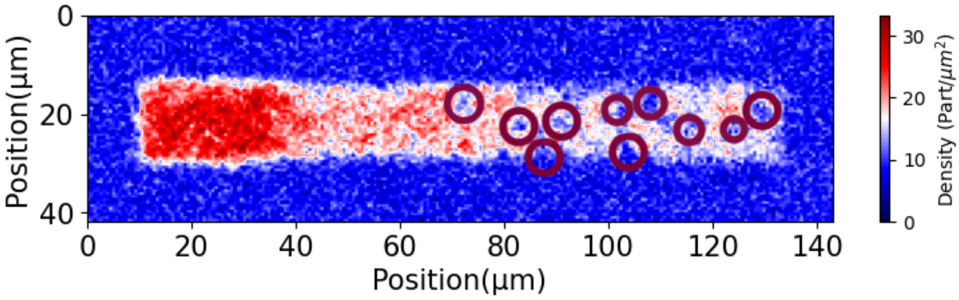

(a) *Vortex observance after a DC driving.*

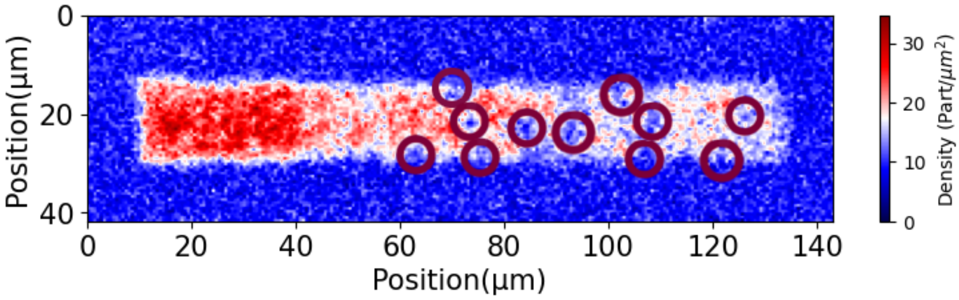

(b) *Vortex observance after an AC driving.*

Figure 4.13: ***(a)***: *Density profile within the Josephson junction after the barrier's driving, done for the following barrier parameters: $v_0 = 2.0\, mm/s$, $x_1 = 0$ (DC driving), and $t_{barr} = 17\, ms$.*
(b): *Density profile within the Josephson junction after the barrier's driving, done for the following barrier parameters: $v_0 = 2.0\, mm/s$, $x_1 = 1.6\, \mu m$ (AC driving), and $t_{barr} = 17\, ms$. Red circles highlight the presence of vortices within the junction in both cases.*

old velocity of the process is lower. As discussed in Sec. 3.4, this mechanism also explains why the critical velocity v_c of the junction, measured in the DC Josephson effect, is found to be smaller than the sound velocity c_s: in this regime the establishment of a non-zero $\Delta\mu$ occurs due to the exceedance of the Landau's critical velocity near the optical barrier, that is, the local speed of sound $c_s^{loc} \neq c_s^{bulk}$. Since the optical barrier is displaced along one side of the Josephson junction without applying a net torque to the trapped ultracold gas, the total angular momentum of the system must be conserved: therefore, vortex excitations nucleate in pairs, having opposite winding numbers w, in order to satisfy this condition. The generated physical entity is known as a vortex dipole, and is made up by a vortex (winding number w) and an anti-vortex (winding number $-w$). According to the previous discussion, in both the DC and AC case of Fig. 4.14, when the set barrier speed v_0 is sufficiently high we observe the occurrence of vortex-antivortex pairs inside the condensate, generated on the opposite side with respect to the barrier's movement. Phase-slippage mechanisms are responsible for the emergence of Shapiro steps: in this phenomena the relative phase ϕ between the two reservoirs changes by $2\pi n$ each modulation period, by jumping across n local minima of the tilted washboard potential, as discussed in Sec. 1.6.4. We want to prove that the

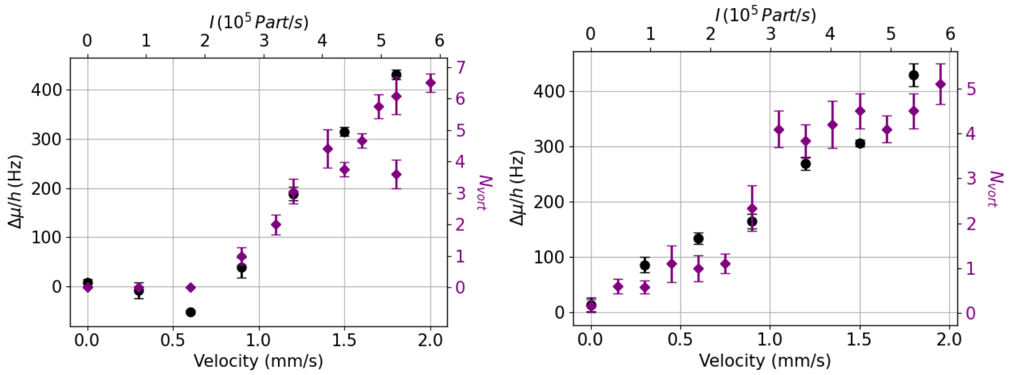

(a) $N_{vort}, \Delta\mu$ vs v_0, DC driving

(b) $N_{vort}, \Delta\mu$ vs v_0, AC driving

Figure 4.14: *(a): Number of vortex N_{vort} (purple dots) as a function of the barrier's velocity v_0, in the case of a DC driving ($x_1 = 0\,\mu m$). The corresponding $\Delta\mu - v_0$ characteristic is reported on the same plot (black dots), which shows a typical DC Josephson behavior, where a finite $\Delta\mu$ is observed after exceeding the critical velocity v_c.*
(b): Number of vortex N_{vort} (purple dots) as a function of the barrier's velocity v_0, in the case of an AC driving ($x_1 = 1.6$, $\nu = 175\,Hz$). The corresponding $\Delta\mu - v_0$ characteristic, featuring Shapiro steps, is reported on the same plot (black dots): we observe in both cases that the behavior of the vortex number N_{vort} mimics the behavior of the $\Delta\mu$.

Shapiro steps dynamics can be traced back to the formation of vortex pairs within the superfluid, both occurring during phase slips processes. In order for this assumption to be true, the number of vortices N_{vort} observed at the end of the Josephson dynamic as a function of speed v_0 should have a similar structure to the measured $\Delta\mu$-v_0 characteristics, exhibiting a step-like behavior. In the case of a constant driving (DC Josephson effect), shown in Fig. 4.14 (a), we observe that the number of emitted vortex N_{vort} as a function of the barrier's velocity v_0 has the same phenomenological behavior of the respective $\Delta\mu - v_0$ curve: a non-zero vortex number is measured when the driving velocity (current) is greater than the critical velocity (current) v_c (I_c) of the system. This phenomenon helps to relate the Josephson dynamics with the creation of excitations within the superfluid: in our system, the development of a non-zero $\Delta\mu$ during the driving can be associated with the emission of quantized vortices, which start to nucleate in the cloud when the Landau's critical velocity for superfluidity is exceeded. On the other hand, when we apply an alternating current $I(t)$ (which expression is described by Eq. (4.3)) that allows for the observation of Shapiro steps, the behavior of the vortex number as a function of the barrier's velocity becomes more complex. Similar to the DC case, the $N_{vort} - v_0$ curve follows the same trend of the underlying chemical potential imbalance characteristic, as observed in Fig. 4.14 (b): in particular, the number of vortices exhibits almost a step-like structure, similar to the one measured when probing the $\Delta\mu - v_0$ curve, where Shapiro steps emerge. This phenomena can be explained in terms of the phase slippage processes, occurring in the framework of the tilted washboard potential $U(\phi)$, shown in Eq. (1.98), employed for describing the relative phase ϕ dynamics. In particular, whenever the relative phase jumps between two successive minima of the washboard potential due to an alternate driving current, its value must change by 2π, resulting in the creation of a Shapiro step in the $\Delta\mu - v_0$ characteristic: in our system, this process is accompanied by the emission of a vortex dipole, being constituted by a vortex-antivortex pair with opposite winding number w. We can corroborate this observation by noting that in Fig. 4.14 (b) the measured vortex number N_{vort} on the first Shapiro step ranges between 1 and 2 ($\sim$ 1 vortex dipole), while on the second step roughly 4 vortices ($\sim$ 2 vortex dipoles) are present. This behavior, together with the step-like structure exhibited by the vortex number as a function of the driving velocity of the barrier, seems to confirm the presented theory: the emergence of Shapiro steps is correlated with vortex dynamics in our experimental system, as the observation of a quantized plateau is always associated with the nucleation of a finite number of vortex dipole.

4.5 Shapiro steps in Unitary Fermi gas

Previously we discussed the emergence of Shapiro steps in the $\Delta\mu - I$ characteristic of our superfluid Josephson junction, occurring when an alternating current $I(t) = I_{DC} + I_{AC}\,\sin(2\pi\nu t)$ is injected inside the system. The chemical potential difference has been shown to jump approximately by $h\nu$ between nearby plateaus having constant $\Delta\mu$ (Tab. 4.2, Fig. 4.9 , Fig. 4.12), as predicted by Eq. (1.107). Up until now, in our measurements we always employed a ^{6}Li gas in the weakly repulsive regime ($1/k_F a \gg 1$) where atoms bound together in pairs to form Feshbach molecules, creating a BEC superfluid. In the present section we briefly show the phenomenon of Shapiro steps occurring in the strongly interacting case ($1/k_F a \sim 0$), where our atomic Josephson junction contains a Unitary Fermi gas of ^{6}Li: in this particular regime of the BEC-BCS crossover, the superfluid is made up of short-distance Cooper pairs. Regarding the $\Delta\mu - I$ characteristic, measured by injecting an AC current inside the junction, we expect that the height of the steps shouldn't depend on the particular interaction regime considered but only on the modulation frequency ν. In fact, Shapiro dynamics is the direct consequence of a synchronization phenomena, occurring between the external driving (characterized by a frequency ν) and the phase velocity $\partial\phi/\partial t$, regardless of the nature of interparticle interactions. In conclusion, we expect to observe nearby Shapiro steps separated by a chemical potential difference of about $\Delta\mu \sim h\nu$ also for a Josephson junction made-up of a Unitary Fermi gas. The measurements are made as follows: an atomic Josephson junction of linear size $125 \times 17.5\,\mu\mathrm{m}^2$ is created following the procedure described in Sec. 2.1, containing a ^{6}Li superfluid in the Unitary regime. This strongly-interacting gas is realized by keeping the magnetic field to a value of about $B \sim 690\,\mathrm{G}$ during the ultracold gas realization, in order to employ the broad Feshbach resonance located at 696 G, occurring between the $|1\rangle - |3\rangle$ hyperfine states, as reported in Fig. 2.3. The mean number of particles trapped within the junction accounts to $N \sim 20 \cdot 10^3$ atoms, resulting in a chemical potential of approximately 5 kHz, which is calculated via Eq. (2.8). Since for the same experimental conditions (namely, system size $L_x \times L_y$ and atom number N) the chemical potential in the UFG case is of order of $\mu_{UFG} \sim 5 \cdot 10^4$ Hz, which is higher than the corresponding chemical potential in the BEC regime ($\mu_{BEC} \sim 10^3$), the applied laser power is set to a value of $P_{DMD} = 650$ mW: this way, the corresponding barrier height to chemical potential ratio is calculated to be about $V_0/\mu \sim 1.4$, comparable with the values employed for the various BEC measurements at $P_{DMD} = 130$ mW, ensuring we are in the Josephson tunneling regime.

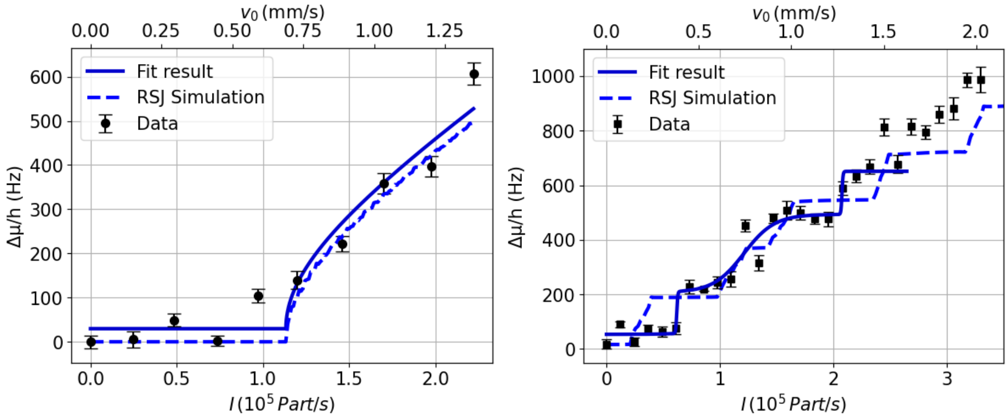

(a) $\Delta\mu$ vs I, DC driving **(b)** $\Delta\mu$ vs I, AC driving

Figure 4.15: *(a): Experimental data in the case of a DC driving, reported together with its corresponding curve fit and numerical simulation, effectuated through Eq. (1.94), for a UFG superfluid Josephson junction.*
(b):Experimental data in the case of a AC driving, reported together with its corresponding curve fit and numerical simulation, effectuated through Eq. (4.6). Both measurements are taken with driving parameters set as $\nu = 175$ Hz and $x_1 = 0,2\,\mu m$, while the driving time of 17 ms.

The measurements are carried out exactly as described in Sec. 4.3: the optical barrier is set into a modulated motion within the junction, so that its trajectory results described by Eq. (4.1): the modulation's parameters are chosen as $\nu = 175$ Hz, $x_1 = 2\,\mu$m and $N_{Cycles} = 3$. The absorption imaging is carried out after a driving time of $t_{barr} = 17$ ms, for different values of the barrier's velocity v_0, in order to extract the $\Delta\mu - I$ curve from Eq. (4.2). Measurement results for both the DC curve and its corresponding AC curve are reported in Fig. 4.15, together with their relative curve fits (blue solid lines), effectuated by fitting Eq. (1.94) and Eq. (4.6) respectively: we also report the numerical simulations of the RSJ model (blue dashed lines), plotted above the experimental data. We also report in Tab. 4.3 the fit results for the steps height $\Delta\mu_{S_i}$ of the first three Shapiro steps shown in Fig. 4.15. The measured values for the various step height are comparable with the expected height (in frequency units) of 175 Hz: we can further corroborate this statement by plotting in Fig. 4.16 the three steps height (with respect to $\Delta\mu = 0$) together with the straight line $f(n) = n \cdot \nu$, where n is the step number.
We observe that the plotted curve is compatible with the measured data within

Table 4.3: *Fit results for the first, second and third step height* $\Delta\mu_{S_i}$*, obtained by fitting Eq. (4.6) to the experimental data reported in Fig. 4.15 (a).*

Step number	$\Delta\mu_{S_i}$ (Hz)
1	153 ± 46
2	286 ± 55
3	158 ± 25

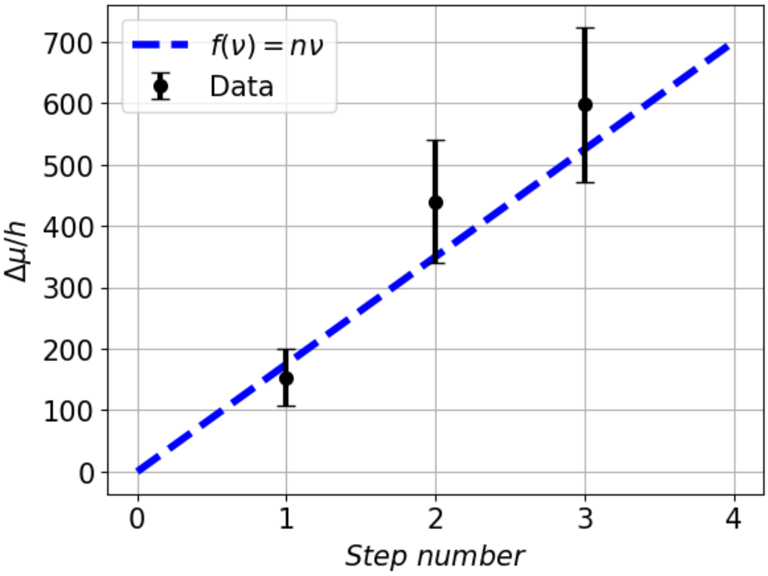

Figure 4.16: *Measured results for the first, second and third step reported in Fig. 4.15 (b). The nth step is obtained by summing together the previous steps, in order to obtain the total height with respect to* $\Delta\mu = 0$*. A straight line described by* $f(n) = n\nu$ *is plotted underneath, where* n *is the step number while* $\nu = 175$ *Hz is the modulation frequency.*

the latter's error bar, confirming our initial assumption; Shapiro steps also occur in the strongly-interacting regime of the crossover, where the chemical potential difference jumps by $\Delta\mu_S = h\nu$ between nearby plateaus.

Conclusions

In this thesis we investigated the behaviour of an elongated ^{6}Li superfluid Josephson junction, made-up of atoms in the weakly-repulsive BEC regime, probing its transport properties when an alternating atomic current $I(t)$ is applied: moreover, we also characterized the well-known DC and AC Josephson effects within the system, extracting noteworthy quantities as the critical current I_c and the Josephson oscillation frequency ν as a function of both the junction's size and the trapping strength. If a thin optical barrier is displaced according to a modulated trajectory $x(t)$, *Shapiro steps* appear inside the junction's $\Delta\mu - I$ characteristic, occurring due to a synchronization phenomena between the driving frequency ν and the relative phase velocity $\partial\phi/\partial t$. Quantized plateaus are clearly observed in the measurements shown in Sec. 4.3, where chemical potential difference jumps are found to be compatible with the theoretically expected value presented in Sec. 1.6.4: in particular, the height of the n-th Shapiro step is measured to depend solely on the modulation frequency via $\Delta\mu_{S_n} = nh\nu$. This behavior has been confirmed for both the first and second step, as shown in Figs. 4.9 (a) and 4.12. We also measured the number of observed quantum vortices at the end of the barrier's displacement, as a function of its velocity v_0, in order to relate the emergence of Shapiro steps with the nucleation of vortex dipoles in our system: in particular, we found out that whenever a Shapiro step is measured, this phenomena occurring due to *phase-slip* processes, it is always accompanied by the creation of a vortex-antivortex pair within the superfluid. The device investigated in this thesis work constitutes one of the first examples of periodically driven many-body systems realized in ultracold atoms physics: these circuits represent important prospects for successive studies, as DMD optical setups allow for the arbitrary manipulation of optical potentials. For example, synchronization phenomena could be probed in more complicated arrays of Josephson junctions, these devices being disposed either side by side or in annular configurations [65]. In particular, we could couple together two rectangular superfluid junctions having different lengths, and modulate both of them by injecting the same atomic current to study their eventual interactions. Another possibility is given by the realization of ring-shaped potentials through the fine tuning of optical potentials: collective phenomena could be investigated by sectioning such a device in different sectors, each one having its corresponding Josephson barrier, and by modulating simultaneously every optical barrier with the same trajectory in order to disclose synchronization processes The *Kuramoto-Daido* model, describing the dynamical behavior of a large set of coupled harmonic oscillators, has already been employed in the study of superconducting Josephson junctions arrays [66, 67]. Regarding our physical system, this model could be applied in order to investigate the dynamics across the various interacting regimes of the BEC-BCS crossover, even in the presence of disordered couplings between the device's links [68, 69]. In this thesis work we have also briefly shown how the dependence of the steps height on the modulation frequency ν is the same regardless of the particular interaction regime considered (UFG or BEC). Successively to this thesis work, the Shapiro step phenomena has been successfully measured in our laboratory with strongly-interacting *Unitary Fermi gas* Josephson junctions, presenting the same experimental results reported in this thesis ($\Delta\mu_{S_n} = nh\nu$). In this particular regime of the crossover, as in the weakly-interacting BEC regime, the equation of state (*EOS*) describing the relationship between the particle's density n and the chemical potential difference $\Delta\mu$ is well known: unfortunately, the *EOS* has not yet been determined analytically in the intermediate regime of the BEC-BCS crossover, where its calculation still constitutes a formidable task. In analogy with superconducting physics, where Shapiro steps are employed in Josephson voltage standard devices, we could use this phenomena in order to accurately measure the bias chemical potential difference $\Delta\mu$ between a superfluid junction's reservoirs as a function of the external magnetic field: this approach would be particularly useful for allowing an experimental determination of the *EOS* across the whole BEC-BCS crossover.

Appendices

Appendix A

Laser cooling and trapping

When interacting with a quasi-resonant light source a two-level atom experiences radiative forces, which can be exploited to modify the atom's dynamics. In ultracold atoms experiments two remarkable applications of these forces stand out: laser trapping and laser cooling, which constitute fundamental tools for investigating low-temperature quantum gases. First and foremost, laser cooling is necessary for slowing down the particles of the cloud, eventually obtaining a degenerate gas where many-body effects set in, depending on the particular quantum statistic describing the system. Laser trapping techniques are subsequently employed in order to spatially localize and sometimes to further slow down the atomic cloud. In Sec. A.1 we will discuss about radiative forces and how they arise in the context of atom-light interaction. The following Sec. A.2 is dedicated to describing the major applications of radiative forces in ultracold atoms experiments, namely laser cooling and laser trapping techniques, for the general case of a two-level atom.

A.1 Radiative forces

The concept of a "mean force" due to an external laser light acting on a two-level atom in the position $\vec{R}$ is valid only when the spread of the atomic wave-packets is sufficiently small, which means that the uncertainties ΔR and ΔP must satisfy the following conditions:

$$\begin{cases} \Delta R << \lambda \\ k\,\Delta P << M\gamma \end{cases} \tag{A.1}$$

where λ is the laser wavelength, while γ is the natural line width of the considered atomic transition. The inequalities reported in Eq. (A.1) must hold simultaneously with **Heisenberg's uncertainty principle**, $\Delta R\,\Delta P \geq \hbar$, and ensure that the atom's position is well localized within the laser beam. We can derive a force operator $\hat{F}$, in the quantum-mechanical framework, by considering the time derivative of the center-of-mass momentum operator $\hat{P}$, associated with the atomic motion. This derivative is given by Heisenberg's equation:

$$\hat{F} = \frac{d\hat{P}}{dt} = \frac{1}{i\hbar}[\hat{P}, \hat{H}] \tag{A.2}$$

where $\hat{H}$ is the full hamiltonian of the system:

$$\hat{H} = \hat{H}_{CM} + \hat{H}_r + \hat{H}_{A-L} + \hat{H}_{A-R} \tag{A.3}$$

which takes into account both the atomic ($\hat{H}_{CM}$) and electronic ($\hat{H}_r$) dynamics, as well as the atom interactions with the laser wave ($\hat{H}_{A-L}$) and the reservoir ($\hat{H}_{A-R}$) of initially empty modes of the electromagnetic field. In order to obtain the mean force acting on the atom due to the external radiation field we should consider the average of Eq. (A.2): the only term of $\hat{H}$ which gives a non-zero averaged commutator is the interaction term $\hat{H}_{A-L} = -\vec{d}\cdot\vec{E}$, describing the coupling between the atomic dipole $\vec{d}$ and the electric field $\vec{E}$ of the laser. In the following we will consider the laser field to be described by an oscillating function which amplitude depends on position, such that:

$$E(\vec{R}) = \mathcal{E}(\vec{r})\, cos(wt + \phi(\vec{R}))\, \hat{e} \tag{A.4}$$

where we suppose that $\phi(\vec{R}) = \vec{k}\cdot\vec{R}$. Taking the expectation value of Eq. (A.2), whose calculation is carried out with the density matrix formalism of quantum statistical mechanics, we obtain the following expression for the mean force acting on the atom [35]:

$$\langle\vec{F}\rangle = -\frac{1}{2}\frac{\hbar\,\delta\,\Omega(\vec{R})\,(\vec{\nabla}\Omega(\vec{R}))}{\delta^2 + \gamma^2/4 + \Omega^2(\vec{R})/2} + \frac{\hbar\,\vec{k}\,\gamma\,\Omega^2(\vec{R})/4}{\delta^2 + \gamma^2/4 + \Omega^2(\vec{R})/2} = \vec{F}_{dip} + \vec{F}_{rad} \tag{A.5}$$

where $\vec{k}$ is the wave vector of the laser wave, $\delta = w_L - w_0$ is the *detuning* between the (angular) frequency of the atomic transition w_0 and the laser frequency w_L, while $\Omega(\vec{R})$ is the *Rabi frequency*, defined as:

$$\Omega(\vec{R}) = -\frac{\mathcal{E}(\vec{R})\cdot\langle e|\,\vec{d}\,|g\rangle}{\hbar} \tag{A.6}$$

where $\mathcal{E}(\vec{R})$ is the electric field amplitude of the laser beam, while $\langle e|\,\vec{d}\,|g\rangle$ is the matrix element of the dipole operator d between the excited and ground states of the atomic transition. The first term $\vec{F}_{dip}$ of Eq. (A.5) constitutes the *optical dipole force*, dominating for high values of δ, while the second term $\vec{F}_{rad}$ is the *dissipative force* due to radiation pressure, which instead dominates at resonance ($\delta = 0$), describing absorption processes between an atom and the photons that constitute the laser beam. Both contributions are employed for different reasons in ultracold atoms experiments: the radiation pressure force is mostly used in laser cooling processes, while trapping mechanisms are usually based on the optical dipole force.

A.2 Laser cooling and trapping techniques

The physical mechanism behind laser cooling, where the motion of the atom is slowed down thanks to interactions with light, is the transfer of the momentum of a laser photon to the atom. Due to *Doppler effect*, a two-level atom in the energy ground state E_0, moving with an initial velocity v_0 against a counter-propagating laser beam with frequency $\nu = \omega/2\pi$, will perceive an angular frequency $\omega' \neq \omega$ equal to [35]:

$$\omega' = \omega\frac{v_0}{c} + \omega = k\,v_0 + \omega \tag{A.7}$$

Resonance condition occurs if the angular frequency separation between the considered atom levels $\omega_0 = (E_1 - E_0)/\hbar$ is equal to the perceived ω': as a consequence a photon is absorbed by the atom, which transitions to the excited state E_1. This process causes the atom to slow down to a smaller velocity v_f due to momentum conservation, $Mv_0 - \hbar k = Mv_f$. After a time scale $T_{int} \propto \gamma^{-1}$, much smaller than the one associated with the motion of the atom in the laser field, $T_{int} << T_{ext} \sim (\hbar\, k^2/M)^{-1}$, a photon is spontanously emitted from the atom in a random direction: this results in the de-excitation of the atom to the ground state and to another change of its momentum. Since spontaneous emission phenomena occurs in random directions, the total recoil due to a macroscopic number of emissions averages to zero, unaffecting the mean velocity of the atom. On the other hand, absorption processes always occur in the same direction, fixed by the wave vector $\vec{k}$ of the laser beam, causing a significant decrease of the atom velocity over many cycles of absorption/emission. The procedure just described to slow down an atom is only possible around resonance, where absorption processes are most likely to occur. However, the speed of the atom gradually decreases over time due to continuous interactions with photons, causing a departure from resonance conditions, thus suppressing the absorption of photons. Laser cooling techniques used in experiments, such as *Doppler cooling* or *Zeeman cooling*, are designed to overcome this problem.

Zeeman cooling

The application of an external magnetic field causes a separation of the atomic energy levels known as Zeeman effect, due to the interaction between the spin of the atom and the field itself; the good quantum number in this case becomes the projection of the total angular momentum $F = I \oplus J$ along the quantization axis, m_F, which can take values in the range $m_F \in \{-F, -F+1, ..., F-1, F\}$, where I is the nuclear spin while $J = L \oplus S$ is the total electronic angular momentum. The Zeeman cooling technique employs a magnetic field $B(x)$ which varies in space, such that the energy shift of atomic levels compensates for the decrease in speed of the atom, keeping the process at resonance while the sample is slowed [35]:

$$\omega_0 + \frac{\Delta\mu}{\hbar} B(x) = k\, v(t) + \omega \tag{A.8}$$

where $\omega_0 = (E_1 - E_0)/\hbar$ is the level separation in angular frequency at zero field, while $\Delta\mu = \mu_1 - \mu_0$ is the difference in magnetic momentum of the levels. For large laser intensities $\Omega \gg \gamma$, near resonance, the component of the radiative force $\vec{F}_{rad}$ related to the radiation pressure in Eq. (A.5) saturates to a maximum constant value, $\vec{F}_{rad} \approx \hbar\,\gamma\,\vec{k}/2$, thus implying a constant deceleration of the atom. Solving Eq. (A.8) by using the formulas for an uniformly accelerated motion we obtain the requested expression for the magnetic field $B(x)$ as a function of the position:

$$B(x) = \frac{\hbar\, k\, v_0}{\Delta\mu} \left(\sqrt{1 - \frac{x}{L}} - 1 \right) \tag{A.9}$$

where $L = v_0^2/2a$ is the braking distance, k is the wave vector of the laser and v_0 is the initial velocity of the atom. The magnetic field reported in Eq. (A.9) is the one necessary to maintain the absorption process at resonance during the deceleration of the atom, and can be generated by a set of solenoids. Experimental devices whose operation is based on the Zeeman cooling are known as Zeeman slowers: in our experimental setup, a Zeeman slower is employed as the first device for slowing down the atomic beam, right before the magneto-optical trap.

Doppler and sub-doppler cooling

Let us consider a two-level atom moving with velocity v in the field produced by two counter-propagating weak laser beams ($\Omega \ll \gamma$) with angular frequency ω_L, as illustrated in Fig. A.1, such that the process is red detuned ($\delta = \omega_L - \omega_A < 0$) with respect to the atomic transition, $\hbar\omega_A = E_1 - E_0$.

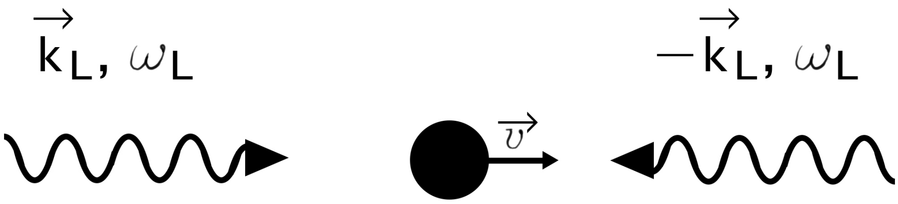

Figure A.1: *Experimental setup for Doppler cooling. In the reference frame of the atom, the frequencies of the two laser waves are Doppler shifted in a different way, such that the atom experiences counter-propagating travelling waves with frequencies* $\omega' = \omega \pm k_L v$.

The respective polarizations of the lasers are chosen to be orthogonal to each other in order to avoid interference phenomena. The total force acting on the atom due to radiation pressure can be calculated by expanding the expression of the dissipative force $\vec{F}_{rad}$ in Eq. (A.5) in a power series of v near zero, considering the contributions of both lasers. In the 1-D case we obtain:

$$F_{rad} = F_{k_L} - F_{-k_L} = -\alpha\, v + O(v^3) \tag{A.10}$$

where α is the damping coefficient:

$$\alpha = 8\,\hbar\, k^2\, s \frac{|\delta|/\gamma}{(1 + 4\,\delta^2/\gamma^2)^2} \tag{A.11}$$

and $s = 2\,\Omega^2/\gamma^2$ is the saturation parameter. The maximum value of the damping coefficient α is obtained when $\delta = -\gamma/2$, such that $F_{rad} \sim -\hbar\, k^2\, s\, v$ is the maximum force which can act on the atom in this setup. As shown in Fig. A.2 there is a finite velocity range around zero for which the radiative forces of the two red-detuned and counter-propagating waves act as an effective damping force. This velocity interval is centered around the Doppler capture velocity $v_{dopp} = \gamma/k_L$, which for alkali atoms is of order of 10^{-1} m/s. The minimum temperature that can be reached with Doppler cooling, estimated to be of order of $100\,\mu$K, is constrained by two competing contributions: that

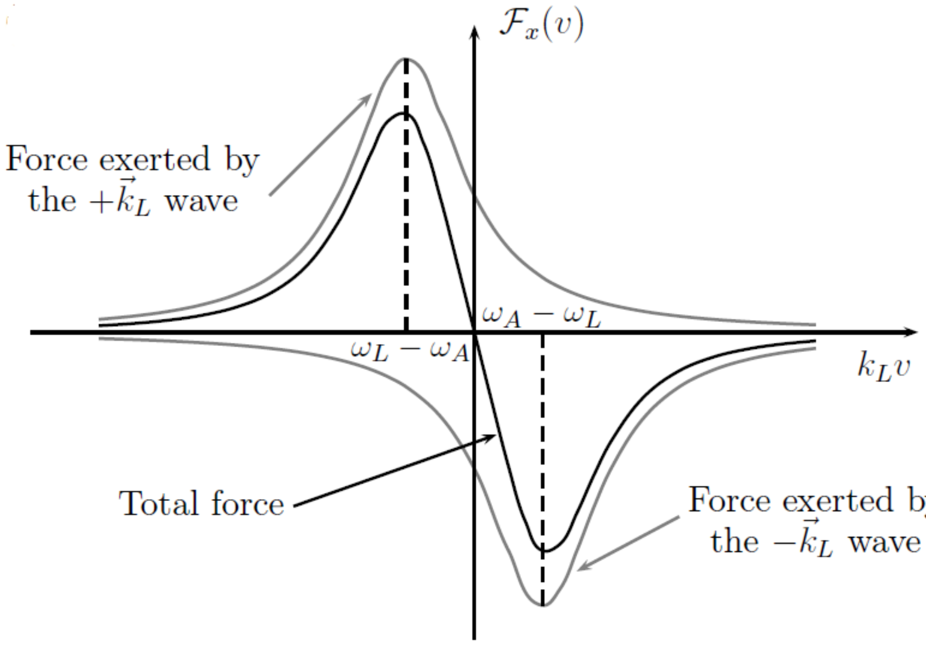

Figure A.2: *Radiation pressure forces acting on the atom as a function of its velocity in the Doppler cooling setup. Darker plot represents the total dissipative force due to both laser beams, while the lighter ones represent the single contributions. A maximum/minimum occurs at resonance, when* $k_L v = \pm(\omega_L - \omega_A)$. *Figure taken from Ref. [35].*

due to absorption of photons, which tends to cool the system, and that due to the fluctuation in the number of absorbed photons, which tends to heat the system. In reality, during experiments temperatures much lower than those expected a priori can be reached. This is due to the presence of additional effects which have been neglected, such as polarization gradients or optical pumping, which constitute the physical mechanisms underlying the sub-Doppler Sisyphus cooling, where the temperatures achievable experimentally are of the order of $10\,\mu$K. The setup described above can also be adapted to three dimensions, where three pairs of counter-propagating laser beams out of resonance, detuned towards the red, are employed. In this case, the structure of light which is formed is called an optical molasses.

Magneto-optical traps

The working principle of one-dimensional magneto-optical trap (MOT) consists of two counterpropagating laser beams oscillating at the same frequency ω_L, with opposite circular polarizations σ^+ and σ^-. Both beams are red-detuned with respect to the atomic transition, $\delta = \omega_L - \omega_0 < 0$. Furthermore a spatially inhomogeneous magnetic field, $B \sim B_0\, x$, modifies the atomic energy levels through the Zeeman effect. We also assume the angular momentum of the ground and excited states g and e, involved in the trapping, to be respectively $J_g = 0$ and $J_e = 1$. Because of the selection rules in quantum mechanics, when the atom absorbs a photon with polarization $\sigma^\pm$ it will go into an excited state such that $\Delta m = \pm 1$, where m is the projection of the angular momentum onto the quantization axis. This situation is represented in Fig. A.3.

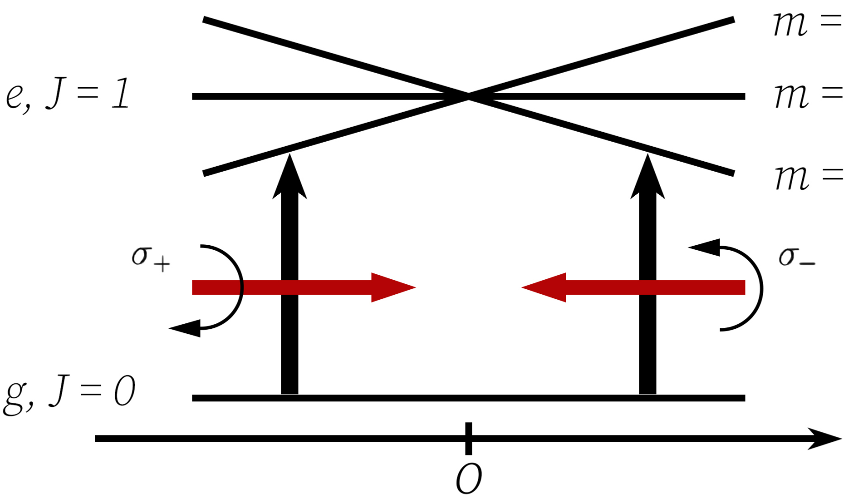

Figure A.3: *Working principle of the magneto-optical trap (MOT) using an optical transition from a ground state with $J = 0$ to an excited state with an angular momentum of $J = 1$. Here $J = L \oplus S$ is the total angular momentum of the electrons, neglecting hyperfine structure. The two counter-propagating laser beams, are σ^+ and σ^- polarized, and they have the same intensity and frequency. A gradient of the magnetic field creates a situation where atoms feel a restoring force towards the zero magnetic field position.*

At the center of the trap O, the magnetic field is zero: by symmetry the two radiation pressure forces exerted by the lasers at this location have the same magnitude, but opposite direction, so that an atom at O feels no net force. For an atom to the left (right) of the center of the trap, the σ^+ (σ^-) polarized beam ($m = 0 \to m = +1\,(-1)$) is closer to the resonance than the other, and its radiation pressure dominates the dynamics of the system: the atom experiences a net force towards the center of the trap, regardless of the side. One therefore achieves a stable trapping around O. The total force experienced by the atom in the trap can be calculated with the same procedure of Eq. (A.10), expanding the total radiation pressure force in a power series of v near zero:

$$F = F_{\sigma^+} - F_{\sigma^-} \approx -\alpha\, v_x - k\, x \tag{A.12}$$

where α is the friction coefficient introduced before, while K is the system "stiffness":

$$K = 2\, k_L\, \mu_e\, B_0\, s \frac{|\delta|\,\gamma}{\delta^2 + \gamma^2/4} \tag{A.13}$$

where μ_e is the magnetic moment of the excited state, while s is the saturation parameter. The total force in Eq. (A.12) describes the motion of a damped harmonic oscillator, with a characteristic oscillation frequency of $\omega = \sqrt{K/M}$, where M is the atom's mass. Therefore, magneto-optical traps are used both for laser cooling and for laser trapping: temperatures achievable in these devices range from few μK to $1\,m$K depending on the atomic species and the MOT parameters. Such a configuration can be extended to three dimensions, where the magnetic gradient is usually made with a pair of coils in anti-Helmholtz configuration [52].

Optical dipole traps

The optical dipole force introduced in Eq. (A.5) is a conservative force, and can be thus associated with a potential energy U_{dip}:

$$U_{dip}(\vec{R}) = \frac{\hbar\,\delta}{2} \log\left(1 + \frac{\Omega^2(\vec{R})/2}{\delta^2 + \gamma^2/4}\right) \tag{A.14}$$

which satisfies $\vec{F} = -\vec{\nabla} U_{dip}(\vec{R})$. When $\delta >> \Omega, \gamma$ the optical dipole potential reported in Eq. (A.14) can be expanded in powers of Ω, obtaining, at first order [35]:

$$U_{dip}(\vec{R}) \approx \frac{\hbar\,\Omega^2(\vec{R})}{4\,\delta} \tag{A.15}$$

such that for high values of the *detuning* δ the potential energy experienced by atoms due to a laser field is directly proportional to the laser intensity, since $\Omega^2(\vec{R}) \propto I(\vec{R})$. Moreover, the shape of the potential curve depends on the particular intensity profile employed: real laser beams are well described in terms of Gaussian beams, whose intensity profile can be expanded in terms of the Hermite-Gauss normal modes [70]. Thus, the optical potential acting on a two-level atom due to a single laser field has approximately a Gaussian shape and depends on the sign of the detuning δ, as reported in Fig. A.4.

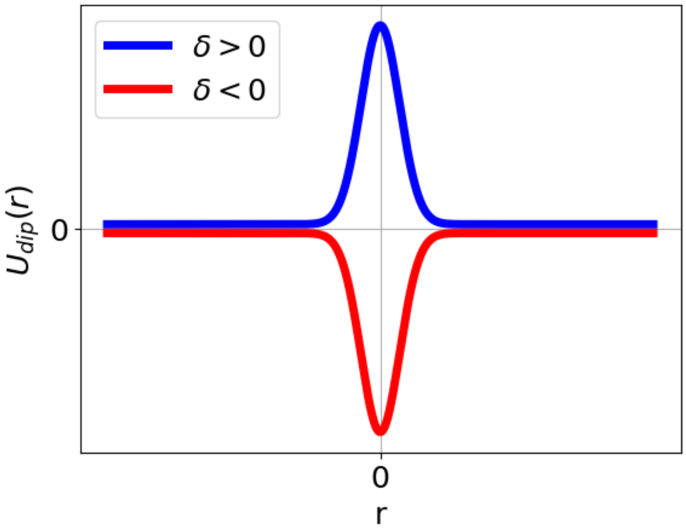

Figure A.4: *Profile of the optical dipole potential as a function of position, where $r = 0$ represents the center (of the radial coordinate) of the laser beam. Its nature depends on the sign of the detuning δ: the potential is attractive for $\delta < 0$, and repulsive for $\delta > 0$.*

Optical dipole traps used in experiments employ red detuned beams with $\delta < 0$, such that the potential is attractive and the atom can be trapped in the intensity maximum of the laser (high intensity seeking). On the contrary, for blue detuning ($\delta > 0$), the force exerted on the atoms tends to push them away from high intensity regions (low intensity seeking). If the thermal energy of the trapped cloud is small compared to the depth of the trap, $k_B T << U_0$, we can expand the optical dipole potential reported in Eq. (A.15), supposing a Gaussian intensity profile, in order to show that atoms experience an harmonic confining potential [35]:

$$U_{dip} \approx U_0 \left[-1 + \frac{2r^2}{w_0^2} + \frac{z^2}{z_r^2} \right] = -U_0 + \frac{1}{2} m\, w_\perp\, r^2 + \frac{1}{2} m\, w_z^2\, z^2 \tag{A.16}$$

where $r = \sqrt{x^2 + y^2}$ is the radial coordinate, w_0 is the beam waist, which is the minimum transverse dimension of the beam, while $z_r = \pi\, w_0^2 / \lambda$ is the *Rayleigh length*. The optical dipole trap generated by a single focused beam can be very anisotropic, since $w_z / w_\perp \approx \lambda / w_0 << 1$.

Evaporative cooling

The most efficient cooling technique, capable of bringing the atomic cloud to temperatures of the order of $100\, n\mathrm{K}$, is evaporative cooling. To describe its functioning, suppose we have an atomic sample, trapped in a potential with non-infinite depth U_0, not in thermal equilibrium. Particle collisions lead to the thermalization of the system, at certain temperature T: the most energetic atoms, which are those that possess an energy comparable to U_0, are expelled from the trap, and only the coldest particles remain trapped in the potential. By lowering the trap depth to a different value $U_0^{'} < U_0$, the system thermalizes again due to interatomic collisions, cooling down to a lower temperature $T^{'} < T$ which depends on the trap depth $U_0^{'}$. The evaporation process stops when the temperature of the trapped sample decreases to values such that $k_B T \ll U_0^{'}$, since elastic collisions can no longer transfer enough energy to allow atoms to leave the trap. This mechanism is reported in Fig. A.5.

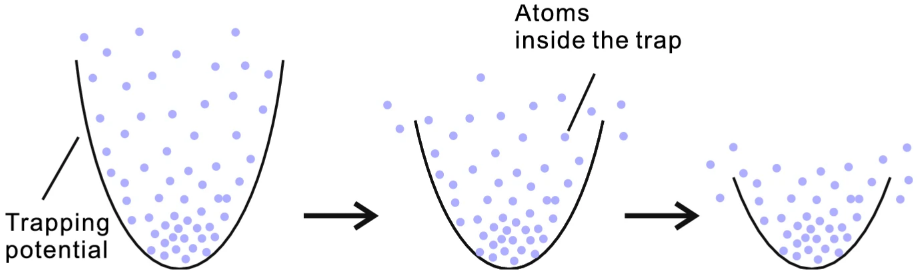

Figure A.5: *Representation of the evaporative cooling process, where the depth U_0 of the trapping potential is progressively lowered: as a consequence, the most energetic particles are expelled from the trap. Thermal equilibrium is subsequently restored through particle collisions. Figure taken from Ref. [71].*

The net result is that while the total population in the trap decreases, so does the mean energy of the remaining population. This process can be repeated many times, gradually reducing the height of the trap, allowing to reach temperatures at least one order of magnitude lower than those obtainable with sub-Doppler cooling. The only physical constraint in this technique is related to the number of trapped atoms, which decreases with each cycle of evaporation, so that beyond a certain point the density in real space is so low that collisions are suppressed, and the system does not thermalize easily. In our experiment the forced evaporation process is carried out in an optical dipole trap, where we can lower the trap depth by reducing the intensity of the lasers. As already pointed out in Sec. 1.3, ultracold fermionic gases composed of identical particles do not experience collision phenomena due to Pauli's exclusion principle, and therefore cannot be cooled by evaporative cooling techniques, where the system is thermalized through collisions. To overcome this problem, in our system we employ a mixture of ^{6}Li atoms in different Zeeman sublevels, as explained in Sec. 2.1.

Ringraziamenti

In questa sezione nascosta del lavoro di tesi, presente solamente in alcune copie (sennò la commissione giustamente mi boccia) vorrei portare i miei saluti personali a molte persone. La mia vita privata è stata indubbiamente arricchita dalla loro presenza, **pertanto inizierò una lista innecessariamente lunga per ringraziare tutti e nessuno potrà fermarmi**.
Vorrei ringraziare la mia famiglia (Renzo, Lorella, Luana, Floriano, Andrea, Francesca) per avermi supportato negli ultimi anni, e per avere creduto in me. In particolare, ringrazio Renzo e Lorella per avermi dato la possibilità di raggiungere questo risultato. Sperando, un giorno, di poter rendere un figlio orgoglioso del proprio genitore, come avete fatto voi.
Vorrei ringraziare il gruppo di ricerca con il quale ho affrontato l'esperienza di tesi (Giulia, Giacomo, Nicola, Diego, Marcia). Augurandomi che le nostre strade si possano incrociare spesso in futuro, a dispetto della mia scelta di percorrere la strada teorica.
In particolare, ringrazio Giulia Del Pace per essersi dimostrata una persona umanamente squisita, un'abilissima fisica ed un'eccellente relatrice, dalla quale ho indubbiamente imparato moltissimo del lavoro di Fisico.
Ringrazio anche Giacomo Roati per i preziosi consigli, di grande aiuto per decidere quale strada percorrere nel mio immediato futuro, e per avermi dato la possibilità di lavorare a questo bellissimo progetto.
Vorrei ringraziare il gruppo di Kendo e Kenjutsu del Ken-Shin-Kan (Stefano Z., Gianni, Francesco, Federico, Alessandro, Stefano A., Barbara, Rosa, Andrea), che mi ha accompagnato in questi lunghi anni nel mio percorso accademico, fra scherma e particelle microscopiche.
A Francesco, Federico, Alessandro, Stefano A., Andrea e Barbara per essere stati preziosi compagni di pratica e buoni amici, oltre che aspri rivali.
A Giovanni Comoretto, per avermi aiutato sei anni fa a scoprire questa bellissima disciplina, portandomi a studiare una forma di scherma che mi ha sempre affascinato.
A Stefano Zancaner, il cui metodo didattico applicato a Kendo-Kenjutsu ha indubbiamente impattato sulla mia vita (marziale, sportiva e personale), forse molto più di quanto in questo momento io riesca a comprendere.
Ringrazio le Flora's Angels (Matilda, Emma, Clara, Angela, Sofia, **Pietro**) per essersi sempre dimostrate ottime amiche. Per essermi state recentemente accanto ed avermi aiutato ad affrontare me medesimo, di fronte al dolore sentimentale. Di fronte agli eventi inaspettati della vita.
RIngrazio le persone conosciute a pallavolo (Alessia, Camilla, Martina, i vari all'epoca Pink Volley): avete reso questo anno difficile molto più tollerabile, e ricco.

Ringrazio Sara Marino per avermi fatto passare un bellissimo anno. Sperando che in futuro le nostre strade possano reincrociarsi, con connotazioni diverse.
Ringrazio Serena Vannacci: a dispetto dell'altalenante frequenza con la quale ci sentiamo, ti ritengo una delle persone più belle che conosca. Una delle più empatiche. Una delle più intelligenti.
A Riccardo, Marianna, Lorenzo, Ida, compagni ed ex compagni di università. Sebbene abbiamo scelto tutti strade diverse, auguro ad entrambi il migliore dei proseguimenti. Date sfocio al vostro talento, senza paura.
Vorrei ringraziare il gruppo delle dolomiti (Leonardo.P, Tommaso B., Andrea, Martina F., Marco, talvolta Luca P.) per avermi accompagnato in escursioni indimenticabili sul tetto d'Europa. Per aver condiviso con me una delle mie giornate più nere, da quando ho memoria. Per avermi risollevato da quest'ultima.
Ringrazio Leonardo Pierri per l'organizzione dei viaggi e per aver sempre dimostrato un innegabile maturità, ogniqualvolta avevo bisogno.
Ringrazio Luca Ponticelli per i bei ganci.
Ringrazio Andrea Guasti per il bell'albero.
Ringrazio Tommaso Benvenuti per le belle ultra.
Ringrazio Marco Bellezza per essersi dimostrato una persona incredibilmente sensibile e valida, forse molto più di quanto egli pensi.
Ringrazio Martina Feri per l'amicizia probabilmente più particolare degli ultimi anni: persona insospettabilmente dolce e supportiva quando hai bisogno, nonchè spirito guida dei distratti.
Ringrazio messer Francesco d'Onofrio per il viaggio in Giappone; probabilmente, una delle esperienze più belle della mia vita, che proverò sicuramente a replicare in futuro.
Ringrazio il mio gruppo di amici di sempre (Tommaso G. , Luca P., Leonardo G., Leonardo P., Lorenzo, Martina B., Giacomo, Ginevra, Matteo) per aver reso colorate le giornate della mia vita, da quando vi sono entrati, ognuno a tempo debito.
Ringrazio Matteo per essermi rimasto accanto, nelle nostre modalità, dalla pallacanestro in poi, persona per cui nutro una stima infinita.
Ringrazio la Ginevra per la sensibilità che ha dimostrato da quando ci conosciamo: a dispetto dei traumini, sei un'ottima persona, non dimenticarlo.
Ringrazio Giacomo per essere il detentore di expertise di "qualsiasi cosa ti serva" nel nostro gruppo: la persona più intraprendente del nostro gruppo.
Ringrazio Lorenzo per la **madre della miseria**, il "ti fidi di me" e le risata: il suo umorismo genuino rende migliore ogni giornata.
Ringrazio Martina per essere stata un'ottima amica, a suo personalissimo modo, della quale ho potuto apprezzare le recenti evoluzioni: persona con la quale ho avuto moltissimi alti e bassi, ma che è ancora nella mia vita.
Ringrazio Leonardo Pierri per aver generato (non creato) Speck^{TM}: stai occupando già tre righe della mia tesi di laurea e la cosa mi turba.
Ringrazio Leonardo, Tommaso e Luca, che conosco da sempre, per comporre il nucleo principale dei miei amici. Augurandomi che tutti trovino la loro felicità, insieme. Anche quando saremo eventualmente separati.
Ringrazio Leonardo per essermi vicino sin dalle scuole medie: sei una persona per me più preziosa di quanto io riesca probabilmente a farti capire, e ti voglio bene. Ricomincia pallavolo, pirla, che eri diventato bravino. Lo pensano tutti.

Ringrazio Luca per le risate, le partite a magic, ai picchiaduro, **il fatto di non masterarmi a DnD**: spero in futuro tu possa trovare la possibilità di realizzare i tuoi sogni.
In dirittura di arrivo, ringrazio Tommaso Guastini, il mio disagiato compagno di vita. Non ho molte parole da spendere nacchero, se non questo: sono incredibilmente orgoglioso di te, e forse, dico forse, dovresti iniziare ad esserlo anche te. Ringrazio infine Flora per essere stata, per sempre e fino ad oggi, la mia più grande alleata. A te auguro tutta la felicità che meriti.
Ciononostante ti maledico e che tu possa condividere le mie disavventure ed il mio disagio per il resto della mia vita MUAHAHAH.

Bibliography

[1] Chang C. Tsuei and John R. Kirtley. "Pairing symmetry in cuprate superconductors". In: *Reviews of Modern Physics* 72 (4 Oct. 2000), pp. 969–1016.

[2] S.G. Chung. "Spontaneous symmetry breaking in Josephson junction arrays". In: *Physics Letters A* 355.4 (2006), pp. 394–398. ISSN: 0375-9601. DOI: `https://doi.org/10.1016/j.physleta.2006.02.043`.

[3] B.D. Josephson. "Possible new effects in superconductive tunnelling". In: *Physics Letters* 1.7 (1962), pp. 251–253. ISSN: 0031-9163.

[4] M. Tinkham. *Introduction to Superconductivity: v. 1.* Dover Books on Physics (Dover Publications, Mineola, NY), 2004.

[5] P. W. Anderson and J. M. Rowell. "Probable Observation of the Josephson Superconducting Tunneling Effect". In: *Phys. Rev. Lett.* 10 (6 Mar. 1963), pp. 230–232.

[6] C. Gross and I. Bloch. "Quantum simulations with ultracold atoms in optical lattices". In: *Science* 357 (2017), pp. 995–1001.

[7] Luca Pezzè et al. "Quantum metrology with nonclassical states of atomic ensembles". In: *Reviews of Modern Physics* 90.3 (Sept. 2018). ISSN: 1539-0756.

[8] S. Inouye et al. "Observation of Feshbach resonances in a Bose-Einstein condensate". In: *nat* 392.6672 (Mar. 1998), pp. 151–154.

[9] Cheng Chin et al. "Feshbach resonances in ultracold gases". In: *Reviews of Modern Physics* 82.2 (Apr. 2010), pp. 1225–1286. ISSN: 1539-0756. DOI: `10.1103/revmodphys.82.1225`. URL: `http://dx.doi.org/10.1103/RevModPhys.82.1225`.

[10] Giancarlo Calvanese Strinati et al. "The BCS–BEC crossover: From ultra-cold Fermi gases to nuclear systems". In: *Physics Reports* 738 (Apr. 2018), pp. 1–76. ISSN: 0370-1573. DOI: `10.1016/j.physrep.2018.02.004`.

[11] Andrea Amico. "Probing the many body dynamics of ultracold repulsive Fermi gases of lithium atoms". PhD thesis. University of Firenze, 2009.

[12] Giacomo Valtolina et al. "Josephson effect in fermionic superfluids across the BEC-BCS crossover". In: *Science* 350.6267 (Dec. 2015), pp. 1505–1508. ISSN: 1095-9203.

[13] Wolfgang Ketterle and Martin W.Zwierlein. "Making, probing and understanding ultracold fermi gases". In: *La Rivista del Nuovo Cimento* 31.506 (July 2008), pp. 247–422. ISSN: 0393697X.

[14] R. Haussmann et al. “Thermodynamics of the BCS-BEC crossover”. In: *Physical Review A - Atomic, Molecular and Optical Physics, vol. 75, no. 2, pp. 1–22* (2007).

[15] Mohit Randeria, Wilhelm Zwerger, and Martin W. Zwierlein. *The BCS-BEC crossover and the unitary fermi gas.* Springer, 2012.

[16] Daniel Petter. “Spatial modulation of light for ultracold gas experiments with erbium atoms”. MA thesis. Faculty of Mathematics, Computer Science and Physics, University of Innsbruck, 2015.

[17] Luigi Amico et al. “Colloquium: Atomtronic circuits: From many-body physics to quantum technologies”. In: *Rev. Mod. Phys.* 94 (4 Nov. 2022), p. 041001. DOI: `10.1103/RevModPhys.94.041001`. URL: `https://link.aps.org/doi/10.1103/RevModPhys.94.041001`.

[18] A. Smerzi et al. “Quantum Coherent Atomic Tunneling between Two Trapped Bose-Einstein Condensates”. In: *Phys. Rev. Lett.* 79 (25 Dec. 1997), pp. 4950–4953. DOI: `10.1103/PhysRevLett.79.4950`. URL: `https://link.aps.org/doi/10.1103/PhysRevLett.79.4950`.

[19] W. J. Kwon et al. “Strongly correlated superfluid order parameters from dc Josephson supercurrents”. In: *Science* 369.6499 (July 2020), pp. 84–88. ISSN: 1095-9203.

[20] S Levy et al. “The A.C. and D.C. Josephson effect in a Bose Einstein condensate”. In: *Nature* 449 (Nov. 2007), pp. 579–83. DOI: `10.1038/nature06186`.

[21] R Gati and M K Oberthaler. “A bosonic Josephson junction”. In: *Journal of Physics B: Atomic, Molecular and Optical Physics* 40.10 (May 2007), R61. DOI: `10.1088/0953-4075/40/10/R01`.

[22] Francesco Cataliotti et al. “Josephson Junction Arrays with Bose-Einstein Condensates”. In: *Science (New York, N.Y.)* 293 (Sept. 2001), pp. 843–6. DOI: `10.1126/science.1062612`.

[23] Michael Albiez et al. “Direct Observation of Tunneling and Nonlinear Self-Trapping in a Single Bosonic Josephson Junction”. In: *Physical Review Letters* 95.1 (June 2005). ISSN: 1079-7114. DOI: `10.1103/physrevlett.95.010402`.

[24] Niclas Luick et al. “An ideal Josephson junction in an ultracold two-dimensional Fermi gas”. In: *Science* 369.6499 (July 2020), pp. 89–91. ISSN: 1095-9203. DOI: `10.1126/science.aaz2342`.

[25] S. Raghavan et al. “Coherent oscillations between two weakly coupled Bose-Einstein condensates: Josephson effects, π oscillations, and macroscopic quantum self-trapping”. In: *Phys. Rev. A* 59 (1 Jan. 1999), pp. 620–633.

[26] Michael Albiez et al. “Direct Observation of Tunneling and Nonlinear Self-Trapping in a Single Bosonic Josephson Junction”. In: *Phys. Rev. Lett.* 95 (1 June 2005), p. 010402. DOI: `10.1103/PhysRevLett.95.010402`.

[27] J. Sólyom. *Fundamentals of the Physics of Solids: Volume II: Electronic Properties.* Springer, 2008.

[28] Sidney Shapiro. “Josephson Currents in Superconducting Tunneling: The Effect of Microwaves and Other Observations”. In: *Phys. Rev. Lett.* 11 (2 July 1963), pp. 80–82.

[29] B F Field, T F Finnegan, and J Toots. “Volt Maintenance at NBS via 2e/h: A New Definition of the NBS Volt”. In: *Metrologia* 9.4 (Oct. 1973), p. 155.

[30] Jaw-Shen Tsai, A. K. Jain, and J. E. Lukens. “High-Precision Test of the Universality of the Josephson Voltage-Frequency Relation”. In: *Phys. Rev. Lett.* 51 (4 July 1983), pp. 316–319.

[31] Vijay Pal Singh et al. *Shapiro steps in driven atomic Josephson junctions.* 2024.

[32] Sandro Stringari and Lev P.Pitaevskij. *Bose-Einstein condensation and superfluidity.* Oxford science publications, 2016.

[33] Neil W.Ashcroft and N.David Mermin. *Solid State Physics.* Cengage. 1975.

[34] Marcin Budka et al. “Molecular Model of Dynamic Social Network Based on E-mail communication”. In: *Social Network Analysis and Mining* 3 (Sept. 2013).

[35] Claude Cohen-Tannoudji and David Guéry-Odelin. *Advances in Atomic Physics: An Overview.* World scientific, Nov. 2011, pp. 1–767. ISBN: 978-981-277-496-5.

[36] L. P. Pitaevskii S. Giorgini and S. Stringari. “Theory of ultracold atomic Fermi gases”. In: *Reviews of Modern Physics, vol. 80, no. 4, pp. 1215–1274* (2008).

[37] Henning Heiselberg. “Fermi systems with long scattering lengths”. In: *Phys. Rev. A* 63 (4 Mar. 2001), p. 043606. DOI: `10.1103/PhysRevA.63.043606`.

[38] T.-L. Ho. “Universal thermodynamics of degenerate quantum gases in the unitarity limit”. In: *Physical Review Letters, vol. 92, no. 9, p. 090402* (2004).

[39] M. J. H. Ku et al. “Revealing the superfluid lambda transition in the universal thermodynamics of a Unitary Fermi Gas”. In: *vol. 335, no. February, pp. 563–568* (2012).

[40] Giulia Del Pace. “Tunneling transport in strongly-interacting atomic Fermi gases”. PhD thesis. Università degli studi di Firenze, 2020.

[41] Hauke Biss et al. “Excitation Spectrum and Superfluid Gap of an Ultracold Fermi Gas”. In: *Phys. Rev. Lett.* 128 (10 Mar. 2022), p. 100401.

[42] M. Veldhorst et al. “Experimental realization of superconducting quantum interference devices with topological insulator junctions”. In: *Applied Physics Letters* 100.7 (Feb. 2012). ISSN: 1077-3118. DOI: `10.1063/1.3686150`.

[43] Maria Castellano et al. “Realization and Characterization of a Squid Flux Qubit with a Direct Readout Scheme”. In: Jan. 2006. ISBN: 0387263322, 9780387263328. DOI: `10.1007/0-387-31143-2_15`.

[44] B. Ruck et al. “Experimental realization of a 3D integrated RSFQ T-flip-flop using stacktrons”. In: *IEEE Transactions on Applied Superconductivity* 9.2 (1999), pp. 3966–3969.

[45] Peder Heiselberg. “Shapiro steps in Josephson Junctions”. MA thesis. University of Copenhagen, 2013.

[46] K. K. Likharev. “Superconducting weak links”. In: *Rev. Mod. Phys.* 51 (1 Jan. 1979), pp. 101–159.

[47] Vinay Ambegaokar and Alexis Baratoff. “Tunneling Between Superconductors”. In: *Phys. Rev. Lett.* 10 (11 June 1963), pp. 486–489.

[48] G. Del Pace et al. “Tunneling Transport of Unitary Fermions across the Superfluid Transition”. In: *Physical Review Letters* 126.5 (Feb. 2021). ISSN: 1079-7114. DOI: `10.1103/physrevlett.126.055301`.

[49] Jia Du et al. “High-T(c) Superconducting Step-Edge Josephson Junction Detector for Terahertz Imaging”. In: *2009 International Conference on Applied Superconductivity and Electromagnetic Devices, ASEMD 2009* (Sept. 2009).

[50] Giacomo Valtolina. “Superfluid and spin dynamics of strongly interacting atomic Fermi gases”. PhD thesis. Scuola Normale Superiore di Pisa, 2016.

[51] A. Burchianti et al. “Efficient all-optical production of large ^{6}Li quantum gases using D_1 gray-molasses cooling”. In: *Physical Review A* 90 (June 2014). DOI: `10.1103/PhysRevA.90.043408`.

[52] Marcius Extavour. “Design and construction of magnetic elements for trapping and transport of cold neutral atoms”. In: (Jan. 2004).

[53] Michael E. Gehm. *Properties of ^6Li*. 2003.

[54] G. Zürn et al. “Precise characterization of ^6Li Feshbach resonances using trap-sideband-resolved RF spectroscopy of weakly bound molecules”. In: *Physical Review Letters, vol. 110, no. 13, p. 135301* (2013).

[55] F. S. Cataliotti et al. “Josephson Junction Arrays with Bose-Einstein Condensates”. In: *Science* 293.5531 (Aug. 2001), pp. 843–846. ISSN: 1095-9203.

[56] John Clarke and Alex I. Braginski. “The SQUID handbook”. In: 2006.

[57] Carlo Ottaviani et al. “Adiabatic Splitting, Transport, and Self-Trapping of a Bose-Einstein Condensate in a Double-Well Potential”. In: *Physical Review. A* 81 (Apr. 2010).

[58] E. Infeld et al. “Statics and dynamics of Bose-Einstein condensates in double square well potentials”. In: *Physical Review E* 74.2 (Aug. 2006). ISSN: 1550-2376.

[59] A. Griffin, Wen-Chin Wu, and S. Stringari. “Hydrodynamic Modes in a Trapped Bose Gas above the Bose-Einstein Transition”. In: *Phys. Rev. Lett.* 78 (10 Mar. 1997), pp. 1838–1841.

[60] Michail Zak and Igor Kulikov. “Supersonic effects and shock waves in a Bose–Einstein condensate”. In: *Physics Letters A* 307.2 (2003), pp. 99–106. ISSN: 0375-9601.

[61] Stefano Giovanazzi, A Smerzi, and Salvatore Fantoni. “Josephson Effects in Dilute Bose-Einstein Condensates”. In: *Physical review letters* 84 (June 2000), pp. 4521–4. DOI: `10.1103/PhysRevLett.84.4521`.

[62] F. Binanti, K. Furutani, and L. Salasnich. “Dissipation and fluctuations in elongated bosonic Josephson junctions”. In: *Physical Review A* 103.6 (June 2021). ISSN: 2469-9934.

[63] G.释 Paternò A. Barone. “Physics and Applications of the Josephson Effect”. In: John Wiley Sons Ltd, 1982.

[64] R. W. Simmonds et al. “Observation of the Superfluid Shapiro Effect in a ^3He Weak Link”. In: *Phys. Rev. Lett.* 87 (3 June 2001), p. 035301.

[65] Luca Pezzè et al. “Stabilizing persistent currents in an atomtronic Josephson junction necklace”. In: *Nature Communications* 15 (June 2024). DOI: `10.1038/s41467-024-47759-7`.

[66] Steven Strogatz. *Sync: The Emerging Science of Spontaneous Order.* Hyperion Press, 2003. ISBN: 0786868449.

[67] Y. Kuramoto. *Chemical Oscillations, Waves, and Turbulence.* Vol. 66. 7. Springer-Verlag, 1986, pp. 296–296.

[68] B. R. Trees, V. Saranathan, and D. Stroud. “Synchronization in disordered Josephson junction arrays: Small-world connections and the Kuramoto model”. In: *Phys. Rev. E* 71 (1 Jan. 2005), p. 016215.

[69] Haiko Lietz. “Watts, Duncan J./Strogatz, Steven H. (1998). Collective Dynamics of » Small- World « Networks. Nature 393, S. 440 – 442.” In: ed. by Boris Holzer and Christian Stegbauer. Wiesbaden: Springer Fachmedien Wiesbaden, 2019, pp. 551–553.

[70] Francesco Pampaloni and Jörg Enderlein. “Gaussian, Hermite-Gaussian, and Laguerre-Gaussian beams: A primer”. In: (Nov. 2004).

[71] Haishan Cao. “Refrigeration Below 1 Kelvin”. In: *Journal of Low Temperature Physics* 204 (Sept. 2021). DOI: `10.1007/s10909-021-02606-7`.

[72] Steven H. Duncan J./Strogatz. “Collective Dynamics of » Small- World « Networks. Nature 393, S. 440 – 442.” In: Jan. 1998, pp. 551–553.